

October 2021

PATTERN FORMATION AND PHASE TRANSITION OF CONNECTIVITY IN TWO DIMENSIONS

Arman Mohseni Kabir
University of Massachusetts Amherst

Follow this and additional works at: https://scholarworks.umass.edu/dissertations_2



Part of the [Artificial Intelligence and Robotics Commons](#), [Condensed Matter Physics Commons](#), and the [Statistical, Nonlinear, and Soft Matter Physics Commons](#)

Recommended Citation

Mohseni Kabir, Arman, "PATTERN FORMATION AND PHASE TRANSITION OF CONNECTIVITY IN TWO DIMENSIONS" (2021). *Doctoral Dissertations*. 2259.
<https://doi.org/10.7275/24491453> https://scholarworks.umass.edu/dissertations_2/2259

This Open Access Dissertation is brought to you for free and open access by the Dissertations and Theses at ScholarWorks@UMass Amherst. It has been accepted for inclusion in Doctoral Dissertations by an authorized administrator of ScholarWorks@UMass Amherst. For more information, please contact scholarworks@library.umass.edu.

PATTERN FORMATION AND PHASE TRANSITION OF CONNECTIVITY IN TWO DIMENSIONS

A Dissertation Presented

by

ARMAN MOHSENI KABIR

Submitted to the Graduate School of the
University of Massachusetts Amherst in partial fulfillment
of the requirements for the degree of

DOCTOR OF PHILOSOPHY

September 2021

Physics

© Copyright by Arman Mohseni Kabir 2021

All Rights Reserved

PATTERN FORMATION AND PHASE TRANSITION OF CONNECTIVITY IN TWO DIMENSIONS

A Dissertation Presented

by

ARMAN MOHSENI KABIR

Approved as to style and content by:

Donald Towsley, Chair

Jonathan Machta, Member

Narayanan Menon, Member

Weibo Gong, Member

Saikat Guha, Member

Narayanan Menon, Department Chair
Physics

As a small particle moving through the non-linear and disordered medium of life, the dynamics of every single time-step of my being has been unequivocally influenced by the energy fields of many extraordinary individuals. I would like to dedicate this dissertation to the people who truly made it possible:

My beloved parents, especially my mom, Mahin, who has guided my soul, taught me patience and love and inspired me during hard times.

My beloved wife and my best friend, Nazanin, who has been the best companion I could have ever asked for in my life.

My beloved sister, who always believes in me and motivates me to become my best self.

And my teacher, Ostad, who has shown me the way.

ACKNOWLEDGMENTS

First and foremost, I would like to express my sincere appreciation and gratitude to my advisor Professor Don Towsley who has supported me with his technical advice, encouragement, and guidance during my graduate studies. I am particularly thankful for his outstanding effort to widen my academic perspective into many diverse problems. I would also like to especially thank Professor Saikat Guha, who helped me form many of the scientific ideas presented in this dissertation and was always willing to discuss and help in solving the problems along the way.

I would like to extend my special thanks to my dissertation committee members Professor Jon Machta, Professor Weibo Gong, and Professor Narayanan Menon, for their insightful questions, comments, and feedback.

Thanks to all of my former and current colleagues at UMass Amherst, Stefan Dernbach, Gayane Vardoyan, Leila Rashidi, Siddharth pal, Amir Reza Ramtin, for their friendship, technical discussions, and their help during my PhD. I am especially grateful to Stefan Dernbach since we had fruit-full collaborations on quantum-walk-inspired graph neural networks.

I want to extend my deepest gratitude to my parents, my wife, my sister, and my friends who have always supported me with their unconditional love and encouragement to pursue my dreams and become better every day. Without their support, this journey would not have been possible.

ABSTRACT

PATTERN FORMATION AND PHASE TRANSITION OF CONNECTIVITY IN TWO DIMENSIONS

SEPTEMBER 2021

ARMAN MOHSENI KABIR

B.Sc., IKIU, IRAN

M.Sc., SHARIF UNIVERSITY OF TECHNOLOGY, IRAN

Ph.D., UNIVERSITY OF MASSACHUSETTS AMHERST

Directed by: Professor Donald Towsley

This dissertation is devoted to the study and analysis of different types of emergent behavior in physical systems. Emergence is a phenomenon that has fascinated researchers from various fields of science and engineering. From the emergence of global pandemics to the formation of reaction-diffusion patterns, the main feature that connects all these diverse systems is the appearance of a complex global structure as a result of collective interactions of simple underlying components. This dissertation will focus on two types of emergence in physical systems: emergence of long-range connectivity in networks and emergence and analysis of complex patterns.

The most prominent theory which deals with the emergence of long-range connectivity is the percolation theory. This dissertation employs many concepts from the percolation theory to study connectivity transitions in various systems. Ordinary percolation theory is founded upon two main assumptions, namely locality and

independence of the underlying components. In Chapters 2 and 3, we relax these assumptions in different manners and show that relaxing these assumptions leads to irregular behaviors such as appearance of different universality classes and, in some instances, violation of universality. Chapter 2 deals with relaxing the assumption of locality of interactions. In this Chapter, we define a hierarchy of various measures of robust connectivity. We study the phase transition of these robustness metrics as a function of site/bond occupation/removal probability on the square lattice. Furthermore, we perform extensive numerical analysis and extract these robustness metrics' critical thresholds and critical behaviors. We show that some of these robustness metrics do not fall under the regular percolation universality class. The extensive numerical results in this work can serve as a foundation for any researcher who aims to design/study various degrees of connectivity in networks.

In Chapter 3, we study the non-equilibrium phase transition of long-range connectivity in a multi-particle interacting system on the square lattice. The interactions between different particles translate to relaxing the assumption of independence in the percolation theory. Using extensive numerical simulations, we show that the phase transition observed in this system violates the regular concept of universality. However, it conforms well with the concept of weak-universality recently introduced in the literature. We observe that by varying inter-particle interaction strength in our model, one can control the critical behavior of this phase transition. These observations could be pivotal in studying phase transitions and universality classes.

Chapter 4 focuses on the analysis of reaction-diffusion patterns. We utilize a multitude of machine learning algorithms to analyze reaction-diffusion patterns. In particular, we address two main problems using these techniques, namely, pattern regression and pattern classification. Given an observed instance of a pattern with a known generative function, in the pattern regression task, we aim to predict the specific set of reaction-diffusion parameters (i.e. diffusion constant) which can reproduce

the observed pattern. We employ supervised learning techniques to successfully solve this problem and show the performance of our model in some real-world instances. We also address the task of pattern classification. In this task, we are interested in grouping different instances of similar patterns together. This task is usually performed visually by the researcher studying certain natural phenomena. However, this method is tedious and can be inconsistent among different researchers. We utilize supervised and unsupervised machine learning algorithms to classify patterns of the Gray-Scott model. We show that our methods show outstanding performance both in supervised and unsupervised settings. The methods introduced in this Chapter could bridge the gaps between researchers studying patterns in different fields of science and engineering.

TABLE OF CONTENTS

	Page
ACKNOWLEDGMENTS	v
ABSTRACT	vi
LIST OF TABLES	xii
LIST OF FIGURES	xiii
 CHAPTER	
1. INTRODUCTION	1
1.1 Complex Networks	4
1.2 Percolation	5
1.3 Phase Transitions and Universality	8
1.4 One Dimensional Percolation	11
1.5 New Types of Percolation	13
1.6 Reaction Diffusion Patterns	16
1.7 Predicting Reaction-Diffusion Parameters from Observed Patterns	17
1.8 Quantitative Definitions for Reaction Diffusion Patterns	18
1.9 Machine Learning and Analysis of Patterns	21
1.10 Dissertation Outline	22
 2. PERCOLATION THRESHOLD FOR ROBUST NETWORK CONNECTIVITY	 24
2.1 Introduction	24
2.2 Robustness measures	26
2.3 Robust percolation thresholds	28
2.3.1 k-connectivity	28
2.3.2 k-strong-connectivity and k-core	31
2.3.3 k-stub	34
2.4 Finite Size Scaling	35

2.5	Numerical Results	37
2.6	Conclusion and Future Work	39
3.	PHASE TRANSITION, PATTERN FORMATION AND VIOLATION OF UNIVERSALITY IN A NONEQUILIBRIUM PERCOLATION MODEL	41
3.1	Introduction	42
3.2	Related Work	44
3.2.1	Non-equilibrium Phase Transitions	44
3.2.1.1	Percolation Transitions in Reaction-Diffusion Systems	45
3.2.2	Continuous Varying Exponents and Violation of Universality	48
3.2.3	Pattern Formation	50
3.3	The model	51
3.3.1	Time-evolution of Connected Components	55
3.3.2	Phase Transition of Global Connectivity and Finite Size Scaling in time Domain	58
3.4	Mapping to p space	62
3.5	Critical exponents and violation of universality	65
3.5.1	Weak Universality	69
3.5.1.1	Continuous variation of exponents as a function of α	69
3.5.1.2	Effect of Initial Conditions on the Critical Exponents	74
3.6	Phase transition in similar systems	77
3.6.1	Global Connectivity of Photoactive Robotic Swarms	77
3.7	Conclusion and Future Work	81
4.	MACHINE LEARNING PATTERNS OF NATURE	82
4.1	Introduction	82
4.2	Gray-Scott Model	84
4.3	Supervised Learning Methods	86
4.4	Unsupervised Learning Methods	88

4.4.1	Dimensionality Reduction	89
4.4.2	Clustering	92
4.5	Results and Analysis	93
4.5.1	Supervised Classification of Patterns Generated by Gray-Scott Model	93
4.5.2	Supervised Regression of Patterns of Gray-Scott Model	95
4.5.3	Unsupervised Learning Patterns of Gray-Scott Model	98
4.5.3.1	Evaluation Metrics	104
4.5.3.2	Clustering Results	106
4.6	Conclusion and Future Work	109
5.	CONCLUSION AND FUTURE WORK	111
5.1	Robust Network Connectivity	111
5.1.1	Exploring Naturally Formed Networks	111
5.1.2	Robust Connectivity in Real-World Networks and Random Graphs	112
5.1.3	Robustness in Heterogeneous Networks	113
5.2	Connectivity Transitions in Non-equilibrium Systems	114
5.2.1	Cluster Analysis of Multi-Particle Model	114
5.2.2	Connectivity Transitions in Other Reaction-Diffusion Systems	116
5.3	Machine Learning Analysis of Patterns	116
5.3.1	Classifying Patterns From Diverse Generating Functions	117
5.3.2	Embedding Pattern Dynamics	118
	BIBLIOGRAPHY	121

LIST OF TABLES

Table	Page
1.1 Percolation thresholds for various types of lattices.	8
2.1 Bond percolation thresholds.	39
2.2 Site percolation thresholds	39
3.1 Critical exponents as a function of α	71
3.2 Critical exponents as a function of α for random initial condition	77
4.1 <i>ARI</i> value of different combinations of dimensionality reduction and clustering techniques. To calculate <i>ARI</i> , each clustering is compared to the ground. The Combined model which achieves an outstanding performance is created by combining the results of all three models.	108

LIST OF FIGURES

Figure	Page
1.1 An example of a graph with nodes representing components and edges representing interactions between them in the corresponding complex system. This network has $N = 8$ nodes and $L = 10$ edges.	3
1.2 Site percolation on square lattice for different values of site occupation probability p . Blue shows an underlying lattice structure. Red denotes the sites and bonds that belong to the largest connected cluster (LCC), and black shows the sites and bonds that belong to clusters other than the LCC. At $p_c = 0.5928$, we see the emergence of the incipient largest connected component.	7
1.3 Some examples of reaction-diffusion patterns.	16
1.4 Different patterns generate from the same underlying function, with different parameters.	17
1.5 Three images (taken from [1]) of patterns which have similar length-scales and Fourier transform but appear different to human visual system.	19
1.6 area fraction v , Euler characteristic χ , and length of the boundary line s as a function of ρ for some typical patterns, taken from [1]	20
2.1 Models of robustness in connectivity. The arrows depict going from stronger to progressively weaker measures of robustness. In other words, if a network is in the supercritical regime with respect to the stronger of two robustness models, it will be so for the weaker one, but not necessarily vice versa.	27
2.2 The renormalized grid made by joining the disjoint crossings	30
2.3 (a) k -connectivity for bond percolation on square lattice. The critical threshold is $p_c = 0.5$. (b) k -connectivity for site percolation on square lattice. The critical threshold is $q_c = 0.5927$	31

2.4	Counter-example showing possibility of non-equivalence of 3-core and 3-strong component on square lattice with periodic boundary conditions.	33
2.5	(a) k -stub of square lattice for bond percolation. The critical threshold for 4-stub is smaller than 1; (b) k -core of square lattice. Note that the curve for 2-core, 2-connectivity and 2-strong-connectivity are exactly overlapping.	34
2.6	Exponents $\frac{\beta}{\nu}$ and $\frac{\gamma}{\nu}$ for regular percolation, 2-connectivity, and 3-connectivity (a),(b) $p_c = 0.5927$ and (c),(d) $q_c = 0.5$. The linear nature of these scaling exponents verifies the fact that we are at the percolation threshold.	37
3.1	(a) Initial random configuration of particles on the lattice. (b) Configuration after running the dynamics and reaching the termination criteria. The single large cluster has spanning connectivity through the lattice. Images taken from [2]	46
3.2	First two images show the clusters formed in the lattice at two different filling factors (points in time) and at a fixed temperature. The last image shows the behavior of the phase transition of connectivity at different temperatures and different filling factors. Images taken from [3]	47
3.3	Evolution of the fluence profile of a high power laser beam propagating in air [4]. The laser beam forms a large cluster of connected sites at the beginning (dark red cluster in (f)). As it propagates, it forms filamentation patterns and the connectivity of the beam is lost (scattered connected clusters in (j)).	48
3.4	Time evolution of particles on a square lattice of size 128. At $t = 0$, all lattice sites are occupied by a single particle. Colors denote number of walkers on each lattice site.	53
3.5	Time evolution of lattice occupancy. Each site is declared active (black) if there is one or more particles on it. Otherwise, it is declared inactive (white).	54
3.6	Evolution of connected component size. Colors denote component size divided by the size of the lattice.	55
3.7	Scaled size of GCC as a function time for interacting and non-interacting particles. The plots are averaged over 2000 simulations for a lattice with $L = 128$	57

3.8	Percolation probability as a function time for interacting and non-interacting particles. The plots are averaged over 2000 simulations for a lattice with $L = 128$. The system is considered percolated if there exists a spanning cluster which connects two side of the lattice both horizontally and vertically.	58
3.9	Filling factor p as a function of time. Filling factor is a monotonically decreasing function of time.	59
3.10	Scaled GCC size (a), percolation probability (b), truncated average cluster size (c), and largest non-percolating cluster (d) as a function of time for different lattice sizes. The phase transition in connectivity becomes sharper as the size of lattice increases.	60
3.11	Scaled GCC size (a) and percolation probability (b) as a function of time for system sizes and different α s. Here, as in all of the figures, we show curves for $L = 50$, $L = 60$, $L = 70$, $L = 80$, $L = 90$, and $L = 100$. Colors denote different α values. As we increase α , the transition happens later in time. Also, the near-critical behavior of Π and P_∞ changes as we change the interaction strength by changing α	61
3.12	Finite size scaling for Π as a function $t - t_c$. $\nu = 1.6 \pm 0.26$ gives us the best curve collapse for different length scales.	63
3.13	P_∞ and Π as function of filling factor.	65
3.14	(a) and (b) show long-time behavior of S and s_{max} . (c) shows the long-time behavior of connected components. In early stages ($t = 15$ and $t = 25$), there are many small connected components. As time elapses, these small components (mainly free particles) coagulate and form components with higher density. These aggregated particles form the pattern of spots observable at $t = 400$	66
3.15	(a) Percolation probability Π with respect to the filling factor p . The expected unique crossing point defines $p_c = 0.616 \pm 0.001$. All the curves result from the average of 5×10^6 independent runs. (b) Percolation probability Π as a function of the re-scaled variable $(p_c - p)L^{\frac{1}{\nu}}$, yielding $\nu = 1.30$ by curve collapse.	68
3.16	(a) Percolation strength Π_∞ dependence on the filling factor p . (b) Rescaled cluster strength P_∞ as a function of the rescaled parameter $(p_c - p)L^{\frac{1}{\nu}}$. The ratio $\beta/\nu = 0.11 \pm 0.01$ yields the same value of p_c found using Π	69

3.17	Rescaled largest non-percolating cluster as a function of rescaled parameter $(p_c - p)L^{\frac{1}{\nu}}$. Seeking a curve collapse leads to the determination of $\sigma = ? \pm$	70
3.18	(a) Average cluster size S with respect to p . The percolating cluster has been excluded in calculating the average cluster size. (b) $\ln(S)$ with respect to the $\ln L$, allowing us to find $\frac{\gamma}{\nu} = ? \pm 0.05$	71
3.19	Percolation probability Π as a function of filling factor p for $\alpha = 1.1$ and $\alpha = 0.6$ with the same uniform initial conditions.	72
3.20	Cluster size distribution at $p = p_c$ for systems simulated with two different α parameters. along with regular site percolation on square lattice at $p = 0.5927$. System size is $L = 300$	74
3.21	P_∞ and Π as function of filling factor for a system with random initial condition and $\alpha = 0$	76
3.22	Collective aggregation patterns forming in positive delay regime. Image taken from [5]	79
3.23	Percolation probability as a function of time for photoactive swarm of robots defined by Eq. (3.13).	80
4.1	Set of 12 distinct Gray-Scott patterns taken from ref. [6]. Colors represent concentration of chemical U where red represents $U = 1$ and red represents $U = 0.2$. Yellow is intermediate to red and blue.	86
4.2	Schematic overview of a CNN architecture used in this work. An image is passed through the network. Network weights are iteratively updated by back-propagating the error from the output layer.	88
4.3	Convolutional autoencoder is built by stacking a convolutional neural network with a mirror version of itself. The latent variables in the middle layer are forced to capture the most important features of the image to recreate it in the output.	91
4.4	Collection of 7 patterns from Gray-Scott equations chosen for this work.	94
4.5	Classification accuracy as a function of training iterations. The model reaches the maximum accuracy of around 99% in early stages of training.	94

4.6	First row shows images generated from simulating the Gray-Scott equations with random set of F and K parameters. Images in the second row are generated by feeding the first row images to our trained regression model, getting model predictions for F and K , and simulating the Gray-Scott equations with these F and K parameters with random initial conditions.	96
4.7	The left column shows real vegetation patterns taken from [7]. The right column shows the mapping of these patterns to the Gray-Scott patterns based on the predictions of our trained model.	97
4.8	PCA applied to 7 patterns of Fig 4.4. Each color refers to a specific type of pattern generated from a specific set of F and K parameters. The figure is colored based on our previous knowledge for visualization purposes and the algorithm does not have access to these labels.	99
4.9	GMM clustering applied to the results of PCA. Here the colors denote the way GMM has separated different clusters. Compared to k -means, we see more accurate differentiation between clusters.	100
4.10	VAE applied to 7 patterns of Fig 4.4. Each color refers to a specific type of pattern generated from a specific set of F and K parameters. The figure is colored based on our previous knowledge for visualization purposes and the algorithm does not have access to these labels.	100
4.11	GMM clustering applied to the result of VAE. Colors are specified by the algorithm to separate different detected Gaussian distributions.	102
4.12	Minkowski measures as a function of threshold parameter ρ . All of the plots are averaged over a large number of realizations of the pattern shown above.	103
4.13	The two figures shown above represent two different clusterings of a set of data points in a two-dimensional space. In this case, the clusterings of the points are identical but are labeled (colored) differently. Therefore, in this case, $ARI = 1$	106

5.1	Largest connected component (LCC) for different values of α at $t = t_c$. There are significant qualitative differences between the two patterns. One observable difference between the two images is the hole size distribution in the LCC.	115
5.2	Path of a pattern in PCA space. Colors denote time. Dark red denotes $t = 0$ and dark blue denotes $t = 100$. At the top, we see example snapshots of the evolution of the pattern in time. The pattern is called Chaos in Gray-Scott category of patterns.	119

CHAPTER 1

INTRODUCTION

This dissertation is devoted to the study of pattern formation and phase transition of connectivity in two-dimensional systems. One of the most fascinating fields of research in physical systems is the study of *emergent behavior*. Emergent behavior in complex systems is observed in diverse fields ranging from self-organization of viral capsules from small protein components [8] to flocking of birds [9] to epidemic spreading [10] and molecular self-assembly [11]. The main feature that connects all these diverse sets of phenomena is the appearance of complex global structure and dynamics resulting from collective interactions of simple underlying components. In this dissertation, we will focus on two types of emergence in physical systems, namely emergence of long-range connectivity in networks, and emergence and analysis of complex patterns.

When the system under study can be modeled as a network, connectivity becomes one of the system's characteristics, which is of utmost importance. Long-range connectivity is crucial (detrimental) in many engineered and naturally-formed networks. For example, a deadly virus can create a pandemic and quickly reach the other side of the globe as a result of small-scale interactions among people. On the contrary, networks like the Internet require long-range connectivity in order to function properly. One of the most prominent theories that deal with the emergence of global connectivity due to local interactions is percolation theory. This theory has been extensively applied to the study of connectivity in complex networks. However, in its original formulation, percolation theory deals with a simplistic notion of connectivity

that is not adequate in capturing higher levels of complexity or higher degrees of connectivity observed in real-world networks. In addition, percolation theory only deals with static networks in which there is no correlation (interdependence) between the components of the network. Hence, it is necessary to develop more generalized notions of percolation to accommodate higher layers of complexity observed/required in real-world networks. In Chapter two of this dissertation, we introduce new notions of connectivity in networks. We study the emergence of long-range connectivity based on these new notions on a square lattice graph, and we investigate the size and statistics of connected components. In the third chapter of this dissertation, we study the temporal transition of long-range connectivity in a multi-particle system on the square lattice. Here we employ the simple notion of connectivity defined by ordinary percolation but relax one of the main assumptions of percolation theory: the lack of correlation between constituents of the network. We show that the temporal evolution of connected components does not follow the universal behavior observed in most problems studied in percolation theory. In addition to the emergence (loss) of long-range connectivity, we observe the emergence of various types of patterns usually observed in reaction-diffusion systems.

Complex patterns emerge in many real-world phenomena. From ecological systems like brushlands and mussel beds, to filamentation patterns formed when a high power laser beam passes through air. The study and analysis of these patterns have been the focus of many fields of science and engineering. Although numerous studies focused on the mathematical modeling of different pattern formation phenomena, analyzing and quantifying the patterns observed remains scarce. Most of the existing literature on pattern analysis uses a qualitative approach to explain patterns in various systems, and this qualitative analysis is limited by our visual ability to distinguish patterns such as the labyrinth, spots, mazes, filaments, etc.

In the last chapter of this dissertation, we employ methods from machine learning to analyze, classify and predict relevant parameters of two-dimensional patterns generated from any underlying dynamics. In particular, we test these methods on patterns generated from a specific set of equations, called Gray-Scott equations [12]. We utilize supervised learning methods to predict the underlying parameters of a given pattern-generating system of equations given an observed pattern. In addition, we employ unsupervised learning techniques to cluster patterns into different groups by mapping them to a low-dimensional space. This low-dimensional representation can be the first step in creating a more universal quantitative definition for patterns generated in different domains.

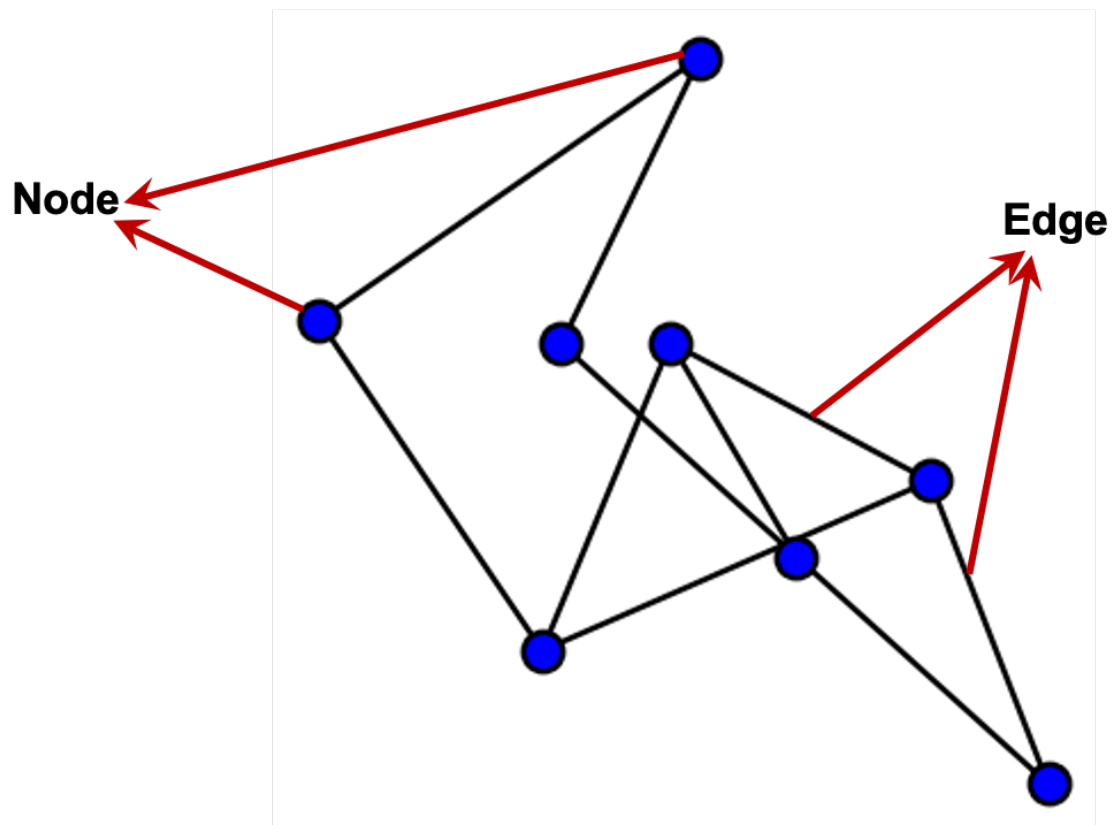


Figure 1.1: An example of a graph with nodes representing components and edges representing interactions between them in the corresponding complex system. This network has $N = 8$ nodes and $L = 10$ edges.

1.1 Complex Networks

Complex networks provide a simple yet valuable mathematical framework to study complex systems. Many real-world phenomena such as emergent collective behavior of animals, disease spreading, the human brain, and the Internet are increasingly being modeled and studied in the form of complex networks. Networks capture the most important characteristic of such systems, namely the agents and the interactions. In the most simplistic approach, the complex system is mapped to a graph (??) where the small constituents are represented as nodes (sites, vertices) and the interactions are represented as edges (bonds, links). For example, a social network is a set of individual accounts (nodes) linked through their friendship connections (edges). Another example is the power grid. Power-plants and electricity-consuming units can be modeled as nodes, and wires connecting these components are modeled as edges. Similar mappings apply to transportation networks, supply chains, ecological interactions, protein interaction networks, and economic networks.

This simple representation of networks as simple graphs can be further enhanced to become more realistic and account for more diverse interactions and interacting components. Nodes may have weights to model different levels of importance or intensity. Similarly, edges can be weighted to show the relative importance of interactions [13]. In many real-world networks like transportation networks, connections have a specific orientation, so edges can be directed to account for these types of interactions. Almost all real-world networks evolve in time. This evolution can be captured by either transformation of the network's backbone, like the addition/removal of nodes or edges, or by dynamics on the network, like epidemics in social networks. The spatial structure of the underlying system can be included in the graph representation [14].

Proper functionality of many real-world networks depends on the connectivity of the underlying graph. To give a few examples, an accident on one road might cause a traffic jam which spans across a city; a breakdown of power-grid and a total blackout

might be caused by damage to a few power stations as what occurred in Italy in 2003 [15]. On the other hand, global connectivity can also be unfavorable in many cases; pandemics spread the fastest when the underlying network is well-connected, as we observed in the COVID-19 pandemic [16]; global connectivity in a forest will have devastating effects in the case of a forest fire [17]. The study of connectivity in complex networks thus is imperative in predicting, controlling, and designing such systems.

In this thesis, we approach the problem of connectivity from the perspective of percolation theory. Percolation theory is a classic research topic in statistical physics that deals with connectivity in graphs subject to removal or insertion nodes or edges. In Chapters 2 and 3 of this dissertation, we focus on new types of percolation transitions in two-dimensional lattices.

1.2 Percolation

The percolation model was suggested by Broadbent and Hammersley in 1957 [18, 19]. Percolation theory studies the statistical properties of connected clusters in different random and disordered systems. Since its introduction, percolation theory has been found effective in modeling many real-world complex systems. Examples of such systems include forest wildfires, polymer gels, porous media, galaxies, and epidemics.

A simple realization of percolation phenomena can be depicted on a square lattice. A square lattice is a graph where each site represents a node in the graph, and each bond represents an edge. Each site on the square lattice has four nearest neighbors. Assume that each site on the lattice can have two states, namely occupied or empty. Each site on the lattice is declared occupied with probability p and empty with probability $1 - p$. Two occupied sites belong to the same cluster if a path of nearest neighbor-occupied sites connects them. This connected system of

occupied-empty sites can model many disordered physical systems like the percolation of through porous media. As the probability of a site being occupied increases, the average size of the connected clusters increase. For an infinite system, there exists a critical probability p_c above which there exists an infinite-sized cluster. Below this critical probability, only finite-size clusters exist. Bond percolation is defined similarly; instead of declaring sites occupied/empty with a certain probability, bonds are occupied in this manner. The value of p_c in which global connectivity occurs depends on the type of percolation (site or bond) as well as dimensionality of the problem. In addition, if we change the lattice structure to another type of lattice-like triangular lattice or a more general graph, p_c changes.

Fig. 1.2 shows site percolation on a square lattice of size 32 by 32 for different values of p . The underlying lattice structure is shown in blue. Red denotes the sites and bonds that belong to the largest connected cluster (LCC), and black shows the sites and bonds that belong to clusters other than the LCC. The site percolation threshold for square lattice is found to be approximately $p_c = 0.5928$. For systems of infinite size, above this threshold, there exists an infinite-sized LCC.

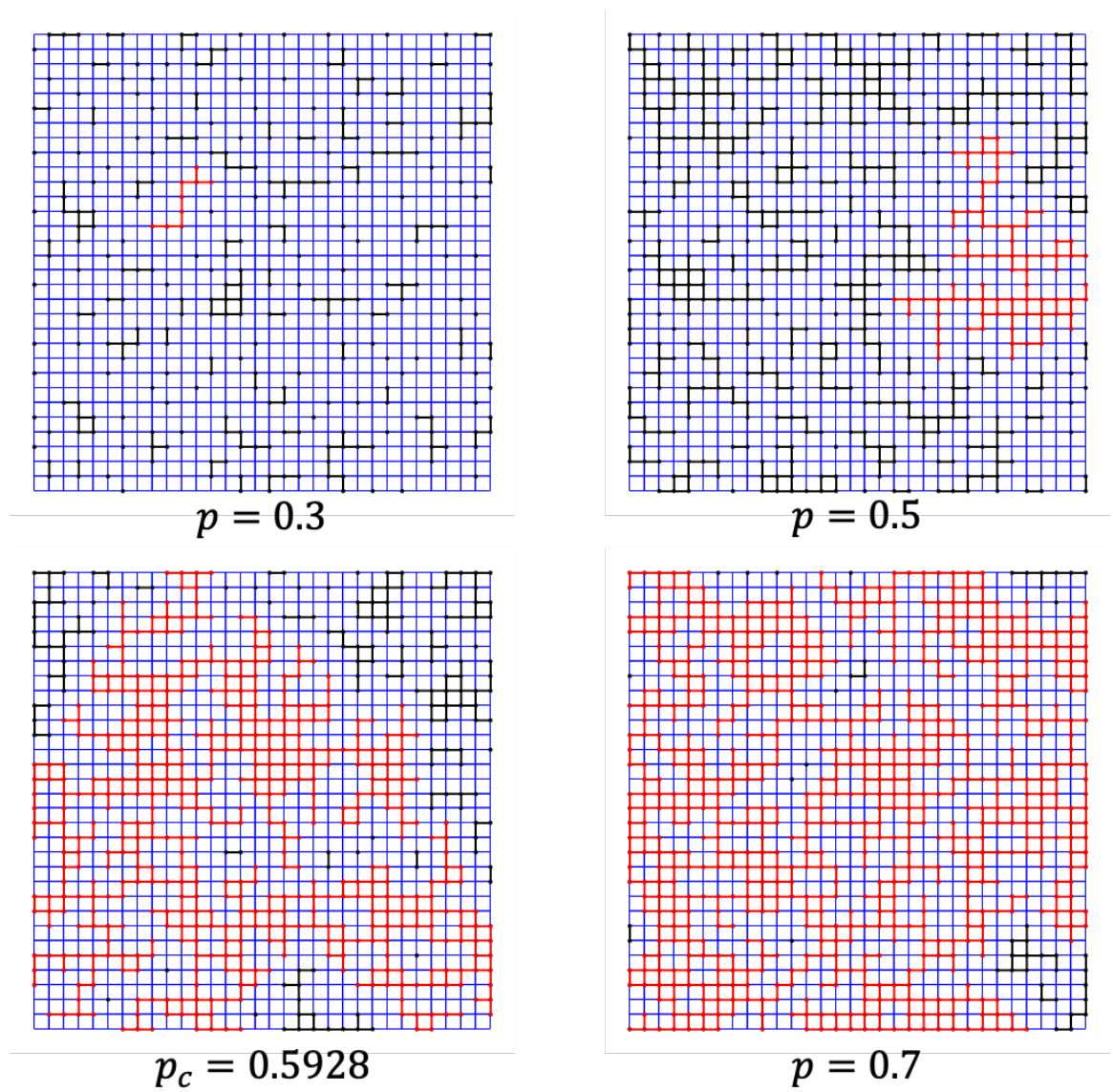


Figure 1.2: Site percolation on square lattice for different values of site occupation probability p . Blue shows an underlying lattice structure. Red denotes the sites and bonds that belong to the largest connected cluster (LCC), and black shows the sites and bonds that belong to clusters other than the LCC. At $p_c = 0.5928$, we see the emergence of the incipient largest connected component.

Table 1.1 shows the percolation threshold for site and bond percolation for various lattices [19].

Lattice	Site Percolation Threshold	Bond Percolation Threshold
Square	0.5927	$1/2^{(exact)}$
Triangular	$1/2^{(exact)}$	$2 \sin(\pi/18)^{(exact)}$
Honeycomb	0.6962	$1 - 2 \sin(\pi/18)^{(exact)}$
Diamond	0.43	0.388
Cubic	0.31161	0.2488
Hypercubic ($d = 4$)	0.197	0.160

Table 1.1: Percolation thresholds for various types of lattices.

Although percolation is a simple problem to formulate, understanding the statistical properties of connected components and determining the exact critical point is a tough problem to solve theoretically. It is evident from Table 1.1 that exact critical points are known only for a small number of special lattices [20, 21]. The results for other lattices are found using various techniques such as Monte Carlo simulations, and series expansion [22, 23]. For example, for $d = 1$, we can easily see that in order to have an infinite cluster that connects two sides of the lattice, all the sites should be occupied, which means $p_c = 1$. Broadbent and Hammersley [18, 19] showed that $0 < p_c < 1$ for $d \geq 2$. In addition, Grimmet showed that the probability of existence of an infinite cluster is 0 for $p < p_c(d)$ and 1 for $p > p_c(d)$ for all d .

A natural extension of percolation on a lattice is continuous percolation. In this model, sites are not bound to be on specific locations as defined by the lattice structure. Examples include porous media in which pores play the role of unoccupied sites. Similarly, many technological problems can be mapped to continuous percolation on a plane or in 2 dimensions. For example, the area covered by a set of Uber drivers in a city or connectivity of wireless antennas spread throughout an area.

1.3 Phase Transitions and Universality

In the physical sciences, phase transitions are usually attributed to phenomena in which there is a transition between different states of media. as exemplified by solid

to liquid transition. During a phase transition, some macroscopic characteristics of matter (i.e., density or magnetization) experience a sharp change due to a change in one of the system's external parameters (i.e., pressure or temperature). As an example, a system of spin $\frac{1}{2}$ particles that possess no macroscopic magnetization at high temperature due to disorder spontaneously transition into an ordered state, which has measurable macroscopic magnetization. The most important property in this transition is the development of long-range order. At high temperatures, the spins are pointing in random directions. As we decrease the temperature, there is a specific temperature at which the spins develop long-range correlations, and the system jumps to an ordered phase in which the majority of spins are in the same direction. In this example, temperature is our *control parameter* and magnetization is what we call an *order parameter*. As evident from its name, the order parameter is one of the system variables that characterize long-range correlations (order). In the case of percolation transitions, the probability that a site belongs to the infinite cluster (LCC in finite systems) is the order parameter. Similar to the phase transition in an Ising system of spins, there is a critical p (site occupation probability) at which the system jumps from no long-range correlations to a system with an infinite-sized cluster that encompasses the lattice. The critical threshold at which the transition occurs is called *critical point* or *critical threshold*. As mentioned earlier in the chapter, p_c is the critical point in a given percolation problem. Similarly, for an Ising system of spins, the critical temperature T_c in which long-range order appears is the critical point.

A class of phase transitions known as *continuous phase transitions* (second-order transitions) exhibit another notable property, namely *universality*. Universality is the observation that many macroscopic properties of a large class of systems are independent of the dynamical details of the system. The concept of universality was first clearly formulated by Kadanoff [24]. The universality hypothesis reduces various

phase transitions observed in various systems to a small number of equivalence classes. These classes are called *universality classes* and depend only on a few fundamental parameters of the system under study.

In continuous transitions, macroscopic observables of the system behave as power laws near the critical point. The exponents for these power laws are known as *critical exponents*. The universality principle claims that in systems with short-range interactions, these exponents are independent of the details of the system and only depend on the dimensionality and symmetries of the system [25]. In short, the critical power-law behavior and scaling functions are the same for all systems that belong to a given universality class. As an illustrative example, the exponent describing the magnetization transition in all three-dimensional magnetic materials is the same, regardless of the crystalline structure and the type of short-range interactions.

Percolation can be viewed as a purely geometrical critical phenomenon. Similar to what is observed in thermodynamic critical phenomena, percolation quantities behave as powers of the control parameter. The exponents that characterize these power law behaviors are called *critical exponents*. For example, in thermodynamic phase transitions, macroscopic thermodynamic quantities scale as powers of $(T - T_c)$ where T is the temperature of the system and T_c is the critical temperature in which the transition happens. For percolation, macroscopic quantities of the system scale as powers of $p - p_c$ near the critical point. One of the quantities of interest in percolation is P_∞ , the probability that a site belongs to the infinite cluster. For an infinite system, $P_\infty = 0$ below p_c . Above p_c , P_∞ behaves as a function of p as follows:

$$P_\infty = (p - p_c)^\beta. \quad (1.1)$$

The average distance between two sites belonging to the same finite cluster (also known as correlation length) is characterized by ξ . When p approaches p_c , ξ diverges as:

$$\xi = (p - p_c)^{-\nu}. \quad (1.2)$$

Similarly, average cluster size S , scales with $p - p_c$ as follows:

$$S = (p - p_c)^{-\gamma} \quad (1.3)$$

Although the value of the percolation threshold strongly depends on the structure and connectivity of the graph, the near-critical behavior of macroscopic parameters like P_∞ , ξ , and S is known to be invariant to microscopic details of the lattice structure (i.e., triangular lattice vs. square lattice), and even type of percolation (site, bond, continuum). For example, two-dimensional percolation problems on lattices and continuum space with short-range interactions (short-range neighborhood and connectivity) all belong to the percolation universality class. This means that a set of fixed critical exponents explain the near-critical behavior of connected components in all different types of lattices and percolation problems.

1.4 One Dimensional Percolation

To illustrate the behavior of different variables in percolation theory, here we consider the simple example of one-dimensional percolation. Let us assume that we have an infinite 1-dimensional chain of connected sites. Similar to the 2-dimensional model introduced earlier, we randomly occupy sites with probability p and form connected components based on nearest neighbor proximity of occupied sites. To have a finite size-cluster, we need to have a chain of connected occupied sites with two empty sites at both ends. Therefore, the number of clusters of size s per lattice site (n_s) is

$$n_s = p^s(1 - p)^2. \quad (1.4)$$

In the above equation, we need to have s occupied sites each with probability p , and two empty sites at two ends of the cluster, each with probability $(1 - p)$. Equation (1.4) could be regarded as the probability of a site belonging to the left-most side of a connected chain. Knowing n_s , the probability of a site belonging to a cluster of size s can be calculated as $n_s s$. It is easy to show the following equality:

$$\sum_s s n_s = p \quad (1.5)$$

As mentioned earlier, we can easily deduce the percolation threshold for a 1-d chain. For any $p < 1$, there exist at least a single unoccupied site in an infinite lattice. Therefore all the sites should be occupied in order to have a connected chain that connects two ends of the lattice. For this reason,

$$p_c = 1. \quad (1.6)$$

As discussed above, one particular variable of interest near the critical point is *average cluster size*, defined as:

$$\sum_s \left(\frac{n_s s}{\sum_s n_s s} \right) s. \quad (1.7)$$

Simplifying the above equation, we get:

$$S(p) = \frac{1 + p}{1 - p}. \quad (1.8)$$

$S(p)$ is equivalent to susceptibility in thermodynamic phase transitions. In continuous phase transitions, it is known that susceptibility diverges at the critical point as we observe it happens for this one-dimensional lattice percolation problem.

1.5 New Types of Percolation

The emergence of global connectivity from random local interactions has been successfully captured by ordinary percolation. This simple notion of percolation has particularly been helpful in fields like materials research. In systems which this assumption holds, the interactions are simply bound to the underlying graph structure, and most of the time, higher orders of interactions can be ignored. However, introducing more layers of complexity is essential to gain a better quantitative explanation of connectivity and robustness in complex systems [26]. Classical percolation theory is based on two fundamental assumptions: interactions are independent and local. Relaxing any of the aforementioned assumptions has been the focus of the study of many recent works on percolation theory. Goltsev et al. [27] and Baxter et al. [28] expanded the condition of simple connectivity and added extra conditions for a structure to be considered connected. As an example, k -core percolation was introduced. Aside from the ordinary condition of connectivity, each node in the graph must have at least k neighbors, which are part of the k -core component. The addition of such a condition drastically alters the near-critical behavior of "connected" clusters. The concepts of dense subgraphs and k -core components were first introduced in the context of social networks [29]. Later it was also used in other fields like modeling protein interaction networks [30]. Of significance to our work are studies that look at more fault-tolerant percolation problems by introducing stricter conditions for connectivity. Newman et al. [31] looked at percolation of sub-graphs that satisfy the condition of bi-connectivity. A bi-connected component is a component in which there are at least two distinct paths between elements in the component. This stricter level of robustness is essential in designing engineered networks that are robust to random failure of specific nodes. It has also been observed that many naturally formed networks such as biological networks [32] employ this notion of multi-path connectivity to avoid catastrophic failures when some components malfunction. Newman et al. [31] showed

that in most networks of interest, the critical point for the appearance of a giant connected component coincides with the emergence of a giant bi-connected component. The co-appearance of a giant connected component and a giant bi-connected component is an exciting finding since it allows researchers to utilize the existing literature on ordinary percolation in designing systems that are also fault-tolerant by standards of bi-connectivity. All of the previously mentioned research works focused on static networks; however, most networks change over time in the real-world. Many recent works focused on percolation problems on temporal networks [33, 34]. Others have focused on percolation on growing networks [35]. In these problems, the number of elements dynamically increases while forming random connections. Introducing non-local interactions in the percolation process has also become a center of focus. In his attempt to delay the emergence of connected clusters and to create a sharper transition, Achlioptas et al. [36] suggested a variant of bond percolation called *explosive percolation* in which adding each new bond is based on global knowledge of the network. For each new bond, two non-occupied bonds are randomly selected, then one of them is selected based on the size of the clusters that the bond is joining. Adding this global information breaks the locality assumption and significantly changes the critical behavior of the transition. These non-local effects often lead to delayed phase transitions, which are sharper in nature.

Another approach in expanding percolation to real-world scenarios is to relax the independence of interactions assumption. In fact, in most real-world applications like social phenomena, cooperative effects between components play a critical role in the emergence of global connectivity in the system. Reaction-diffusion systems are abundant in nature ranging from predator-prey dynamics in an ecological region or chemical reactions among multiple species; all these systems have some degree of correlation between their components. Similarly, in epidemic processes like the spread of a rumor, the number of contacts a given person following a rumor affects the per-

son’s probability of re-sharing the rumor. In disease spreading, each contact with an infected individual may weaken the susceptible person’s immune system and change the infection rate. Although relaxation of the independence assumption in percolation studies is much less prevalent, many researchers studied percolation transitions in such systems [2–4, 37, 38].

As stated earlier, connectivity is a central property of many complex systems. In many systems, global connectivity is needed to ensure proper performance (i.e., communication networks, biological networks). However, in many real-world complex systems, global connectivity is a property to avoided (i.e., epidemic processes, rumor propagation). For this reason, studying new types of percolation in more real-world scenarios is pivotal in modeling, designing, and controlling functional networks.

In the following two chapters of this thesis, we investigate new types of percolation transitions and study how changing the local interactions of percolating agents or changing the underlying definitions for connectivity in a network alters the critical behavior of the system. In the second chapter, we introduce a hierarchy of robustness metrics for connectivity. We then investigate the thresholds, critical behavior, and universality classes of each measure of connectivity on the square lattice. We show that although the critical threshold remains unchanged for stricter robustness measures such as bi-connectivity, the critical exponents and universality classes are different.

In the third chapter, we introduce a multi-particle interacting system and study pattern formation and phase transition of connectivity in such a system as a function time. We show that our multi-particle system undergoes a percolation transition; however, our system breaks the ordinary notion of universality. As mentioned earlier in this chapter, the concept of universality stems from the observation that microscopic details of the graph structure and interactions between components become irrelevant when studying macroscopic quantities near a phase transition. Our model

breaks this paradigm since slight changes in our interaction model change the scaling relations and critical exponents characterizing the phase transition.

1.6 Reaction Diffusion Patterns

The first quantitative formulation of pattern formation was presented in a seminal paper by Turing [39] approximately 70 years ago. His findings were experimentally verified four decades later by a remarkable experiment designed by Castets et al. [40]. Utilizing the reaction-diffusion principles formulated by Turing, computer scientists started to investigate pattern formation in computer graphics. Turk [41], Witkin et al. [42] used reaction-diffusion equations to generate a variety of patterns observed in nature including animal skin patterns. Fig. 1.5 shows an example set of patterns observed in reaction-diffusion systems.

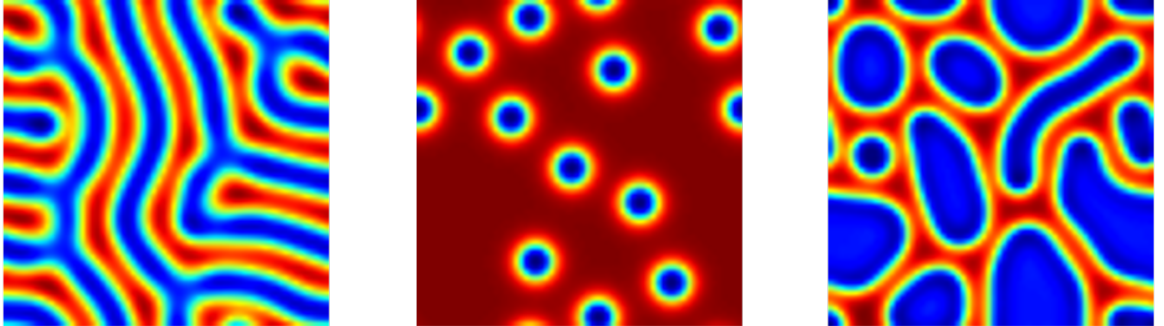


Figure 1.3: Some examples of reaction-diffusion patterns.

The system Turing studied took the following form:

$$\frac{\partial \mathbf{u}}{\partial t} = \mathbf{D} \nabla^2 \mathbf{u} + \mathbf{f}(\mathbf{u}), \quad (1.9)$$

where \mathbf{D} is the matrix of constant diffusion coefficients, \mathbf{u} is a vector of chemical concentrations and $\mathbf{f}(\mathbf{u})$ is a non-linear function. Here \mathbf{u} is an n dimensional vector characterizing different chemical reactants. In this case \mathbf{D} will be an n -dimensional

matrix of constant coefficients that characterize the rates of diffusion for each chemical.

1.7 Predicting Reaction-Diffusion Parameters from Observed Patterns

Assume that, based on extensive experimentation and observations, we know that a particular natural pattern (i.e., leopard skin patterns) is generated from a Turing reaction-diffusion system as explained above with a known functional form of $\mathbf{f}(\mathbf{u})$. Different values of \mathbf{D} in this equation will give rise to patterns with different characteristics. Fig. 1.4 shows an example of such patterns generated from the same underlying function with different values of coefficients.

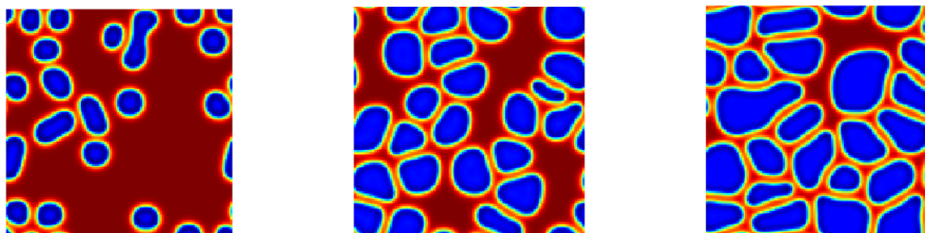


Figure 1.4: Different patterns generate from the same underlying function, with different parameters.

Now, consider the following inverse problem. Given a specific sample (image of a pattern observed in an experimental setting) of the pattern space from this reaction-diffusion equation, find the underlying parameters that created this specific realization. This is an extremely hard problem to address in an ongoing chemical reaction or a living leopard in an experimental manner. Another approach would be to run numerous simulations and do a hyper-parameter search in the space of all patterns that can be generated by this set of equations. Both of the above approaches

are extremely costly and do not create repeatable solutions. Some works focused on extracting geometric features [43] and using these features to predict the underlying parameters; however, these approaches need to be specifically designed for various types of patterns and underlying dynamics. This dissertation (Chapter 4) will utilize supervised learning methods to address this inverse problem as a more robust and repeatable solution.

1.8 Quantitative Definitions for Reaction Diffusion Patterns

Despite remarkable progress in understanding various mechanisms leading to the formation of patterns in diverse systems, some key elements are still surprisingly missing in the scientific literature. For example, what do physicists, biologists, or ecologists precisely mean by reaction-diffusion patterns, how do they identify and classify them, or characterize their properties? In the reaction-diffusion literature, one comes across visual characterization of various patterns as "spots", "mazes", or "stripes". However, these terms are extremely general characterizations of patterns and are limited by our visual ability to distinguish certain patterns. More importantly, "spot" patterns observed in a specific biological phenomenon may have very different geometrical characteristics than "spots" observed in the formation of stars in a galaxy. If we aim to have a more universal understanding of pattern formation and analysis, there is an urgent need to have a more robust quantification of patterns so that researchers from different fields can map their findings into a more coherent framework. One of the most common ways of approaching this problem could be to study Fourier transformation or auto-correlation functions [44] of the pattern images. While these methods can provide insightful information about the orientational order or characteristic length scales of the patterns, they fail to capture more subtle nuances and differences in complex patterns [1]. Therefore, if two patterns have the same average periodicity and length scales but visually differ significantly, these methods will

still classify them in a single class. As an example, Fig. 1.5 shows three very different patterns to the human eye, but their general length-scale and periodic structure are similar and indistinguishable using simple auto-correlation and Fourier analysis. The main differences between these images are more subtle changes in the connectivity of the structures, curvatures of the stripes, and more nuanced features.

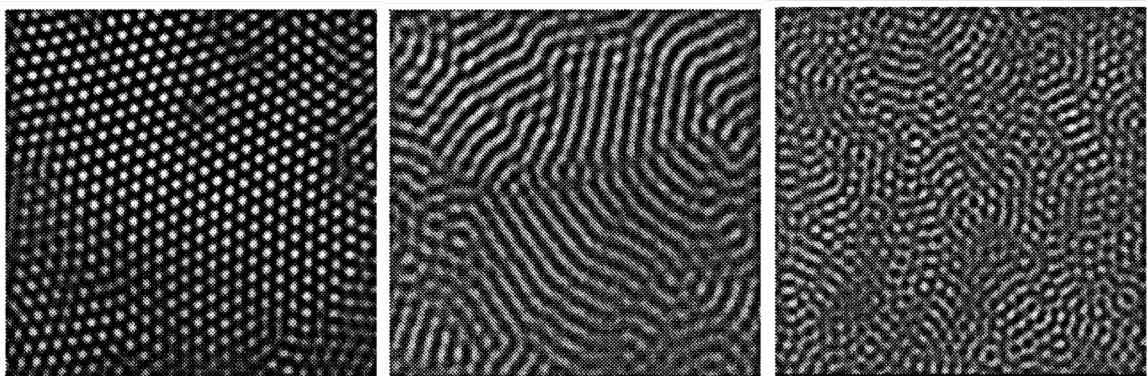


Figure 1.5: Three images (taken from [1]) of patterns which have similar length-scales and Fourier transform but appear different to human visual system.

Mecke [1] introduced more detailed morphological and geometrical characteristics of patterns that are very useful in distinguishing patterns. In this case, a pattern is considered to be a two-dimensional image. In order to find the geometrical properties of this image, he chooses a threshold ρ to turn this grey-scale image into a black and white image. After transforming the pattern into a two-dimensional black and white image, the following characteristics, called Minkowski measures, are calculated for the image.

- The area fraction $v(\rho)$ defined as the fraction of black pixels.
- The length of the boundary line $s(\rho)$ between black and white regions measured as the number of pairs of neighbored black and white pixels normalized by the total number of pixels.

- The so-called Euler characteristic $\chi(\rho)$ defined as the difference between the number of white connected components and black connected components normalized by the total number of pixels.

All these quantities are functions of ρ , the threshold to transform a grey-scale image to a black and white image. Therefore, Mecke postulated that plotting simple combinations of these quantities as a function of ρ should give a different plot for different types of patterns with different morphological characteristics. Fig. 1.6 shows an example of plots gained by varying the threshold taken from [1]. Mecke showed

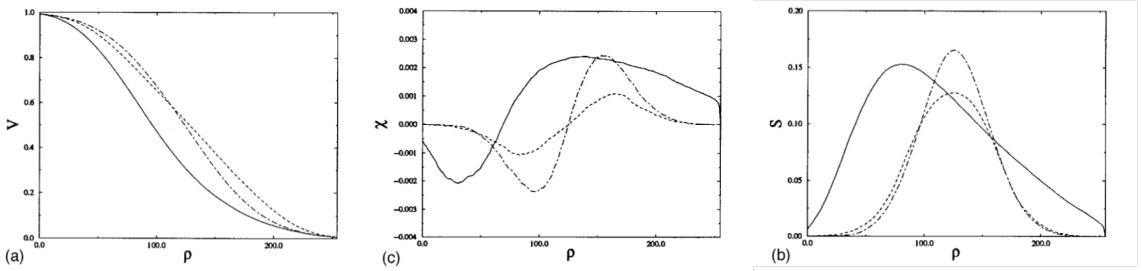


Figure 1.6: area fraction v , Euler characteristic χ , and length of the boundary line s as a function of ρ for some typical patterns, taken from [1]

that if we approximate the aforementioned curves (for more details please see Chapter 4) with polynomials, one can distinguish different patterns by coefficients of the polynomials. While this method has made significant progress in mapping patterns to a lower-dimensional space, it has some shortcomings. First and foremost, it is computationally expensive. For any given pattern, one needs to sweep over a large number of thresholds and find detailed measures of connectivity and boundary length information, which becomes very costly as the size of the image increases or if we need to sweep over a large number of thresholds to get a fine-grained curve. Another shortcoming of this analysis comes from the fact that it cannot deal with black and white patterns since a black and white image will only give a single point in the space of curves discussed above. Many patterns observed in cellular automata literature or

materials science are, in essence black and white patterns. There were other attempts to overcome the latter shortcoming [45, 46]; however, they were designed for specific problems rather than being a holistic approach. This shortcoming limits the ability of this method to categorize these types of patterns into other known patterns. For the above mentioned reasons, there is a need for methods that are more computationally tractable and at the same time are more widely applicable to various types of patterns.

1.9 Machine Learning and Analysis of Patterns

Machine learning has seen dramatic progress in the past decade. This has been mainly driven by advancements in artificial neural networks and an exponential growth in computation power. Commonly referred to as deep learning, these algorithms enable a computer to discover complicated patterns in very large data sets. Nowadays, these models are considered state-of-the-art in many tasks ranging from computer vision to robotics and natural language understanding. The sudden surge of interest in these areas began when a number of research works showed that these algorithms can outperform humans in many tasks, including visual classification and analysis tasks. The first and most prominent example was ImageNet [47]. In the Visual Recognition Challenge in 2012, ImageNet drastically decreased the error rate in image classification tasks. Deep convolutional neural networks used in such tasks now easily outperform humans in visual classification and recognition tasks. Aside from image analysis and visual pattern recognition, deep learning algorithms are being used for various tasks such as speech recognition and synthesis [48], and natural language processing [49]. Deep learning methods, specially deep convolutional neural networks (CNNs), are now being used in areas that were believed to be human-only task a decade ago. As an example, some research in medical image classification has shown performances surpassing human experts. A deep convolutional neural network model

called CheXNet [50] was able to outperform radiologists in detecting pneumonia from chest X-rays in a data-set with 100,000 chest X-rays images. There have been numerous other recent uses of machine learning approaches in medical sciences [51–54]. As a result of these drastic achievements in the past few years, deep learning methods have become a de facto standard for any tasks that needs to extract patterns from a large set of experiments or data points. Convolutional neural networks even entered the field of assisting in physical simulations of complex partial differential equations [55]. Despite all the progress in deep learning and computer vision in different domains, research that utilize these techniques for analysis and classification patterns generated from reaction-diffusion systems is sparse and almost non-existent. For this reason and the reasons outlined in this introduction, in Chapter 4 of this dissertation, we employ many algorithms from the machine learning domain to analyze and classify patterns generate in reaction-diffusion systems. We show that these algorithms prove to be very successful in many tasks that an ecologist or an experimental physicist encounters in the course of his/her research on pattern formation, classification, and analysis.

1.10 Dissertation Outline

The rest of the dissertation is organized as follows.

Chapter 2 introduces a set of hierarchical measures of robustness in networks to ensure various levels of stability against random loss of sites or bonds. We extensively investigate the critical point, critical behavior, and universality classes for these new measures of connectivity on the square lattice for both site and bond percolation. We show that some of these connectivity measures do not belong to the general percolation universality class in two dimensions.

Chapter 3 introduces a simple interacting multi-particle system, and we study the phase transition of connectivity and pattern formation of this system as a function

of time. We show that a continuous phase transition occurs in the dynamics of our model, and the critical exponents characterizing this transition are dependent on the parameters and initial conditions of the multi-particle system. We argue that this observation breaks the general observation of universality since universal behavior predicts that the critical exponents describing the critical behavior of such systems are independent of short-range interactions and even lattice structures.

In Chapter 4, we will investigate the use of various machine learning algorithms in classifying and quantifying patterns generated from reaction-diffusion systems. For this purpose, we utilize the Gray-Scott system of equations to generate various types of patterns since this system of equations can generate various types of patterns in different parameter regimes. We show that these algorithms can successfully classify reaction-diffusion patterns even in the settings where no prior information is given to them. We also formulate and solve the inverse problem of deducing reaction-diffusion constants given sample patterns and show that these algorithms are very effective and efficient in this task.

Chapter 5 focuses on future directions for each of the problems discussed in this dissertation. In this Chapter, I will try to delineate a number of open questions that can serve as the starting point for future research projects.

CHAPTER 2

PERCOLATION THRESHOLD FOR ROBUST NETWORK CONNECTIVITY

2.1 Introduction

In recent years, there has been impressive progress in our understanding of structural and dynamical properties of complex systems. Network science has emerged as a prominent field that provides us novel perspectives to better understand complexity [56, 57]. This is because many complex systems can be described with networks in which the entities are represented by nodes and the relationship between these entities are represented as bonds connecting these nodes. The dynamics of these complex systems can be modeled through the structural dynamics of the network as well as the dynamics on the network [58–60]. Structural transitions in networks have been the focus of numerous research studies in the past decades due to their importance in characterizing the performance of natural and man-made networks. These structural transitions affect many important network properties of networks, e.g. robustness to breakdowns [61, 62], cascading failures in networks [15], and epidemic spreading on social and technological networks. [63–65]. One of the most important properties of these networks is their functional and structural robustness to unexpected interruptions caused due to node and edge failures. At the hallmark of these studies, percolation theory [66] quantifies the robustness of networks by looking at the size of the largest *connected component* (LCC), i.e., the largest set of nodes of which each pair is connected by at least one path, as a function of a probability or a rate parameter that controls either random [62], localized [67, 68], or targeted [69, 70] node

and/or edge removals. A *percolation threshold* refers to the value of that parameter that separates a phase transition between two regimes of network connectedness—a set of small disconnected islands of connectivity on one side (the *subcritical regime*), and the existence of a giant connected component (GCC), a connected component of size proportional to the size of the network, on the other side (the *supercritical regime*). The sudden appearance of the GCC at this threshold is referred to as percolation. As the network goes deeper into the supercritical regime, the GCC becomes progressively more richly connected. Theoretical and numerical computation of percolation thresholds have been an ongoing challenge in the scientific community [71]. Due to the high complexity of the problem, analytical results exist only for very few lattice structures. On the other hand, numerical simulations have been shown very effective in determining the threshold for a range of regular and disordered lattices as well as random networks. The exponential increase in computational resources has paved the way for more precise calculations of percolation thresholds [72–75].

In many real-world applications, *barely* meeting the percolation threshold may not suffice to ensure robust network operation, since the GCC may be fragile and prone to disconnection with the failure of only a small fraction of nodes or edges. Further, even in the absence of actual failures, in certain networks, for example communication networks and biological networks [32], it is often desirable not only to be long-range connected but to have multiple paths connecting pairs of nodes in order to help control network congestion and support higher data throughputs. Therefore, there is a need to introduce more advanced measures of network robustness, which not only capture spanning connectivity but are also able to accommodate additional measure of robustness. Clearly, to meet any such additional robustness-driven constraint, the network must be pushed deeper into the supercritical regime of standard percolation theory. Expanding on ideas from percolation theory, researchers have studied other variants of percolation on different networks including k -core percolation [76–78],

k -clique percolation [79, 80], restricted valence percolation [81], and k -connectivity [31, 32].

In this chapter, we define and perform a comparative analysis of four intuitive measures of network robustness. We explain their inter-relationships, and also numerically evaluate the respective robust percolation thresholds for the square lattice. We leave connecting our robustness measures to application-specific robustness measures in real-life networks, for future work.

2.2 Robustness measures

The four robustness measures that we investigate in this chapter are depicted in Figure 2.1: (1) k -strong-connectivity, (2) k -connectivity [31], (3) k -core connectivity [76] and (4) k -stub connectivity [82]. The arrows in Figure 2.1 depict going from stronger to weaker measures of robustness. In other words, if a network is in the supercritical regime with respect to the stronger of two robustness models, it will also be so for the weaker one, but not necessarily vice versa. In each of the robust connectivity models, $k \in \{1, 2, \dots\}$ denotes the strength of the robustness setting, and each model is defined in a way such that $k = 1$ reduces each to the standard bond (or, respectively site) percolation model. Next to each measure of robustness in Figure 2.1, we write the condition that a robust k -connected component must satisfy under that measure of robustness. The network is said to percolate within any given robustness measure, when the size of the respective largest robust k -connected component is proportional to the size of the network itself.

In this Section, we formally define and explain the intuition behind each of these robustness measures. In Section 2.3, we define bond-percolation and site-percolation thresholds with respect to each of the measures, for the 2D square lattice, and interpret our results.

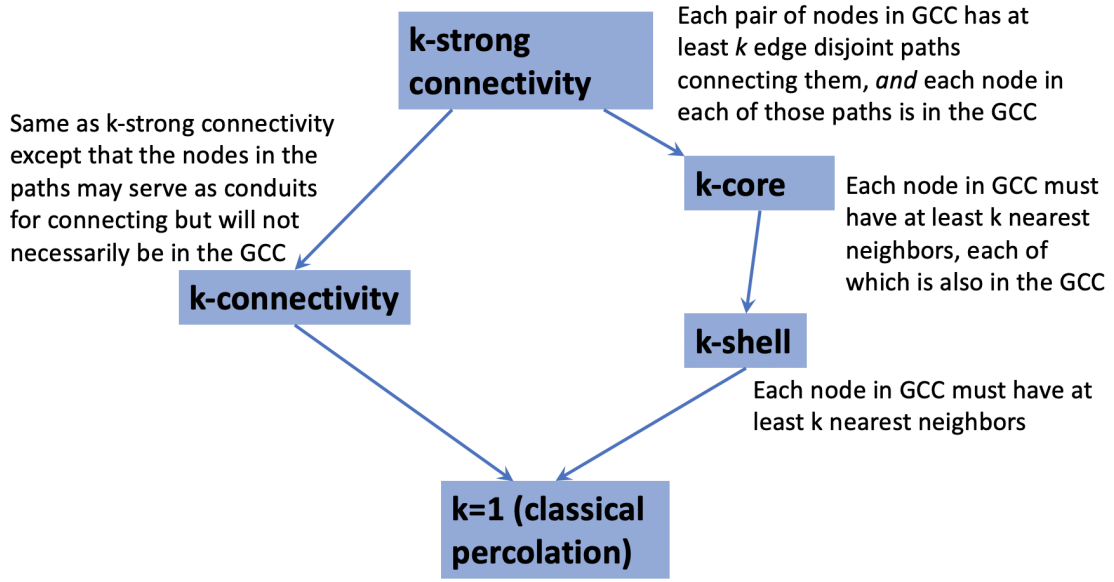


Figure 2.1: Models of robustness in connectivity. The arrows depict going from stronger to progressively weaker measures of robustness. In other words, if a network is in the supercritical regime with respect to the stronger of two robustness models, it will be so for the weaker one, but not necessarily vice versa.

1. **k -strong connectivity:** This is the strongest notion of robustness that we study. In this model, a k -connected component is a set of nodes such that every pair has at least k node-disjoint paths connecting them. The nodes in the paths must also satisfy this conditions and be a part of the k -strong component. This means that removal of $k - 1$ nodes from a k -connected component will not disconnect the rest of the nodes in that component.
2. **k -connectivity:** In this model, a k -connected component is a set of nodes in which each pair is connected via at least k node-disjoint paths. However those paths need not belong to the k -connected component. Newman *et. al* [31] showed that the percolation threshold for a configuration model random graph (any node degree distribution) is the same as that of standard percolation, although the absolute size of the GCC in the supercritical regime varies with k for $k > 1$.

3. **k -core connectivity:** In this model, a k -connected component is a set of nodes such that each node has at least k nearest neighbors each of which is also in the k -connected component. The concept of k -core connectivity and decomposing a complex network into its k -core components has been applied to several real-world networks, e.g., the Internet, the World Wide Web, and cellular networks [83].
4. **k -stub connectivity:** In this model, a k -stub connected component is a set of nodes such that each has at least k nearest neighbors (that need not belong to the k -component).

For any $k > 1$, there is a hierarchical relation between these four measures of robustness— k -strong-connectivity being the strongest of all, and regular percolation being the weakest. Connected components under these measures of robustness are nested per the hierarchies shown in Figure 2.1. For example, a 2-core connected component under the k -core model is always a subgraph of a 2-stub connected component under the k -stub model, which in turn is a subgraph of a regular connected component. There is no established hierarchical relationship between k -connectivity, and either the k -core or k -stub models.

2.3 Robust percolation thresholds

2.3.1 k -connectivity

k -connectivity is the best-known robustness measure studied in the literature. We call a subset of network nodes k -connected if each pair of nodes in that subset has at least k edge-disjoint paths connecting them. These paths can contain nodes that act as conduits to connect two nodes in the k -connected component while themselves not being part of the component. There are several algorithms for finding k -connected components for different values of k for a given graph. However, linear-time algo-

rithms are only known for the cases $k = 2$ and $k = 3$ [84]. For $k > 3$, polynomial-time algorithms exist to find the k -connected components of a graph [85]. To gain a better understanding of the behavior of k -connected components, we restrict ourselves to site and bond percolation on the 2D square lattice. Despite percolation on 2D square lattice being a widely studied problem, to the best of our knowledge there is no literature on k -connectivity properties of percolation clusters (in the sub-critical and super-critical regime). Grimmett [86] showed that the bond percolation threshold of the square lattice is given by $p_c = \frac{1}{2}$ and stated the following theorem:

Suppose B_n is an n by n square grid centered at the origin. Let M_n denote the maximal number of (pairwise) edge-disjoint left to right paths crossings B_n . Then, for any $p > p_c$ there exist positive constants $\eta = \eta(p)$ and $\lambda = \lambda(p)$ such that:

$$P_p(M_n \leq \eta n) \leq \exp(-\lambda n)$$

where $P_p(M_n \leq \eta n)$ denotes the probability of occurrence of event $M_n \leq \eta n$. This means that there exists order n disjoint left-right crossings of box B_n when $p > \frac{1}{2}$.

Using the rotation invariance of the square lattice under $\frac{\pi}{2}$ rotations, we see that the theorem is true for up-down disjoint crossings of the box with sides of length n . This means that above the percolation threshold there exists order n disjoint left-right and order n disjoint up-down crossings of a box B_n . Also, using translational invariance of the square lattice, we know that this is true for any square box with sides of length n . Using this result, we now can superimpose a renormalized square grid Figure 2.2 using the left-right and up-down disjoint crossings of the square lattice. This ensures that we can have a renormalized square grid of order $\Theta(N)$ sites above the percolation threshold in a bond percolation model. Since all of the intersections of the disjoint crossings on the square grid have at least degree 3, the renormalized grid ensures the existence of giant 2-connected and 3-connected components with sizes of order $\Theta(N)$. However, it does not necessarily guarantee the existence of a giant 4-connected component since we need order $\Theta(N)$ degree 4 disjoint crossing

intersections in the infinite connected component to guarantee the existence of a giant 4-connected component. Our numerical results illustrate that the percolation threshold for 4-connectivity is above the regular threshold for global connectivity.

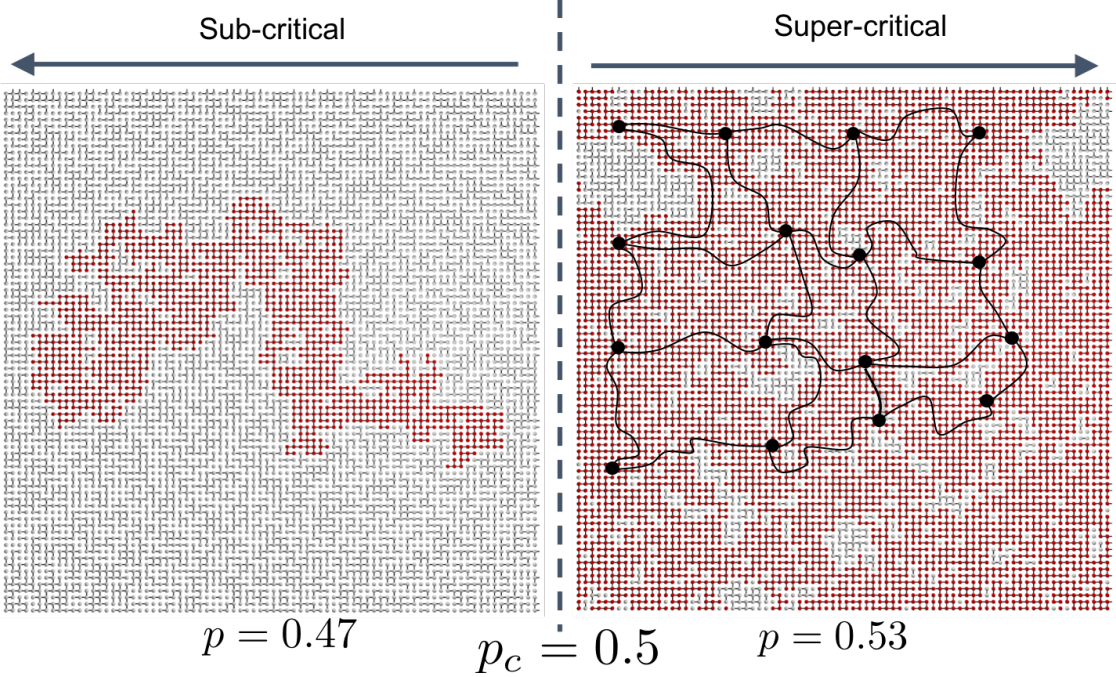


Figure 2.2: The renormalized grid made by joining the disjoint crossings

We verified our theoretical results with numerical simulations [84]. Figure 2.3 shows the percolation threshold for k -connectivity for $k = 1, 2, 3$ for site and bond percolation on square lattice. As observed from the figure, bond percolation thresholds for $k = 1$ to $k = 3$ are the same and equal $p_c = \frac{1}{2}$.

The algorithm for determining the percolation behavior of our model is similar in spirit to the fast percolation algorithm of Newman and Ziff [87] in which we start with an empty graph and randomly occupy bonds one by one until we occupy all the bonds in the square grid. Our simulation results are based on implementations of algorithms developed by Hopcroft et al. [84] and Gutwenger et al. [88] to find the 2-components and 3-components of a given instance of the network.

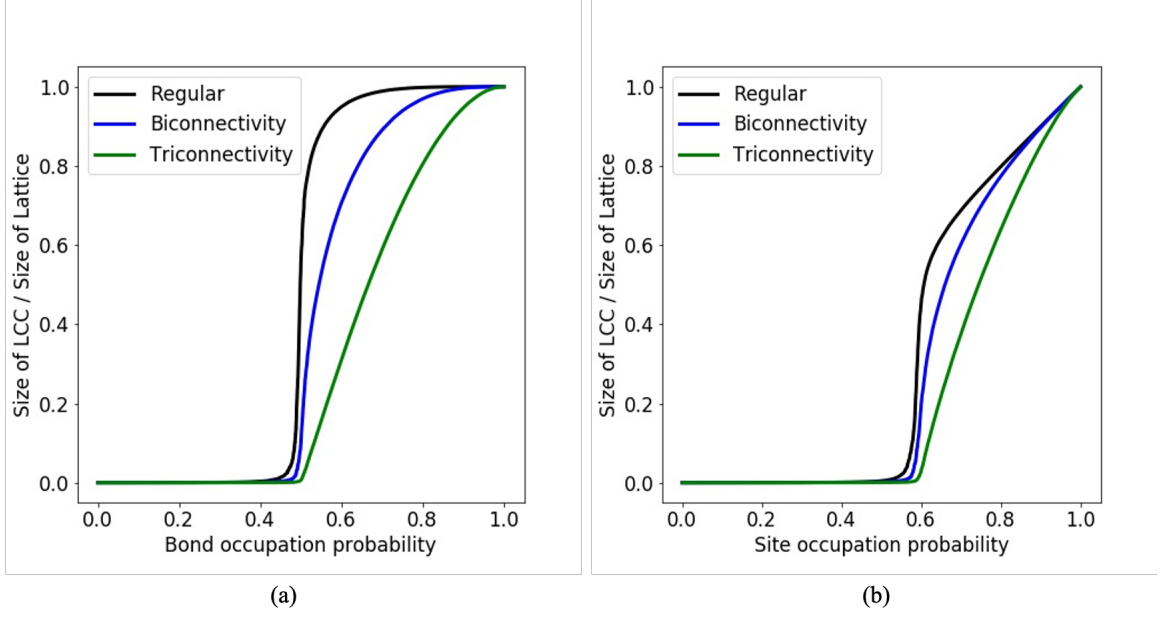


Figure 2.3: (a) k -connectivity for bond percolation on square lattice. The critical threshold is $p_c = 0.5$. (b) k -connectivity for site percolation on square lattice. The critical threshold is $q_c = 0.5927$.

2.3.2 k -strong-connectivity and k -core

k -strong-connectivity, which is less prevalent in the literature and is our strongest robustness measure, demands that every pair of connected nodes in the subset have at least k disjoint paths between them and that nodes on these paths belong to the k -strong-component. The k -core of a network is obtained by recursively removing nodes with degree less than k until no such nodes exist in the network. k -core decomposition has been applied to many real-world networks (the Internet, the World Wide Web, cellular networks, etc.) [89,90] and has become an important tool for visualization of complex networks and interpretation of cooperative processes in them. The critical behavior of k -core in the site percolation setting has been studied before for various types of lattices, including cubic and triangular lattices [91,92]. Here we study the critical behavior of k -core and numerically show that for square lattice, the percolation threshold for k -core is the same as for k -strong-connectivity for all k and is the

same as k -connectivity for $k = 2$. It is evident that for $k = 2$, a k -strong-component is the same as a k -component. This is because the nodes that act as conduits in the case of 2-connectivity are parts of cycles in the network and all the nodes in a cycle have 2 disjoint paths between them and so are k -strongly connected. We also argue that for $k = 3$ on the square lattice with non-periodic boundary conditions, the percolation threshold for k -strong connectivity is the same as k -core and is equal to one. In order to have a k -core, all the nodes in the component need to have degree k or higher than k . The simple square lattice without periodic boundary conditions has four degree 2 nodes on its corners, in order to have a 3-core, we need to remove those nodes and continue the process until there are no nodes with degree smaller than three. This results in the deletion of all of the nodes in the square lattice. Therefore, the threshold for $k = 3$ for k -core and k -strong-connectivity is one in a square lattice with no periodic boundary conditions. However, for a square lattice with periodic boundary conditions, the only configuration in which we can have a non-zero 3-core is a configuration that has a wrap around. The reason is that any configuration that has not wrapped around the torus has a corner that has degree smaller than three which results in the deletion of all of the nodes in the graph during the k -core pruning process. Our numerical results indicate that the 3-core component and the 3-strong connected components are exactly the same with the same participating nodes. This is an interesting observation, since one can come up with counter-examples in which a 3-core component is not 3-strongly connected on the square lattice with periodic boundary conditions, however, the occurrence of such configurations is unlikely because of being extremely ordered. Fig. 2.4 shows an example of such a configuration. There are only 2 node-disjoint paths from node **A** to **D**, one of which passes through **B** and the other passes through node **C**. Nodes **B** and **C** are the only connection points between the left and the right part of this component. However, in order for this configuration to exist, all the edges inside the left and right sides of the compo-

ment should exist. As argued above, the configuration must have wrap-around edges that connect two sides of the square lattice to avoid having nodes with less than 3 connections. Other similar counter-examples could exist but they must satisfy the same requirements to maintain being a 3-core. As the lattice size grows, the probability of observing such structures diminishes, a fact that is confirmed by non-appearance of such configurations in our numerical simulations.

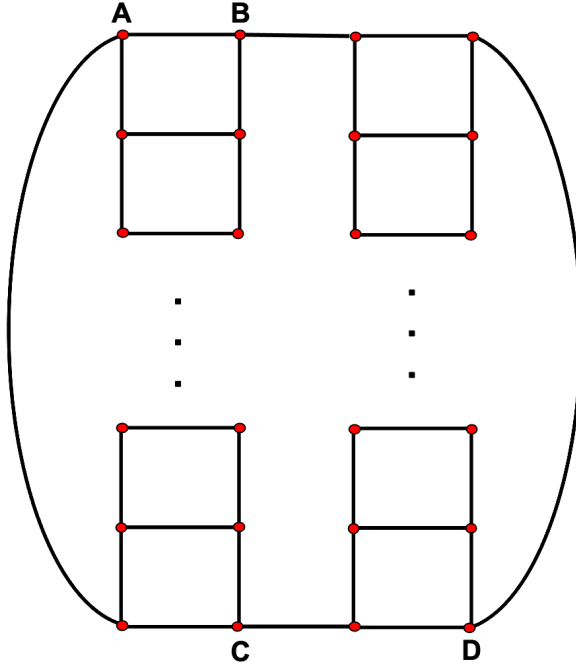


Figure 2.4: Counter-example showing possibility of non-equivalence of 3-core and 3-strong component on square lattice with periodic boundary conditions.

We further numerically investigated the nature of k -core transition and the exact point of criticality using finite size scaling. It is worth noting that, in general graphs the critical behavior for k -core percolation can be different from that of k -strong-connectivity.

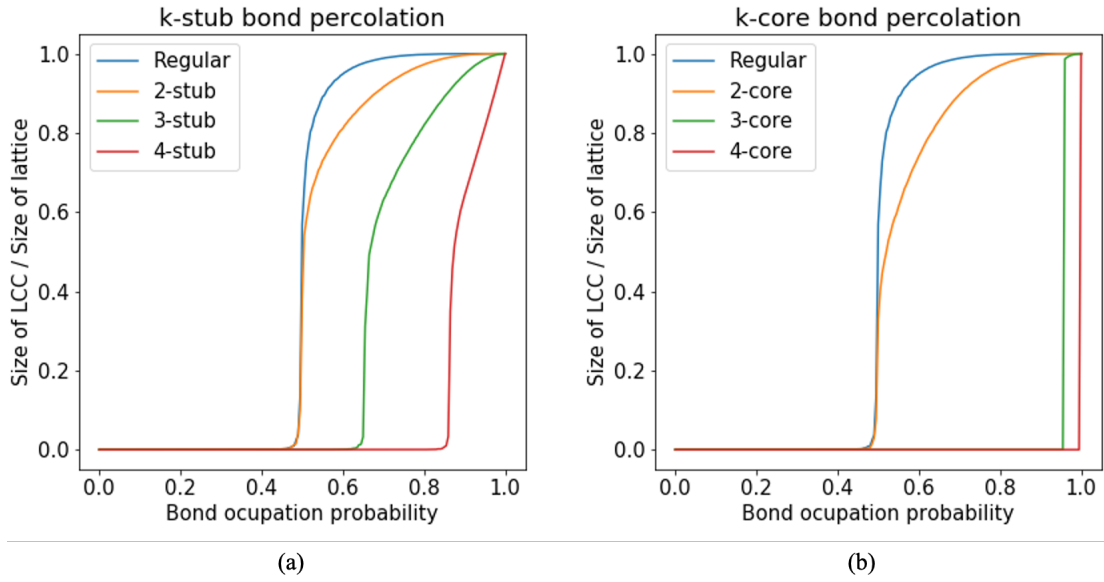


Figure 2.5: (a) k -stub of square lattice for bond percolation. The critical threshold for 4-stub is smaller than 1; (b) k -core of square lattice. Note that the curve for 2-core, 2-connectivity and 2-strong-connectivity are exactly overlapping.

2.3.3 k -stub

The k -stub of a graph is obtained by executing only one iteration of the algorithm for finding the k -core of the graph. We propose an efficient online algorithm similar to one described in [87] to find the percolation properties of k -stubs of graphs using dynamic updates after the addition of each node. In this algorithm, which is based on the union-find data structure, we store extra information on the degrees of nodes. After each node addition, we update the degrees of neighboring nodes and check if they exceed k . If the degree of any of the neighboring nodes exceeds k after an addition, we add it to the union-find structures that store the k -stub components of the graph. This algorithm cannot find the k -core of the graph since the addition of each node could result in non-local changes to the k -core components and tracking these non-local changes will increase the computational cost of these dynamic updates.

As can be observed in Fig. 4(a), the percolation threshold for 4-stub is strictly below 1.

2.4 Finite Size Scaling

In order to better characterize the nature of robustness measures in this chapter, we make use of finite size scaling [93, 94], a well-known technique developed for numerical analysis of phase transitions. In second-order (continuous) phase transitions, every variable X near the critical threshold p_c is scale-invariant. This phenomenon appears due to the divergence of correlation length at p_c . Therefore, X has the following power-law form.

$$X \sim |p - p_c|^\omega \quad (2.1)$$

where ω is the critical exponent for variable X . On a finite system of size N and length L , the variable X has the following scaling form near the threshold

$$X = L^{-\frac{\omega}{\nu}} F \left[(p - p_c) L^{\frac{1}{\nu}} \right] \quad (2.2)$$

where ν is the correlation length critical exponent and F a universal function. At $p = p_c$, the scaling function F converges to a constant and variable X follows a simple scaling relation,

$$X \sim |L|^{-\frac{\omega}{\nu}}. \quad (2.3)$$

Using Monte Carlo simulations of different size systems at $p = p_c$, one can deduce the critical exponent ratio $\frac{\omega}{\nu}$ of the variable using the scaling relation in (2.3). In this work, following an approach similar to [94], we adopt the two main variables commonly used to characterize percolation transitions, i.e. the percolation strength P and the average cluster size S . The percolation strength P_∞ is defined as the

relative size of the largest cluster with respect to the total system size N . The scaling relation of P is

$$P_\infty = L^{-\frac{\beta}{\nu}} F^{(1)} \left[(p - p_c) L^{\frac{1}{\nu}} \right] \quad (2.4)$$

where the critical exponent is β . Here P is the order parameter of the transition. The second variable we use in our numerical simulations is the truncated average cluster size S defined as

$$S = \frac{\sum_s n_s s^2}{\sum_s n_s s} \quad (2.5)$$

In the above equation, n_s stands for the number of clusters of size s per node. Since the percolating cluster diverges above p_c , the sum in (2.5) runs over all cluster sizes except that of the largest cluster. The scaling relation of S is

$$S = L^{\frac{\gamma}{\nu}} F^{(2)} \left[(p - p_c) L^{\frac{1}{\nu}} \right] \quad (2.6)$$

Where γ is the critical exponent related to average cluster size. In lattice percolation, the exponents β_L , ν_L and γ_L (where subscript L stands for lattice) are linked by the so-called hyper-scaling relation [95],

$$\frac{\gamma}{\nu} + \frac{2\beta}{\nu} = d \quad (2.7)$$

where d is the dimension of the lattice.

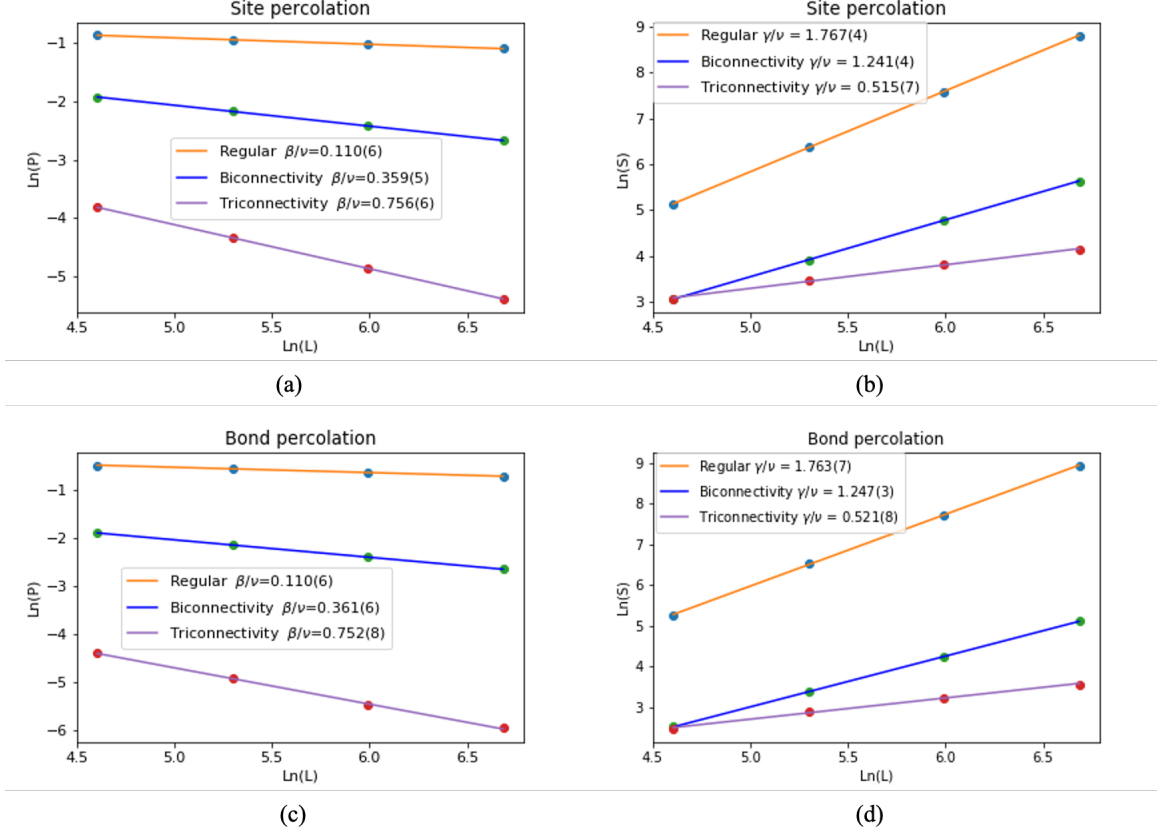


Figure 2.6: Exponents $\frac{\beta}{\nu}$ and $\frac{\gamma}{\nu}$ for regular percolation, 2-connectivity, and 3-connectivity (a),(b) $p_c = 0.5927$ and (c),(d) $q_c = 0.5$. The linear nature of these scaling exponents verifies the fact that we are at the percolation threshold.

2.5 Numerical Results

It is known from percolation theory that in regular percolation, the order parameter changes continuously across the transition. This critical behavior is known as continuous or second-order phase transition. On the other hand, first-order or continuous phase transitions are characterized by a discontinuity in the order parameter of transitions [96]. There is also a class of transition known as hybrid transition that combines a first-order discontinuity with a second-order transition [97].

We examined the critical exponents for all the defined robustness measures. Based on our numerical analysis, the critical behavior of k -stub for all k as well as k -core and

k -strong-connectivity for $k = 2$ is similar to 2-connectivity with similar corresponding exponents. Besides, as shown in the literature [97], our results confirm the fact that k -core for $k > 2$ exhibits a hybrid phase transition combining a discontinuity and a critical singularity that breaks the usual scenario of ordinary percolation. The critical behavior of k -connectivity was found to be different from the percolation universality class. Hence, we report results corresponding to this robustness measure.

Figure 2.6 shows plots for finding critical exponents for bi-connectivity and tri-connectivity, the linear behavior of the curves verifies our theoretical results about the percolation thresholds of these robustness measures on the square lattice. As expected the exponents follow the hyper-scaling relation in (2.7) with a small margin of error that ensures that we indeed observe a second-order phase transition in two dimensions. The values corresponding to $\frac{\beta}{\nu}$ and $\frac{\gamma}{\nu}$ are different from the regular percolation universality class and to the best of our knowledge, do not belong to any known universality class. Shlifer et al. [98] showed that the correlation length exponent ν for bi-connectivity is the same as ν in percolation universality class. Given $\nu = \frac{4}{3}$, we obtain $\beta = 0.48$, which is consistent but slightly lower than previous results, Shlifer [98], $\beta = 0.50$ and Sahimi [99], $\beta = 0.542$. It is also worth noting that the critical behavior of tri-connectivity and bi-connectivity are similar in both bond and site percolation, which is expected since the underlying transition in two dimensions should belong to the same universality class.

Tables 2.1 and 2.2 show the percolation thresholds for all our robustness measures. We were not able to find the exact percolation threshold for 4-connectivity due to its computational complexity; however, our results confirm the fact that the percolation threshold for this robustness measure is above the regular percolation threshold.

Table 2.1: Bond percolation thresholds

	k-connectivity	k-stub	k-core	k-strong-connectivity
k=1	0.5			
k=2	0.5			
k=3	0.5	0.6603(4)	0.9692(1)	0.9692(1)
k=4		0.8655(3)	1	1

Table 2.2: Site percolation thresholds

	k-connectivity	k-stub	k-core	k-strong-connectivity
k=1	0.5927			
k=2	0.5927			
k=3	0.5927	0.7356(3)	0.9747(1)	0.9747(1)
k=4		0.8846(4)	1	1

All simulations reported in the Chapter were performed using a Linux based compute cluster. For all robustness measures, systems with sizes $L = 100, 200, 400, 1000$ were simulated. For k -stub for all values of k and L , 10^6 realizations were generated using the modified Newman-Ziff algorithm introduced in Section 2.3.3. For the other three robustness measures, 10^6 realizations were simulated for the smallest lattice ($L = 100$), and for all other lattices including the largest lattice ($L = 1000$), this number was always $> 10^5$.

2.6 Conclusion and Future Work

We numerically evaluated various percolation phenomena for several robustness measures for the square grid. We showed that k -stub for all k , and k -strong-connectivity and k -core for $k = 2$ belong to the percolation universality class in two dimensions. We showed that critical exponents for k -connectivity belong to different universality classes for different k and calculated the corresponding exponents for $k = 2, 3$. In addition, we report percolation thresholds for all the robustness measures and show that on the square lattice, the percolation threshold for k -connectivity for $k = 2, 3$, and

k -core, k -stub, and k -strong-connectivity for $k = 2$ are equal to the ordinary percolation threshold. In ongoing work, we are applying these connectivity-based network robustness measures to the design and control of software-defined wireless networks to realize distributed analytics that is robust to network dynamics [100]. Furthermore, one of the main future directions of this work is to investigate the critical behavior of these connectivity measures in other network configurations and lattice structures.

CHAPTER 3

PHASE TRANSITION, PATTERN FORMATION AND VIOLATION OF UNIVERSALITY IN A NONEQUILIBRIUM PERCOLATION MODEL

Classical percolation theory mainly deals with statistical properties of connected components in systems with independent components. The probability of occupying a site or bond on the square lattice percolation does not depend on the number of occupied sites in the lattice or the neighborhood of the site or bond. However, when system under study is a system of interacting particles and the phase transition occurs as the dynamics of the system unfold, this assumption no longer holds and behaviors aberrant from ordinary percolation are expected.

In this chapter, we introduce an interacting multi-particle system. We study the dynamics of this system on the square lattice. In particular, we study the phase transition of connectivity as a function of time. We show that there is a sharp loss of long-range connectivity resembling a continuous phase critical phenomena in the time-evolution of the system. We utilize the finite-size scaling techniques introduced in chapter 2 to investigate its critical behavior. Our numerical studies show that this varying parameters of the interaction as well as initial conditions, continuously changes the critical exponents of the transition. As introduced in the first chapter, the concept of universality revolves around the observation that critical exponents explaining continuous phase transitions do not depend on the microscopic details of the system and only depend on few parameters like dimensionality or symmetries of the system. For this reason, our observation violates the general notion of universality. However, we show that it can still be categorized under *weak universality* which was

recently introduced to explain certain rarely observed critical phenomena. During the time-evolution, our system also undergoes different stages of pattern formation. Multiple filamentation patterns, resembling the ones formed in laser filamentation, occurs when the system is undergoing phase transition of connectivity. We qualitatively show that the types of these patterns change as we vary the interaction parameter.

3.1 Introduction

Interacting-diffusing systems of particles or agents have recently been the focus of many research fields ranging from statistical physics [101] to ecology [102]. These systems exhibit interesting phenomena and can give rise to complex collective behaviors such as non-equilibrium critical phenomena [103], pattern formation, self-organization [102], and collective motion [104]. Complex collective behaviors can arise when the particles or agents follow very simple rules that only depend on their local neighborhoods. Aside from physical sciences, these systems have attracted much attention from engineering fields like materials engineering [105–107] and robotic swarm engineering [108, 109]. The goal of these researches is to design simple agents that can be engineered to exhibit robust collective behaviors at different scales [110, 111].

Non-equilibrium critical phenomena have recently been extensively studied. Similar to equilibrium critical phenomena, the notion of universality is the major tool to study and categorize phase transitions in these systems. Prominent examples that exhibit non-equilibrium phase transitions include kinetic Ising models [112], non-equilibrium growth models [113] diffusion-limited reactions [114], absorbing phase transitions [115, 116], sandpile models [117], and generally lattice models or cellular automata. Many of these systems belong to the general schema of the Directed Percolation (DP) universality class. Janssen and Grassberger hypothesized that models which exhibit a continuous phase transition to a single absorbing state belong to the DP universality class [115, 116]. Other universality classes occur when we add new

symmetries or other constraints such as particle conservation to the model. In particular, the effect of particle conservation on universality has been extensively studied in the literature [118], and it has been shown that these systems belong to a universality class other than Directed Percolation class [119]. Examples include the conserved threshold transfer process (CTTP) [118], the conserved lattice gas (CLG) [118], the well known Manna sandpile model [120].

These simple lattice models of interacting particles have shed a great deal of light on the behavior of non-equilibrium critical phenomena. However, most of these works focus on critical behavior in terms of steady state density fluctuations and rarely investigate dynamic transitions in the time domain as particles interact and reach steady-state distribution. More importantly, there are rare instances [2–4, 121] in the reaction-diffusion literature in which the order parameter of the critical phenomena under study is the connectivity of the system as defined in percolation theory [2–4, 121].

This chapter introduces an interacting driven diffusive system on a lattice with finite-range interactions. It is worth noting that this model could be implemented and studied on any general graph structure. We empirically study the phase transition of global connectivity in this lattice system. In addition, to the observation of a phase transition in connectivity in our proposed system, we show that our model shows a continuous variation of exponents as we change specific parameters of the model and, therefore, breaks the usual universality paradigm. We will show that our results conform with the literature on weak universality, rarely observed in other physical systems [122]. We further connect our work to the existing literature on interacting self-propelled agents in continuous space. We implement the model introduced in Mijalkov et al’s work [5] and study the evolution of connectivity as the dynamics of their model unfold. We show that the phase transition of connectivity is also present in this continuous density-driven multi-agent system. These observation open up new

opportunities for further research in multi-agent or multi-particle systems in which the global connectivity of the system as a function of time is of importance, i.e. software defined networks [123, 124]. In addition, to the observation of a phase transition in connectivity in our proposed system, we show that our model shows a continuous variation of exponents as we change specific parameters of the model and, therefore, breaks the usual universality paradigm. We will show that our results conform with the literature on weak universality (see Related Work section), rarely observed in other physical systems [122].

During the dynamics of the transition, our model goes through a series of pattern formation phenomena, namely, from a disordered state to filamentation patterns and eventually to patterns of distributed spots. The occurrence of a dynamic phase transition in connectivity and regimes of pattern formation resembles the dynamics of a high power laser passing through a nonlinear Kerr medium [4, 125]. Pattern formation in driven-diffusive systems is usually described by Turing’s activator-inhibitor dynamics [126]; however, there is an alternative approach developed by Cahn and Hillard in 1958 [127]. They studied pattern formation in mixed fluids and observed that density-dependent rates of dispersal can lead to the separation of fluids into distinct spatial regions. Many studies have since shown that the occurrence of patterns in many natural systems such as bacterial colonies [128] or mussel beds [102] can be explained using Cahn-Hilliard’s density-driven interactions [129]. Similarly, the patterns observed in our model are in principal density-driven patterns.

3.2 Related Work

3.2.1 Non-equilibrium Phase Transitions

Continuous phase transitions are abundant in nature and less understood compared to equilibrium phase transitions. Systems that demonstrate non-equilibrium transitions range from surface growth [113], traffic jam [130], epidemic spreading [131],

laser propagation [4], to ecological phenomena and forest fires [132]. Experimental studies have shown that the concept of universality that is mostly applied to equilibrium systems can be successfully applied to non-equilibrium transitions. However, the critical behavior and the universality classes of non-equilibrium systems are anticipated to be more diverse since these systems have new degrees of symmetry in the time domain and are governed by evolution dynamics. One of the most prominent examples of non-equilibrium phase transitions is Directed Percolation (DP) [133]. Directed percolation belongs to the more general class of absorbing-state phase transitions. These systems show a phase transition to a dynamically active/inactive state as a control parameter is varied. A multi-particle system with absorbing transition may fall into an absorbing state where all particles cease to move, and there are no density fluctuations. On the other hand, the system can transition to a regime where there are active density fluctuations when the system is in the steady state. These systems are usually studied by continuously varying a control parameter (i.e., initial particle density in percolation transitions, temperature in Ising systems, etc.) and observing a sudden transition in the order parameter in the infinite time limit. However, in some works in the literature, the control parameter is time, therefore they study spontaneous transition of the control parameter as the dynamics of the system unfolds [134].

3.2.1.1 Percolation Transitions in Reaction-Diffusion Systems

Gimel et al. [2] studied the gelation of the diffusion-limited cluster aggregation (DLCA) process [37, 38] on a cubic lattice. The initial stage of their simulation consists of randomly distributing N_0 particles on the lattice sites. The evolution of the particles is defined by the following rules. If two particles are near neighbors, they link up irreversibly and become part of the same cluster. The mass m of a cluster is defined as the number of particles forming the cluster. A Brownian motion is assumed

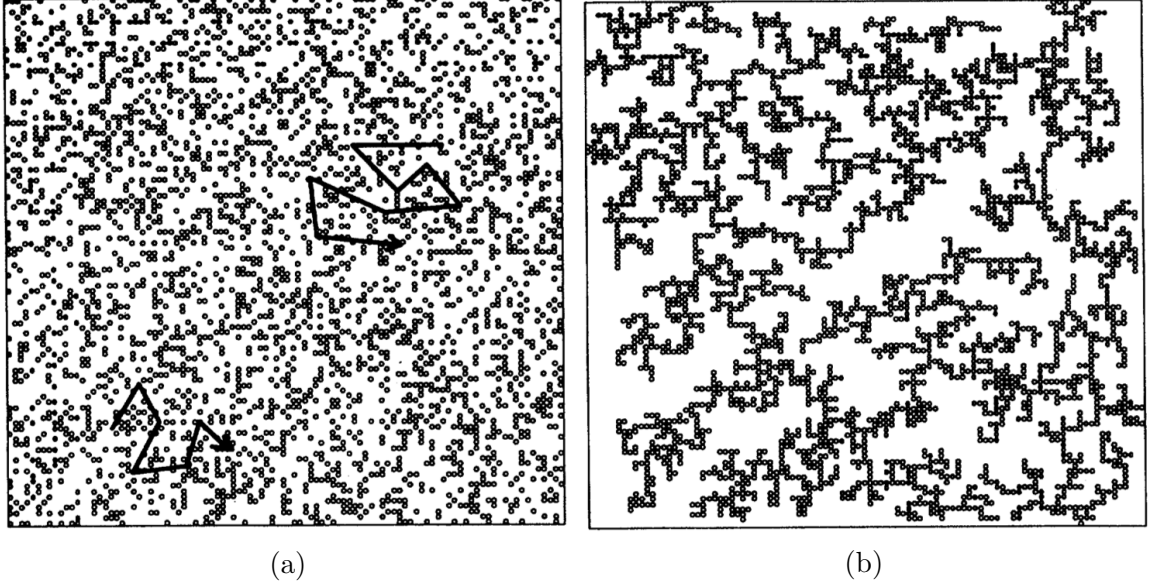


Figure 3.1: (a) Initial random configuration of particles on the lattice. (b) Configuration after running the dynamics and reaching the termination criteria. The single large cluster has spanning connectivity through the lattice. Images taken from [2]

for each cluster in the system, and the diffusion coefficient of a cluster is related to its mass as $D(m) = m^{-\alpha}$, where α is a positive exponent. They assume excluded volume interactions meaning that only a single particle can occupy each site. The simulation ends if there is only one cluster in the system or if there is spanning connectivity in the lattice. (Note that the initial configuration is below the site percolation threshold of the lattice). Fig. 3.1 shows how the DLCA process evolves from an initial state of randomly dispersed particles to a final state of a single large cluster that spans the lattice. The final state of the DLCA process shows interesting pattern formation behavior resembling filamentation patterns observed in activator-inhibitor systems. They extensively study the probability of ending up with a spanning cluster as a function of the initial particle density and show a percolation-like phase transition.

In similar work, Bruschi et al. [3] studied the percolation properties of thin metal film growth. They modeled thin metal growth by considering adsorption, diffusion, and re-evaporation of single atoms on a triangular lattice. Similar to the previous

work, they assume that each lattice site can at most accommodate a single particle. We will briefly explain atoms aspects of the dynamics of their model since the laws governing their model have interesting analogies to our work. Of most importance to us are the laws governing the diffusion rate of the atoms on the lattice. The following equation defines the diffusion rate between neighboring lattice sites i and j :

$$r_{ij} = r_0 \exp\left(\frac{-E_{ij}}{kT}\right) \quad (3.1)$$

In the above equation, r_0 is a constant, and E_{ij} is the activation energy of the transition. The activation energy is determined by taking into account the cumulative occupancy of the nearest neighbors of the diffusing particle. They simulate this system at different temperatures and study the phase transition of connectivity as a function of filling factor p , which measures the fraction of sites containing a particle divided the lattice size. In Fig. 3.2 we see that as we change the temperature, the percolation threshold of the system is shifted to a new location. This is interesting behavior that we also observe in the dynamics of our model.

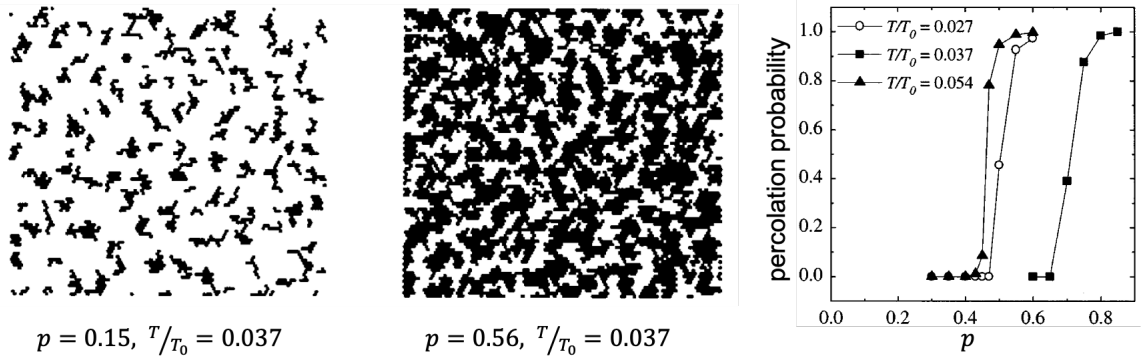


Figure 3.2: First two images show the clusters formed in the lattice at two different filling factors (points in time) and at a fixed temperature. The last image shows the behavior of the phase transition of connectivity at different temperatures and different filling factors. Images taken from [3]

In more recent work, Etoumi et al. [4] studied the phase transition of connectivity in high density regions of a laser beam passing through air. They showed that during the evolution of the dynamics, high-density regions of the laser beam undergo a phase transition in connectivity (Fig. 3.3), meaning that after a certain point in space (time), the filaments formed by the laser beam lose global connectivity and form large number of small clusters. Their experimental and simulation results show that the phase transition does not belong to any previously known universality class.

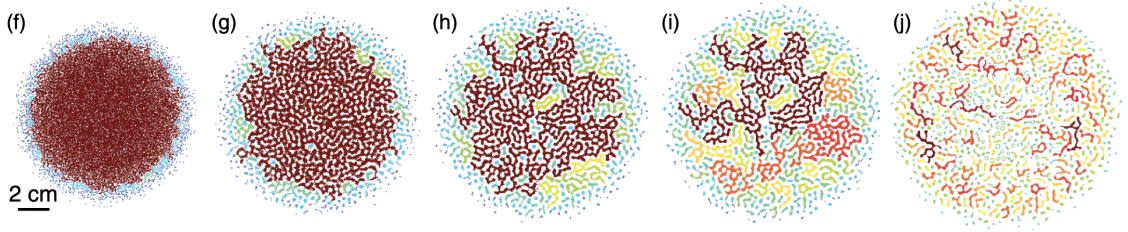


Figure 3.3: Evolution of the fluence profile of a high power laser beam propagating in air [4]. The laser beam forms a large cluster of connected sites at the beginning (dark red cluster in (f)). As it propagates, it forms filamentation patterns and the connectivity of the beam is lost (scattered connected clusters in (j)).

Apart from the related work cited above there are some recent works in the field of temporal percolation in diffusion-based processes or in activity-driven networks; Kantor and Kardar [135] studied the temporal percolation of sites not removed by t steps of a random walk. Starnini et al. [121] studied temporal percolation in activity-driven networks. Valdez et al. [136] studied the temporal percolation of a susceptible adaptive network.

3.2.2 Continuous Varying Exponents and Violation of Universality

The concept of universality is at the center point of the study of critical phenomena. Universality in critical phenomena revolves around the main experimental and theoretical observations: Critical exponents and scaling functions are universal up to symmetries and dimensionality of the system. Although the concept of universal-

ity has been confirmed countless times, there are rare reports of systems in which the critical exponents vary continuously [137]. Some examples include the work of Baxter, who solved the eight vertex model [138]. Later, Kadanoff and Wegner [139] provided a mapping of eight vertex model to a two-layer Ising model with four-body interaction between the layers [140]. This four-body interaction drives the continuous variation of exponents. In 1974, Suzuki [122] proposed a weak universality paradigm in which the critical exponents (like β , ν , γ) can continuously vary while their ratios ($\frac{\beta}{\nu}$, $\frac{\gamma}{\nu}$) remain constant. The underlying feature that separates these systems from systems showing regular universality is yet to be known. Since its introduction, weak universality has been observed in some systems including non-equilibrium absorbing phase transitions [137], frustrated spin systems [141], quantum critical points [142], interacting dimers [143], Fortuin–Kasteleyn random-cluster model [144], etc.

Newman [145] studied a three-species reaction diffusion system and showed that the critical exponents describing the power-law behavior of the density-field vary continuously with reaction-diffusion parameters. Janssen et al. [146] reported that Levy-type long-range flights lead to a continuous variation of critical exponents in the context of absorbing phase transitions. Noh et al. [147] studied a variant of pair contact process with diffusion (PCDP). In their model, they introduce a parameter that controls the strength of long-term memory (long-term correlation with previous positions.). They showed that by varying this parameter, they can continuously tune the critical exponents of the phase transition. Andrade et al. studied a percolation model on a diamond hierarchical lattice where the percolation transition is retarded by the inclusion of a probability of erasing specific connected structures. They show that critical exponents ν and β of the investigated model vary continuously as the erasing probability changes. Interestingly, tuning the erasing probability can lead to $\nu = \infty$ in their model. Cho et al. [148] observe a continuous change in critical exponents in a model of network growth. In their network growth model, they randomly select

two nodes to connect with the constraint that one of these nodes must be selected from a set of smallest clusters. The number of clusters which belong to this set is defined by parameter g . This correlated growth model increases the sharpness of the transition observed in regular percolation models. They further show that by varying g , they can vary the phase transition critical exponents. Here, similar to explosive percolation [36], their network growth process assumes global information about all the clusters present in the percolating system.

Long-range interactions, global information, and long-term memory effects are characteristics observed in many systems that violate the general concept of universality. The model introduced in this chapter shows a continuous variation of critical exponents as depicted in the weak universality paradigm. To the best of our knowledge, our model is the first example of such behavior observed in single-type driven diffusive systems that lack long-range interactions like levy flights.

3.2.3 Pattern Formation

Although different regimes of pattern formation have been abundantly reported in various areas of physics, we would like to focus our attention on a specific class of such pattern formation phenomena, namely single-type particle systems with density-driven motility. Originally Turing [39] introduced the activator-inhibitor principle, which provides a potential theoretical explanation for the formation of many of regular patterns in nature [40, 149, 150]. The underlying principle is based on the diffusive interaction of a local positive activating feedback with a large-scale inhibitory feedback. This activator inhibitor principle can account for many naturally occurring phenomena like growth, birth, mortality, decay, respiration, etc. Theoretical studies by Cahn and Hilalrd in 1958 [127] offer another mechanism for pattern formation. They discovered that density-dependent rates of diffusion can separate mixed fluids into two phases in spatially distinct regions. Switching between aggregation and diffu-

sion when the local density changes explain many pattern formation phenomena [151] like multi-phase fluid flow [152], mineral growth [153], population dynamics in ecological systems and flocking [102]. Spineanu et al. [154] showed that the multiple filamentation patterns observed in Fig. 3.3 can be explained using the Cahn-Hilliard density-driven model. In another work inspired by density-driven motility in bacterial colonies, Mijalkov et al. [5] studied the collective behavior of interacting autonomous robots in a continuous plane. The interaction rule and the velocity of the robots depend on the density of the fields generated by other neighboring robots. They observe pattern formation behavior typical to previously mentioned single species systems (Fig. 3.22). The local density-driven motility introduced in our model is inspired by the aforementioned works and shows various stages of pattern formation. We also investigate the percolation behavior of Mijalkov et al.'s model [5] and show that there occurs a phase transition in connectivity as the robots evolve from an initial state of random positions to a state of isolated clusters.

3.3 The model

Inspired by the notion of single specie density dependant dynamics observed in many physical systems ranging from bacterial population dynamics to high energy laser propagation in Kerr media, we propose a simple model of interacting-diffusing particles.

Our proposed model is based on a simple local density-dependent interaction model between diffusing particles on a discrete lattice or a graph. In this model, at each simulation time step, a particle observes the number of particles on the site it resides on and the total number of particles on the neighboring sites. The following set of rules determines the probability of a hop. Let n_i denote the number of particles co-populating a lattice site i . Each site on the lattice has 4 nearest neighbors. We define m_i as follows:

$$m_i = \sum_{j \in \text{nearest neighbors}} n_j \quad (3.2)$$

The above sum runs over all the nearest neighbors of site i . If $n_i > m_i$, the chosen particle hops to one of the randomly chosen neighboring sites. If $n_i \leq m_i$, the particle hops to one of the randomly chosen neighbors with probability $e^{-(n_i - m_i)^\alpha}$ and stays on the same site with probability $1 - e^{-(n_i - m_i)^\alpha}$. Each time-step consists of going over all the particles in the lattice in parallel and updating the location of all the sites. The dynamics of the interacting particle model depend on the initial distribution of the particles as well as the connectivity structure of the Lattice (In this case square lattice).

Fig. 3.4 shows the dynamics of the model on a square lattice of size 128 with uniform initial conditions. At $t = 0$, one particle is placed on each site. In order to better visualize the dynamics, the per site particle density is shown using the color-bar. At $t = 0$, the system starts from a uniform density profile across the lattice. As time passes, the particles form random high-density points, which act as an aggregation point for any incoming free particle. This results in the formation of sparsely scattered spots of high-density clusters as we reach the steady state. As time goes by in the simulation, the system becomes more and more frustrated because each particle is trapped in a region with a large number of particles on the neighboring sites. As the simulation progresses, we observe that the system converges to a pattern of scattered spots containing a large number of particles, similar to Fig. 3.4 at $t = 199$. However, the true infinite limit behavior of the model is unknown. Since the clusters formed have a finite number of particles in a finite system, the probability of a particle leaving a cluster and joining another cluster with a larger number of particles (therefore more significant interaction strength) is non-zero. Hence, in the limit as time (t) goes to infinity particles will converge and form a single dense cluster.

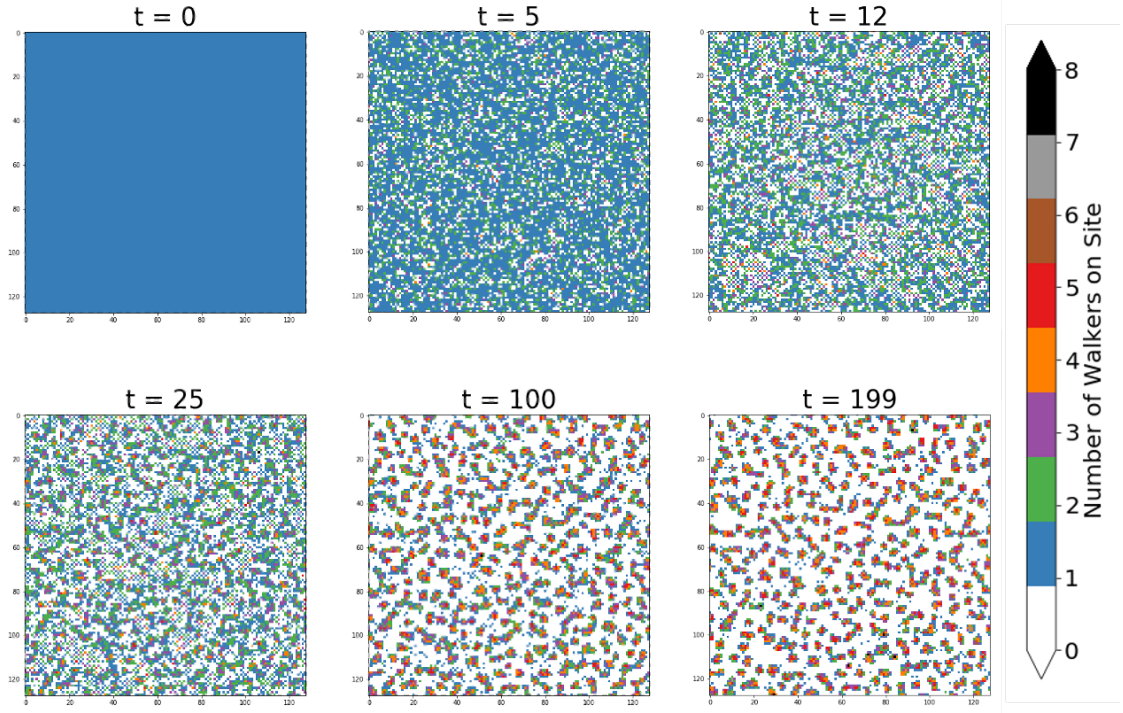


Figure 3.4: Time evolution of particles on a square lattice of size 128. At $t = 0$, all lattice sites are occupied by a single particle. Colors denote number of walkers on each lattice site.

In this chapter, we study the connectivity properties of this multi-particle system. For this reason, we use a repertoire of tools from computational studies of percolation theory, namely finite size scaling which was introduced in chapter two. The first step is to transform each observation in this lattice system to a binary format similar to site percolation. For this purpose, we choose a threshold (in terms of the number of particles) to declare a site on/off. Note that any threshold can be chosen, and the threshold choice has a significant impact on the connectivity patterns observed. In this work, we choose the site activation threshold as a single particle, meaning that a site with one or more particles is declared active/on, and a site with no particles is declared inactive/off. Fig. 3.5 shows the result when we ignore particle density and

transform the lattice to regular binary form in percolation problems. In this figure, it is more observable that the long-time dynamics of the system result in a pattern of scattered spots. Note that, in continuous systems with continuous density field [4], the density threshold to declare a site active/inactive can itself play a role as a control parameter for studying the phase transition of connectivity.

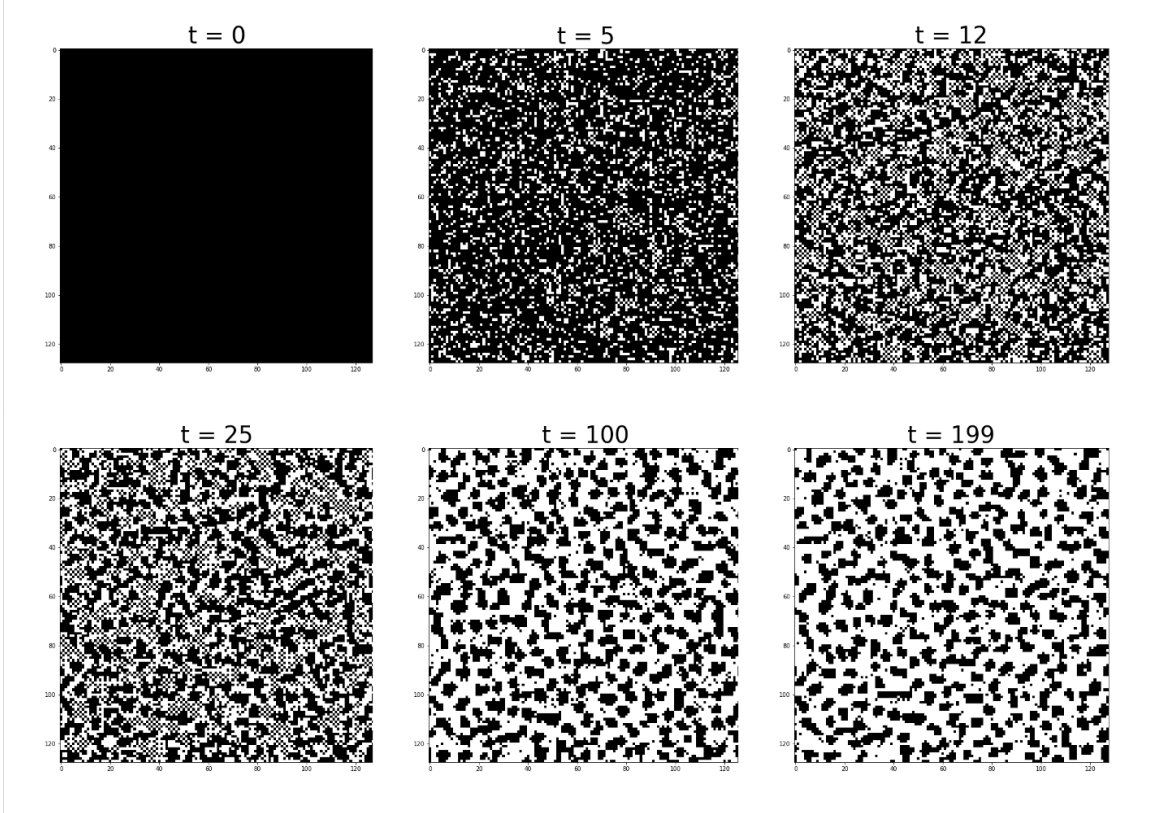


Figure 3.5: Time evolution of lattice occupancy. Each site is declared active (black) if there is one or more particles on it. Otherwise, it is declared inactive (white).

After reformulating the problem as binary percolation, we can now study the dynamics and behavior of connected components formed by the interacting particles. In regular percolation, with the random addition of sites to the lattice, percolation theory predicts that there is a threshold in which the system suddenly gains global connectivity. As discussed in the literature review, many previous studies have observed phase transitions in reaction diffusion systems [4, 145, 147, 155]. However,

considering the size of connected components as the order parameter of the phase transition is not well-studied among these works. Fig. 3.6 shows the evolution of the connected components of the lattice as the dynamics of the particles unfold. Colors in the figure denote the size of the largest connected component (LCC) divided by the total number of lattice sites. As the dynamics unfold and the walkers hop to neighboring sites, the initial encompassing LCC shrinks in size. At $t = 14$, we can see that the lighter blue connected component is the largest component, and that it has clearly lost global spanning connectivity across the lattice.

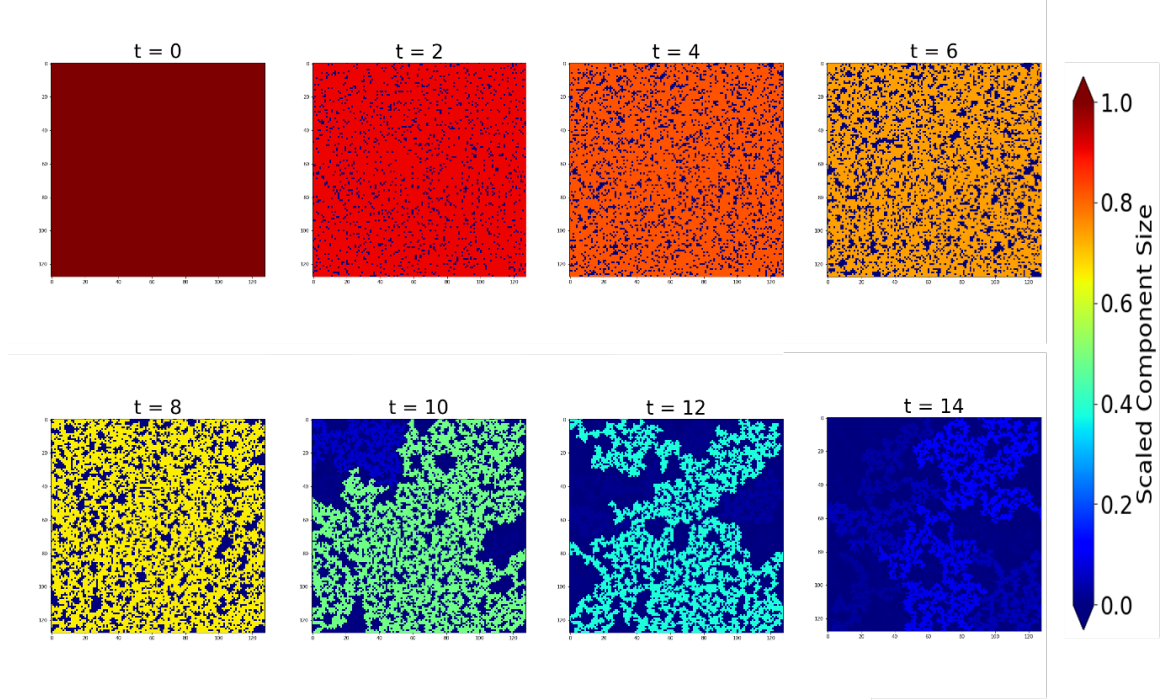


Figure 3.6: Evolution of connected component size. Colors denote component size divided by the size of the lattice.

3.3.1 Time-evolution of Connected Components

Non-interacting Particles

The percolation properties of the stationary state of M non-interacting walkers on a square lattice can be derived analytically. Given M walkers on a square grid

with N sites, the probability of a single walker being on a specific site is given by $1/N$. Then the probability that a site has no walker, P_0 , is given by:

$$P_0 = (1 - \frac{1}{N})^M \quad (3.3)$$

In site percolation [156], global connectivity of a network is characterized by parameter p denoting the site occupation probability. If p exceeds a certain value p_c , a phase transition in the global connectivity of the network is observed. For site percolation on a square grid [157, 158], $p_c = 0.5927$. We utilize this value to derive the number of walkers needed to have steady-state global connectivity in a system of non-interacting walkers. (3.3) is equivalent to $1 - p$; therefore, if $M = \alpha N$ in the infinite limit we have:

$$\lim_{N \rightarrow \infty} (1 - \frac{1}{N})^M = \lim_{N \rightarrow \infty} (1 - \frac{1}{N})^{\alpha N} = e^{-\alpha} = 1 - p \quad (3.4)$$

Phase transition occurs at $p = p_c = 0.5927$. Plugging p_c in and solving for α We find $\alpha_c = 0.8982$. This implies that if we are above this threshold and initialize the walkers uniformly at random, we will not lose global connectivity as the dynamics of the system unfolds. In this case, the particles quickly converge to their final distribution, and similarly, the size of the largest connected component in the lattice evolves to its steady state size. Fig. 3.7 shows the scaled size of GCC as a function of time for both interacting and non-interacting walkers.

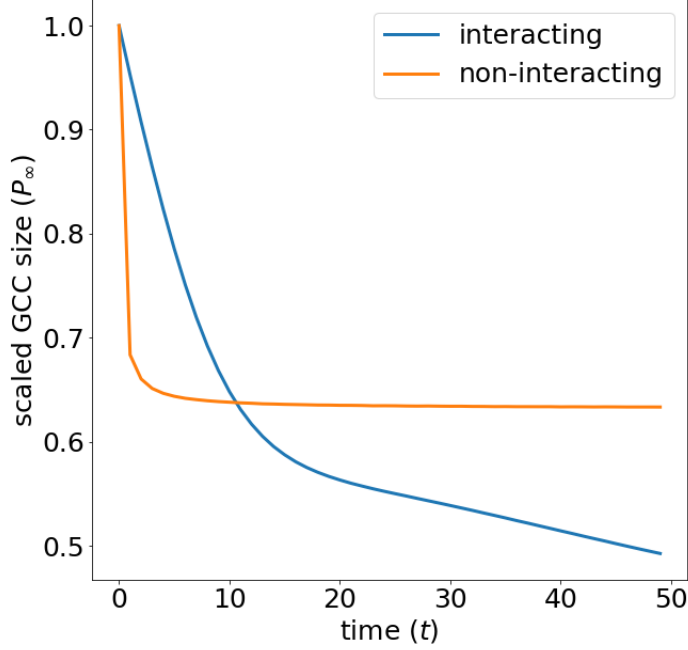


Figure 3.7: Scaled size of GCC as a function time for interacting and non-interacting particles. The plots are averaged over 2000 simulations for a lattice with $L = 128$.

Following [159], we define percolation when a connected component spans the lattice in both directions. Using this definition, we ensure that there exists at most one percolating cluster in each simulation snapshot. Similarly, we define percolation probability ($\Pi(t)$) at time-step t , as to be the fraction of times we have a percolating cluster among the total number of runs. Fig. 3.8 shows the time evolution of percolation probability as defined above. The interacting system sharply loses its percolating cluster. However, as we expected, the non-interacting system remains above the percolation threshold.

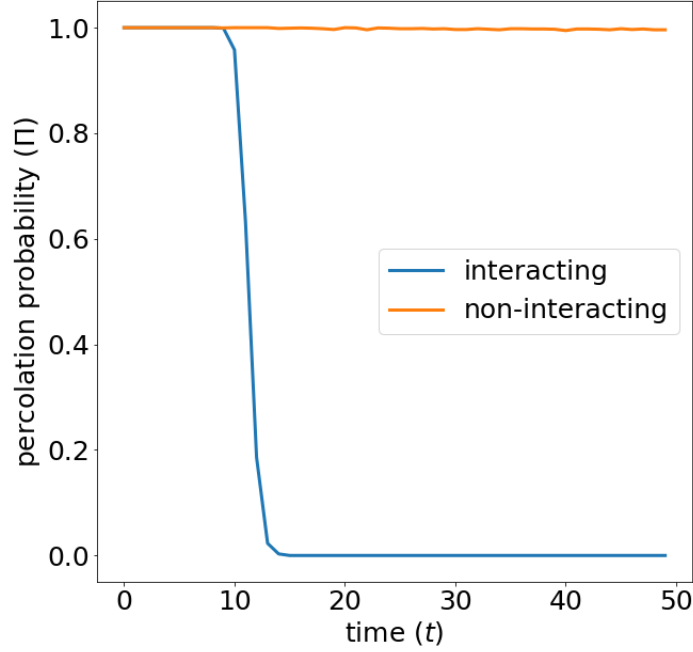


Figure 3.8: Percolation probability as a function time for interacting and non-interacting particles. The plots are averaged over 2000 simulations for a lattice with $L = 128$. The system is considered percolated if there exists a spanning cluster which connects two side of the lattice both horizontally and vertically.

3.3.2 Phase Transition of Global Connectivity and Finite Size Scaling in time Domain

As shown in the previous section, a sharp transition in global connectivity is observed in the dynamics of our model. In this section, we will study the critical behavior of this transition and understand what class of phase transitions it belongs to. For this reason, aside from percolation probability (Π) and percolation strength (P_∞ , size of LCC normalized by the lattice size, see chapter 1), we also investigate other parameters regularly studied in the study of phase transitions in connectivity. Namely, filling factor p , truncated average cluster size S as well as the second largest cluster size s_{max} . S and p are respectively defined as:

$$S = \frac{\sum_s n_s s^2}{\sum_s n_s s} \quad (3.5)$$

$$p = \sum_s n_s s \quad (3.6)$$

Here, n_s stands for the number of clusters of size s per site. In other words, n_s denotes the number of clusters of size s , divided by the lattice size. Since the percolating cluster diverges above p_c , the sum in (3.5) runs over all cluster sizes except that of the largest cluster. In 3.6, p is called filling factor (total number of occupied sites normalized by the lattice size). In Fig. 3.10, we plot these four parameters as a function of time for different system sizes. Fig. 3.10 (a) and 3.10 (b) show how the phase transition sharpens as we increase the system size, which is a typical feature of continuous phase transitions.

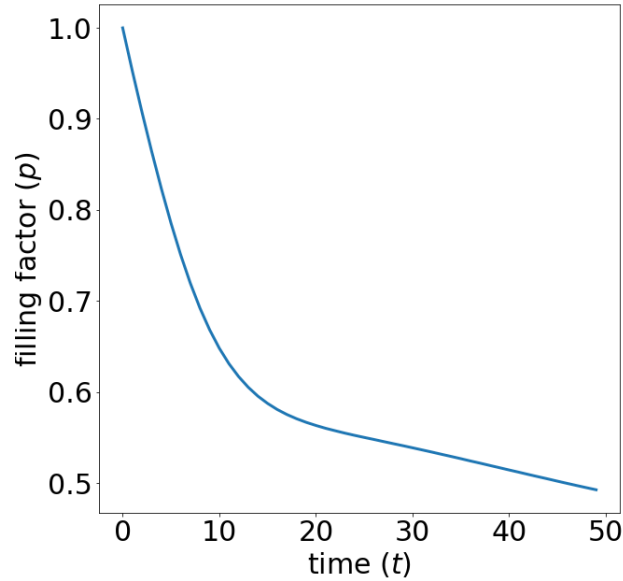


Figure 3.9: Filling factor p as a function of time. Filling factor is a monotonically decreasing function of time.

As mentioned earlier, the dynamics of our interaction model largely depend on the initial conditions and the strength of parameter α . In Fig. 3.10, the phase transition occurs at around $t = 12$. However, changing the parameter α , results in a different critical point as well as different critical behavior.

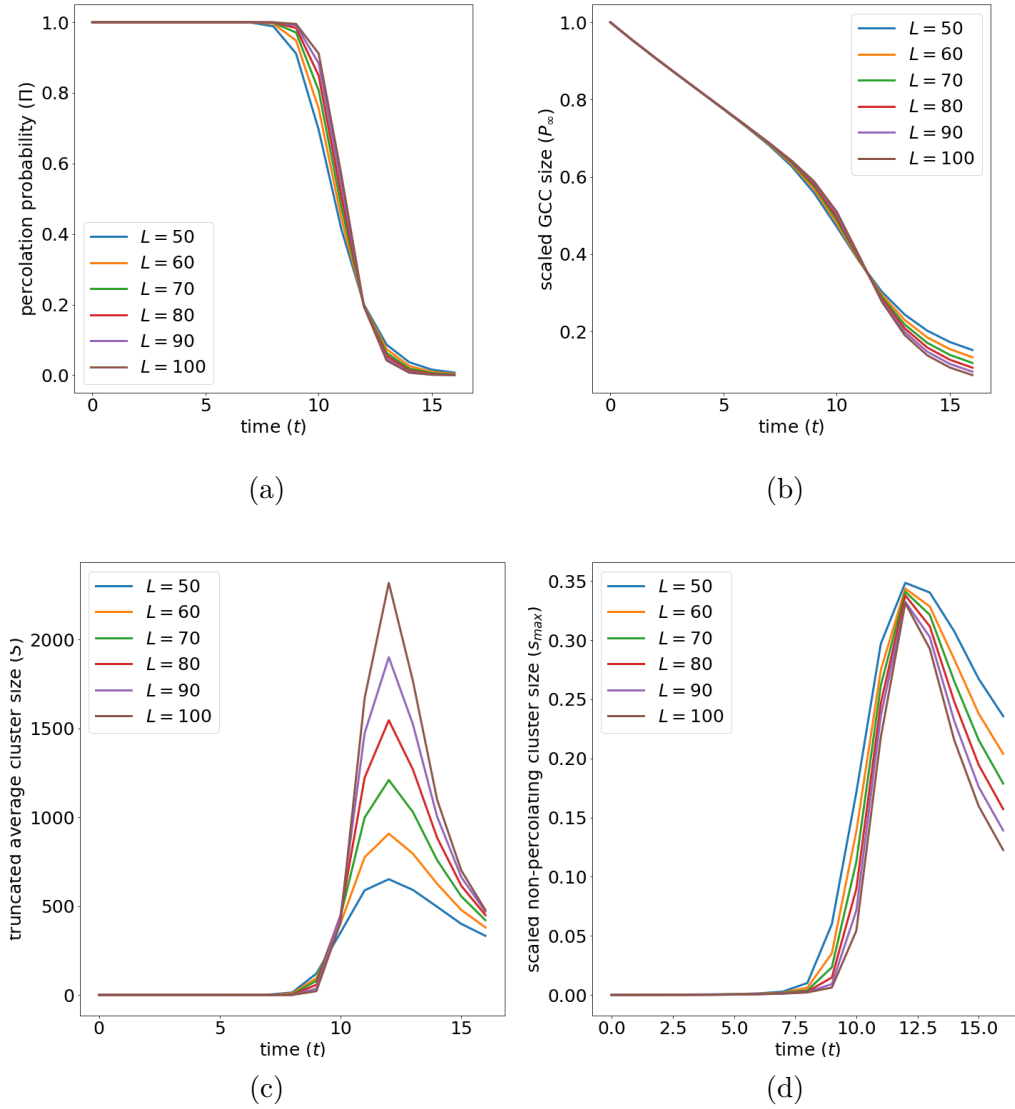


Figure 3.10: Scaled GCC size (a), percolation probability (b), truncated average cluster size (c), and largest non-percolating cluster (d) as a function of time for different lattice sizes. The phase transition in connectivity becomes sharper as the size of lattice increases.

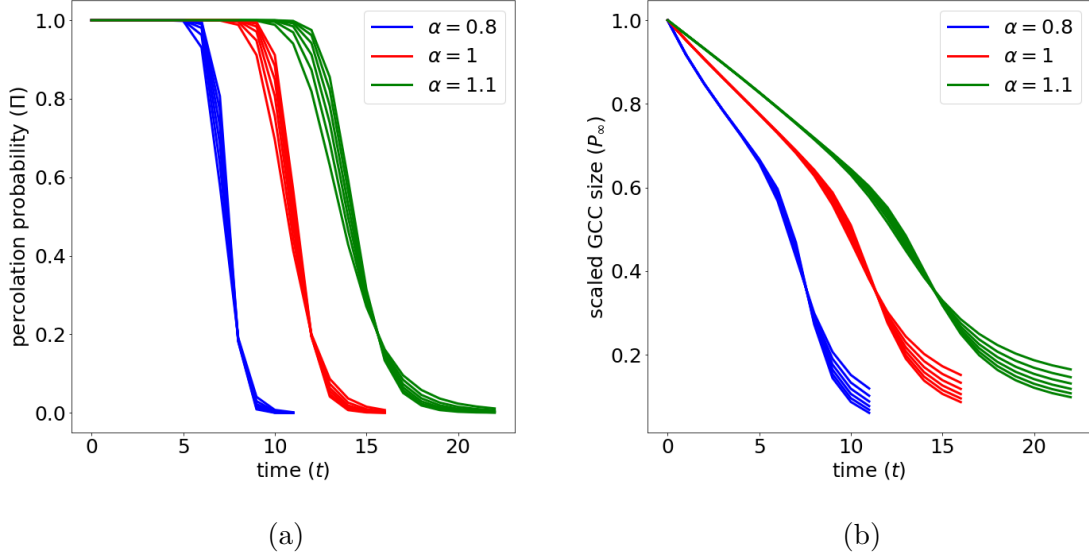


Figure 3.11: Scaled GCC size (a) and percolation probability (b) as a function of time for system sizes and different α s. Here, as in all of the figures, we show curves for $L = 50, L = 60, L = 70, L = 80, L = 90$, and $L = 100$. Colors denote different α values. As we increase α , the transition happens later in time. Also, the near-critical behavior of Π and P_∞ changes as we change the interaction strength by changing α .

Fig. 3.11 shows how that behavior of phase transition varies as we change the interaction strength controlled by the parameter α . The change in critical point is expected since increasing the interaction strength slows the dynamics of the multi-particle system. However, variation in the near-critical behavior of the systems is not trivial. The difference in sharpness of the transition between different system sizes is accentuated as α increases.

In order to further investigate the type of the phase transition and understand its infinite limit behavior, thresholds, and critical exponents, we use the finite-size scaling analysis introduced in section (1.4) of this dissertation, for different α parameters. According to the scaling ansatz discussed in section (1.4), for percolation probability Π , the scaling hypothesis allows us to write:

$$\Pi(t \sim t_c, L) = F_\pi \left[L^{\frac{1}{\nu}}(t_c - t) \right] \quad (3.7)$$

Where F_π is a scaling function. We should note that Π becomes a step function as $L \rightarrow \infty$. In Fig. 3.10 (a), we plot Π for different lengths. The crossing point of all the plots indicates the point of the phase transition. Similarly, plotting Π with respect to $L^{\frac{1}{\nu}}(t_c - t)$ for different lattice sizes and searching for the ν value that gives the best overlap between the plots provides us with a first estimate for ν . Fig. 3.12 shows the collapsed plots for Π as a function of $(t - t_c)$. The plots have nicely collapsed to a master plot, however because of lack of fine-grained data-points (we have discrete time dynamics) near the critical point, we have large error margins for exponent ν . In order to estimate errors, we perform large independent sets of simulations and perform finite-size scaling on them separately. Scaling functions and exponents are the most accurate near the critical point. They become incapable of approximating the finite-size effects for different system sizes as we get away from the critical region. In this case, we have a discrete time phase transition which leaves us with a very small number of data-points above and below the critical point to estimate the critical exponents. We observe an error margin of 0.26 for exponent ν which is a significant margin of error.

3.4 Mapping to p space

In previous sections, we showed that the time-domain behavior of our interacting particle model results in a phase transition in time. As we observed, the parameters of the phase transition changes with change in the interaction strength α . However, finite size scaling theory performs best near the critical point, and in the case of our model, since we have a discrete-time phenomenon, we have a very limited number of data points in the vicinity of the critical point. This makes it difficult to calculate with small error margins. In addition, in order for us to compare our newly discov-

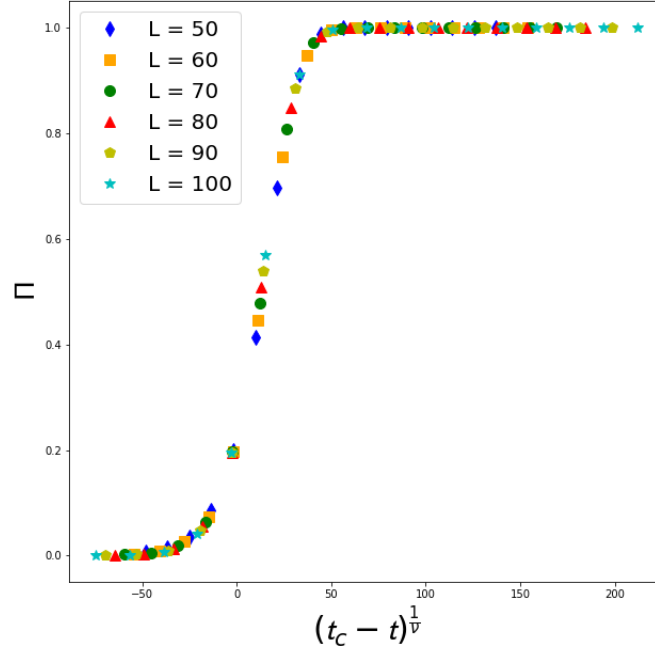


Figure 3.12: Finite size scaling for Π as a function $t - t_c$. $\nu = 1.6 \pm 0.26$ gives us the best curve collapse for different length scales.

ered phase transition with the current percolation-related universality classes in the literature, we need to approach the problem in a similar way that we would approach an ordinary percolation problem where the control parameter is the percolation probability. For this reason, we map the phase transition observed in our model to the p (filling factor) space and, in the rest of this chapter, we investigate the critical behavior of our model's phase transition in p space. If we assume no interaction between the particles, the problem reduces to regular site percolation. Therefore, for a system of non-interacting particles, the phase transition occurs at $p = 0.5927$. However, as observed earlier in this chapter, the dynamics of the particles result in filamentation patterns as the system goes through the phase transition. For this reason, we expect to see different behavior in terms of the critical point and critical behavior. First, let

us see how p varies as a function of time. Fig. 3.9 shows the time-evolution of p . Filling factor is a monotonically decreasing function of time which means that there is a one-to-one mapping between time-steps and values of p . This allows to safely perform our conversion from the time-domain to the filling factor domain, making sure that we are not averaging over statistics from pre-critical and post-critical configurations.

In order to map our simulation results to this new paradigm, at each instance of the simulation, we record all parameters of the phase transition along with the value of filling factor. When saving these values, we round each filling factor value to the third decimal place and store it as a key to a dictionary. The values of the dictionary for this specific key correspond to all the other parameters of the simulation (Π , P_∞ , S , and s_{max}) observed at that specific rounded filling factor. We execute 5×10^6 runs for each lattice size and average all results for all values of p at the end. After running this large number of simulations, at each filling factor value p , we have the ensemble average of all our desired parameters observed in our simulations. (The choice of rounding p to the third decimal place was made to keep computation and number of samples needed manageable).

Fig. 3.13 shows the result of transforming our simulation results into p space. It is evident from the figure that there is a clear phase transition in terms of the filling factor. However, it is also clearly visible that the threshold for the transition is different from the regular site percolation threshold, which is $p = 0.5927$. This is expected since the dynamics of the multi-particle system force the particles to form more spatially structured patterns. The shape of these structured patterns dictates how connectivity in the lattice corresponds to the number of occupied sites. As observed in our simulations, there are multiple stages of pattern formation as the dynamics unfold. First, the filamentous patterns emerge, which then continuously transform into patterns of isolated spots that are effectively static. Fig. 3.14 provides a better view of the limiting behavior of dynamics of the connected components

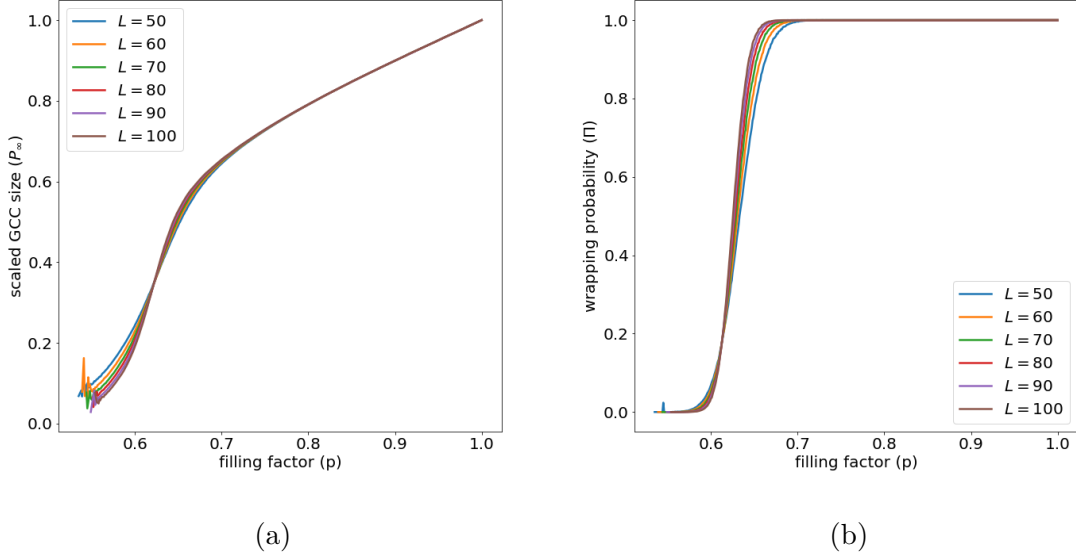


Figure 3.13: P_∞ and Π as function of filling factor.

in our model. Early in the simulation, we have a large number of free particles, belonging to connected components of size 1 (3.14 (c)). As the simulation evolves and we lose global connectivity, filamentation patterns start to separate into multiple smaller clusters. In the limit of large simulation time, we observe the formation of very small clusters, resembling spot patterns, which are effectively do not change size. The particles inside these clusters move internally but the chance of them leaving the cluster is very slim because of the large number of neighbors residing in the cluster.

3.5 Critical exponents and violation of universality

Following the methodology defined in Chapter 2, we use finite size scaling to find the critical exponents for the phase transition observed in the previous section. The following equations characterize the behavior of our parameters near criticality [4].

$$\Pi = F^{(0)} \left[(p - p_c) L^{\frac{1}{\nu}} \right], \quad (3.8)$$

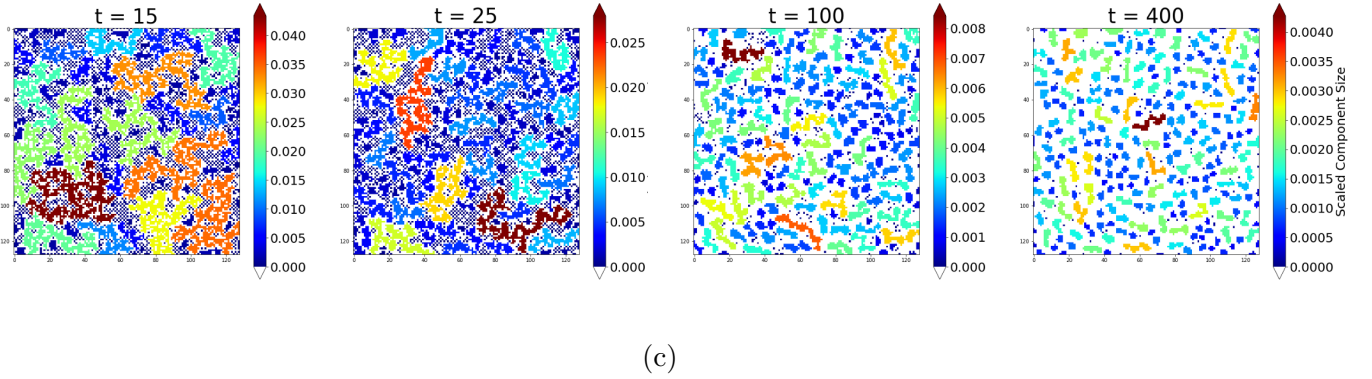
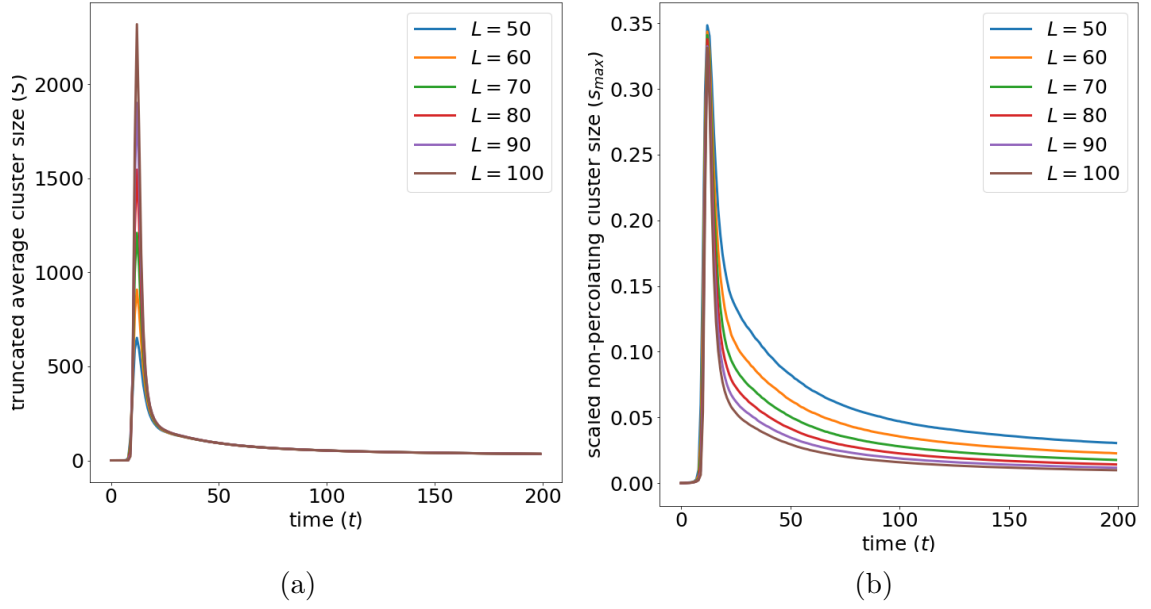


Figure 3.14: (a) and (b) show long-time behavior of S and s_{max} . (c) shows the long-time behavior of connected components. In early stages ($t = 15$ and $t = 25$), there are many small connected components. As time elapses, these small components (mainly free particles) coagulate and form components with higher density. These aggregated particles form the pattern of spots observable at $t = 400$.

$$P_{\infty} = L^{-\frac{\beta}{\nu}} F^{(1)} \left[(p - p_c) L^{\frac{1}{\nu}} \right], \quad (3.9)$$

$$S = L^{\frac{\gamma}{\nu}} F^{(2)} \left[(p - p_c) L^{\frac{1}{\nu}} \right], \quad (3.10)$$

$$s_{max} = L^{\frac{1}{\sigma\nu}} F^{(3)} \left[(p - p_c) L^{\frac{1}{\nu}} \right]. \quad (3.11)$$

Functions F^0 , F^1 , F^2 , F^3 are generic scaling functions that explain the near critical behavior of these parameters in the vicinity of the phase transition. Note that, in the following plots, we are showing the scaling results for $\alpha = 1$, and uniform initial conditions, which we have been working with since the beginning of chapter. Later in this chapter, we will also discuss the effect of varying the initial conditions or the parameter α (which denotes the strength of interactions) on these exponents. First we use the percolation probability Π to find the critical point of the transition in p space since the point of the transition as a function of Π does not depend on system size. Therefore, the point at which all the plots meet determines the critical point. Fig. 3.15 (a) shows the meeting point of these plots at $p_c = 0.616$. Therefore $p_c = 0.616$ is the critical point of this transition. This threshold is much higher than threshold for regular percolation at $p_c = 0.5927$. This result significantly differs from the critical point found in Etoumi et al.'s work [4], in which they find that the critical point occurs at $p = 0.48$, much lower than the regular site percolation threshold. This intuitively means that the filamentation patterns we observe, cause a decrease correlation length as a function of site occupation probability or equivalently filling factor. Utilizing the critical point found above, we can search for parameter ν , which makes all the curves to collapse to the same master curve when plotted against the rescaled filling factor. Fig. 3.15 (b) shows the perfect collapse of the curves in Fig. 3.15 (a) using $\nu = 1.3 \pm 0.01$. The first important observation is that the value of exponent ν differs from the regular percolation critical exponent $\nu = 4/3$, which means it belongs to a different universality class.

Similarly, we can use the curve collapse method for percolation strength P_{∞} , and s_{max} to find values of parameters β and σ from (3.9) and (3.11). Given that we know

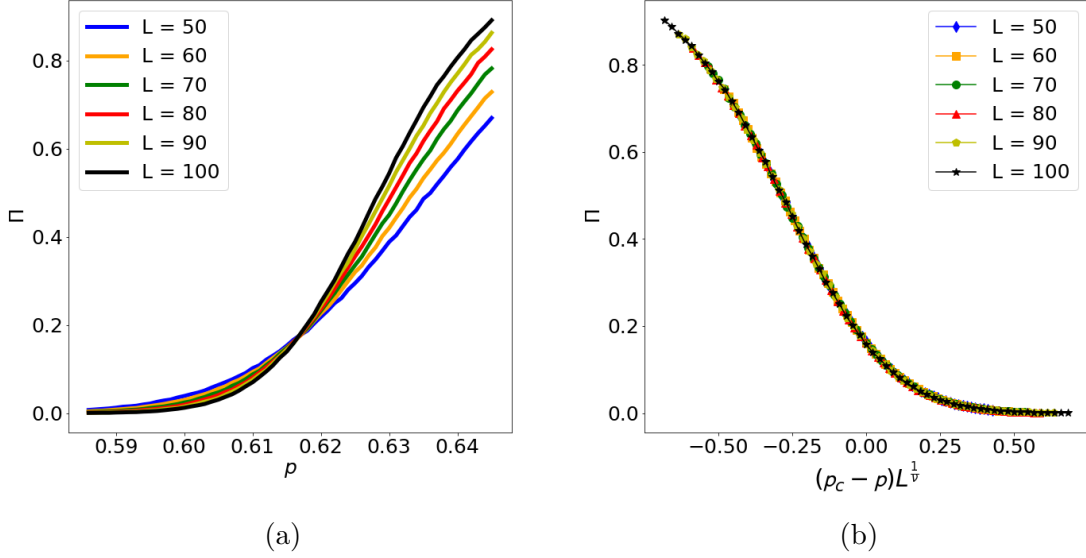


Figure 3.15: (a) Percolation probability Π with respect to the filling factor p . The expected unique crossing point defines $p_c = 0.616 \pm 0.001$. All the curves result from the average of 5×10^6 independent runs. (b) Percolation probability Π as a function of the re-scaled variable $(p_c - p)L^{\frac{1}{\nu}}$, yielding $\nu = 1.30$ by curve collapse.

the value of p_c , we search for the parameters β and ν that minimize the distance between plots of $P_\infty L^{\frac{\beta}{\nu}}$ vs $(p_c - p)L^{\frac{1}{\nu}}$. In Fig. 3.16, we find the same value for p_c when $\beta\nu = 0.11$. This value is similar to the percolation universality class on a 2-dimensional lattice, which signals that we are in the weak universality paradigm introduced in [122]. As mentioned earlier in the introduction Chapter, the notion of universality predicts that the values of β , ν , and $\beta\nu$ in the site/bond percolation on all regular 2-dimensional lattices are the same. The value $\beta/\nu \approx 0.11$ for ordinary percolation and for our model, however, values of β and ν are different between the two.

Last, exponent σ characterizes the mass divergence of the largest non-percolating component when approaching criticality. Fig. 3.17 shows how curve collapse determines $\sigma = 0.34$.

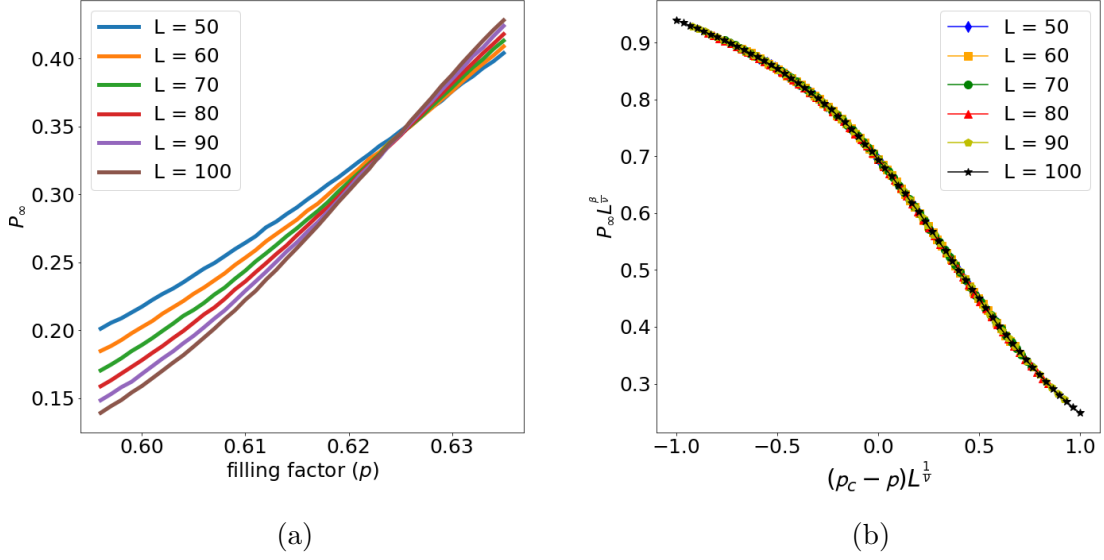


Figure 3.16: (a) Percolation strength Π_∞ dependence on the filling factor p .(b) Rescaled cluster strength P_∞ as a function of the rescaled parameter $(p_c - p)L^{1/\nu}$. The ratio $\beta/\nu = 0.11 \pm 0.01$ yields the same value of p_c found using Π .

3.5.1 Weak Universality

The concept of universality has been verified theoretically and experimentally in many different systems. However, since the early 20th century, there have been observations of violation of universality [139, 140, 145, 147, 160, 161]. In these systems, a continuous change in critical exponents is observed as one changes a certain control parameter in the underlying model. Suzuki [122] proposed weak universality, in which critical exponents like β , ν , and γ vary continuously, however, their ratios β/ν and γ/ν remain constant.

3.5.1.1 Continuous variation of exponents as a function of α

Earlier in this chapter we observed that the time-evolution of particles, pattern formation and the threshold of the studied phase transition, all depend on the strength of the inter-particle interaction, controlled by parameter α , and the initial conditions.

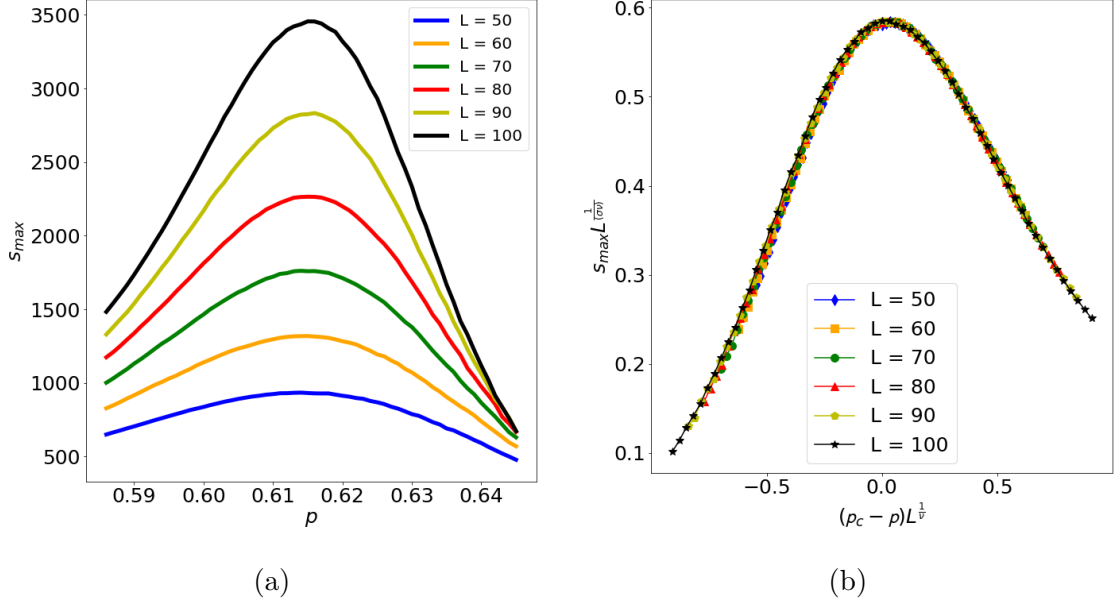


Figure 3.17: Rescaled largest non-percolating cluster as a function of rescaled parameter $(p_c - p)L^{\frac{1}{\nu}}$. Seeking a curve collapse leads to the determination of $\sigma = ? \pm$.

In this section, we study the effect of varying α on the critical exponents of the transition. We also compare the critical exponents with known universality classes, especially, the percolation and directed percolation universality class. Fig. 3.19 shows the plot of Π vs p for various system sizes ($L = 50, \dots, L = 100$) and two different interaction strengths, namely $\alpha = 0.6$ and $\alpha = 1.1$. Note that increasing α makes the particles less prone to change configuration and delays the onset of the phase transition in time, therefore, we are computationally bound to explore certain values of α . Observing Fig. 3.19, it is evident that the near-critical behavior of these systems are different.

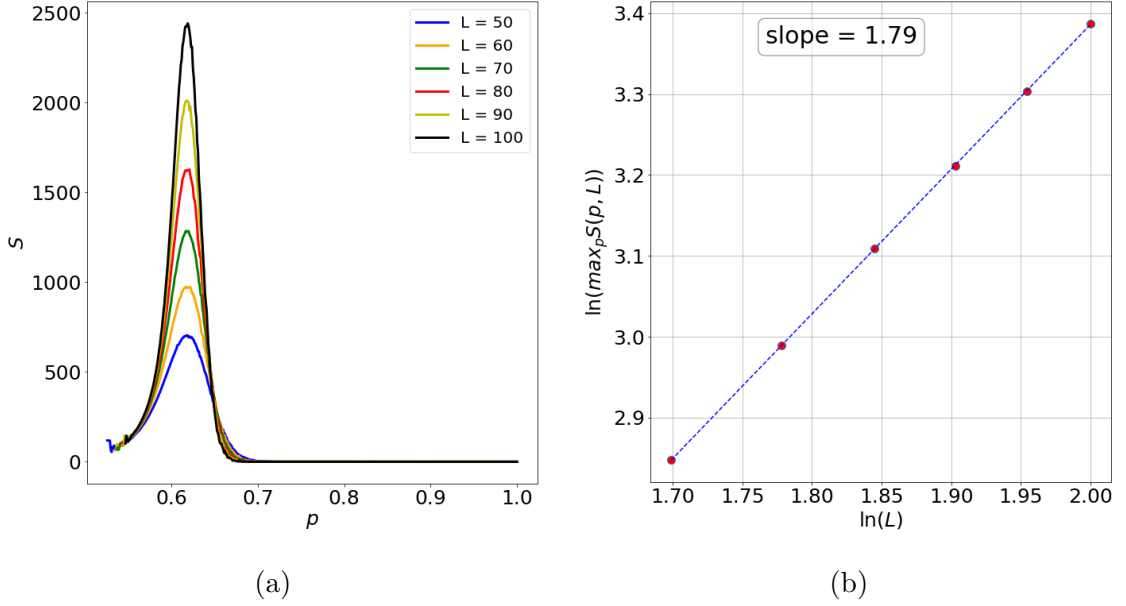


Figure 3.18: (a) Average cluster size S with respect to p . The percolating cluster has been excluded in calculating the average cluster size. (b) $\ln(S)$ with respect to the $\ln L$, allowing us to find $\frac{\gamma}{\nu} = 1.79 \pm 0.05$

Table 3.1: Critical exponents as a function of α

	p_c	ν	β	σ	β/ν	γ/ν
$\alpha = 0.6$	0.620 ± 0.001	1.49 ± 0.01	0.16 ± 0.01	0.35 ± 0.02	0.11 ± 0.01	1.78 ± 0.01
$\alpha = 0.8$	0.619 ± 0.001	1.45 ± 0.01	0.15 ± 0.01	0.35 ± 0.02	0.11 ± 0.01	1.78 ± 0.01
$\alpha = 1$	0.616 ± 0.001	1.30 ± 0.01	0.14 ± 0.01	0.34 ± 0.01	0.11 ± 0.01	1.79 ± 0.01
$\alpha = 1.1$	0.612 ± 0.001	1.28 ± 0.01	0.14 ± 0.01	0.36 ± 0.02	0.11 ± 0.01	1.78 ± 0.01
$\alpha = 1.5$	0.533 ± 0.001	1.21 ± 0.01	0.13 ± 0.01	0.39 ± 0.02	0.11 ± 0.01	1.78 ± 0.01
regular percolation	0.5927	1.33	0.14	0.43	0.11	1.79

In Table 3.1 we show the result of applying finite-size scaling and extracting the critical exponents for different values of α . Exponents ν and β change continuously as interaction strength changes. However, their ratios β/ν and γ/ν remain constant. This is in line with Suzuki's weak universality introduced in [122]. The ratios β/ν and γ/ν are also known to satisfy the following universal scaling relation in lattice systems:

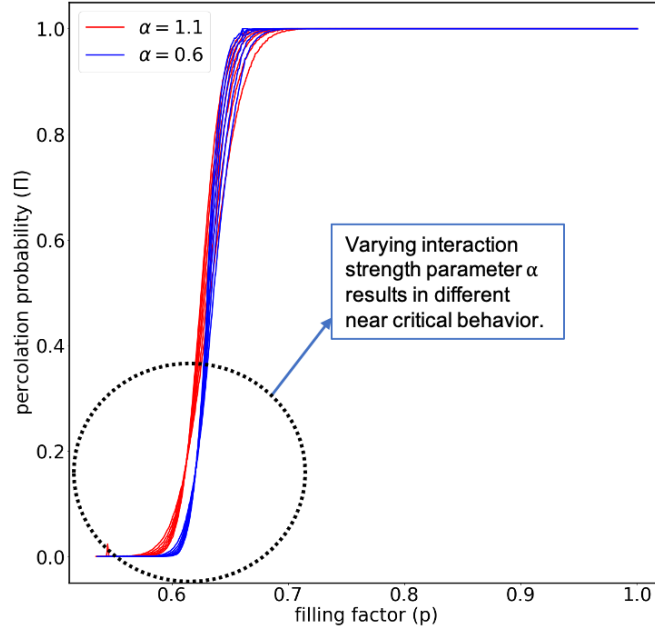


Figure 3.19: Percolation probability Π as a function of filling factor p for $\alpha = 1.1$ and $\alpha = 0.6$ with the same uniform initial conditions.

$$\frac{\beta}{\nu} + \frac{\gamma}{\nu} = d \quad (3.12)$$

where d is the dimension of the lattice which in our case is 2. Substituting values $\beta/\nu = 0.11$ and $\gamma/\nu = 1.78$ in the above equation yields 2 with a small margin of error which again confirms the reliability of our results.

For all values of α except $\alpha = 1.5$, the value of p_c is higher than the regular percolation threshold which means that the occupied lattice sites are correlated in a way that they decrease global connectivity in the lattice compared to random placement of occupied sites in ordinary percolation. However, as we increase α to 1.5, p_c suddenly has a sharp decrease to 0.533, which is a fascinating observation. This means that changing the interaction strength (α) changes the structure of connected components

in a way that their long-range correlation is accentuated in lower p values. We conjecture that the factor that contributes to p_c , is the interplay between the strength of inter-particle interaction and the diffusion of free particles. As α increases, the increased strength of inter-particle interactions slows the dynamics of particles with a large number of particles in their neighborhood. On the other hand, particles with a small number of or no particles in their neighborhood, diffuse freely and attach themselves to existing formed filaments. This effect enhances the filamentation effect in the system and therefore increases the correlation length of the system. When α is small, since the dynamics of the particles with neighbors are faster, filamentation patterns form more quickly, and many free particles remain un-attached to giant components in the lattice system (see Fig. 3.14 (c) at $t = 15$). Since these free particles or small clusters all contribute to the filling factor (p) of the system, global connectivity is occurs at higher values of p .

Fig. 3.20 shows the component size distribution of our model for two different values of α at $p = p_c$ along with that for ordinary site percolation at $p = 0.5927$. This empirical plot confirms our hypothesis about the effect of the interplay between diffusion and interaction strength on the value of p_c . There is a large variation between the number of components of size one between the three distributions. The model with $\alpha = 1$ has almost an order of magnitude more single-particle components compared to the model with $\alpha = 1.5$. Note that for $\alpha = 1$, the transition happens at $t_c = 12$, however, for $\alpha = 1.5$, the transition happens at $t_c = 110$. This longer time-frame allows these free particles to diffuse and attach themselves to other components, changing the overall shape of the component size distribution. This explanation is valid for other small components. On the other hand, a comparison of both distributions generated from our model with that for ordinary site percolation points out many qualitative differences between the distributions. We observe a significantly larger number of free particles in the low- α regime for our model. On the other hand,

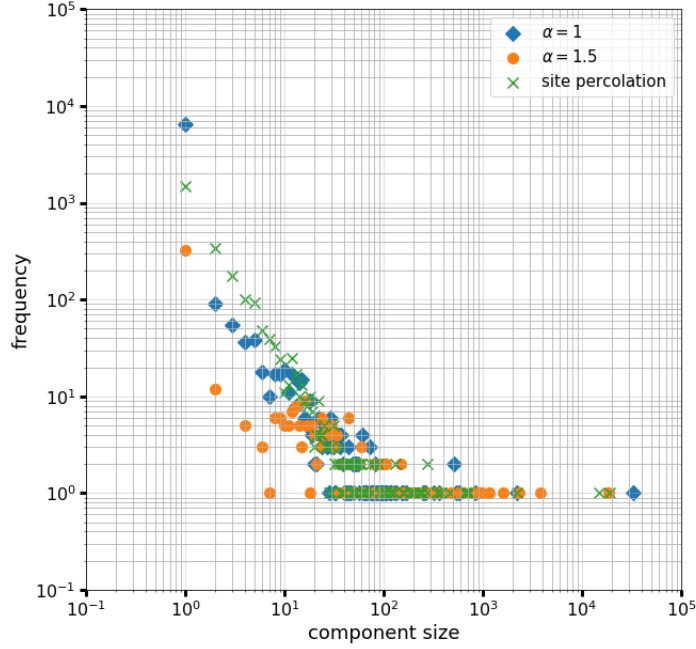


Figure 3.20: Cluster size distribution at $p = p_c$ for systems simulated with two different α parameters. along with regular site percolation on square lattice at $p = 0.5927$. System size is $L = 300$.

small components which occupy more than one site are more abundant in regular site percolation (green crosses). It is again worth noting that here we are fixing the initial conditions and varying the interaction strength. Changing the initial conditions will change the initial distribution of the component site in the lattice and hence, change the component size distribution at the point of transition.

3.5.1.2 Effect of Initial Conditions on the Critical Exponents

In the previous section we discussed the effect of interaction strength (α) on critical exponents. As mentioned earlier, the initial distribution of particles plays an important role in the dynamics and the critical behavior of the system. In all simulations shown up until now, we have used uniform initial conditions as a natural compari-

son to regular site percolation. In uniform initial conditions we fill each lattice site with a single particle before starting the simulation. In this section, we change this initial condition to random initial distribution of particles on the lattice. At $t = 0$ we disperse N particles over a square lattice of side L uniformly at random. Here we assume $N = L^2$, however we should note that changing the initial particle density is also a tunable parameter which can significantly impact the dynamics [2]. We assume $N = L^2$, which produces an initial condition that is above percolation threshold when randomly dispersed, and is a natural choice from the perspective of percolation theory. Investigating higher or lower initial particle densities is outside the scope of this dissertation. Similar to the previous section, we map the time-evolution of our particle system into p space and investigate its critical behavior. Fig. 3.21 shows the percolation probability Π and the scaled GCC size P_∞ as a function of filling factor p for a system with random initial conditions ($\alpha = 1$). While the shape of the near-critical region differs from that of regular site percolation and shows higher levels of non-linearity, the figures show that the transition becomes sharper as system size is increased. Therefore, we are still observing a continuous phase transition. Similar to the previous section, these results are averaged over 5×10^6 independent simulations for each system size.

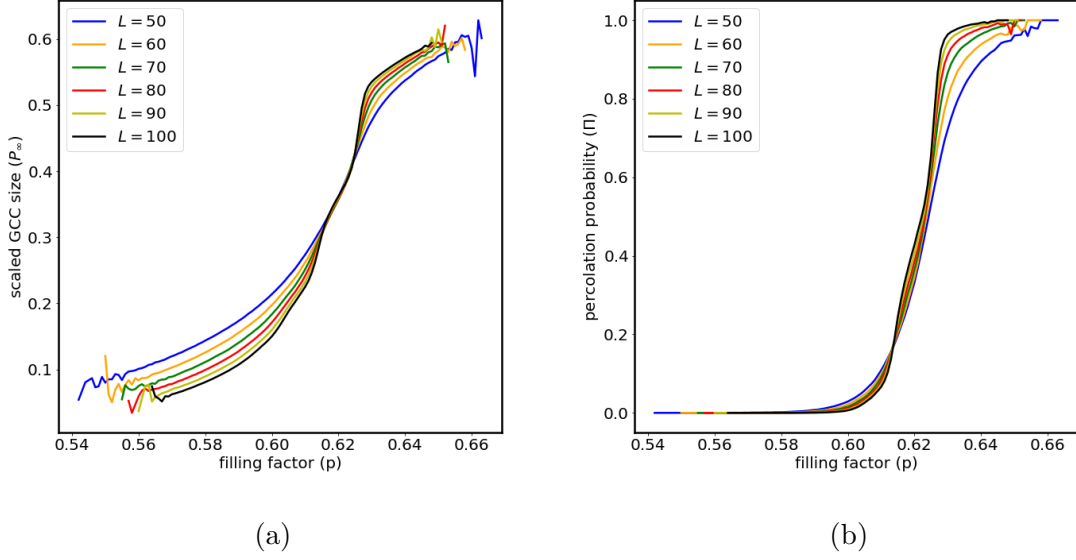


Figure 3.21: P_∞ and Π as function of filling factor for a system with random initial condition and $\alpha = 0$.

In Table 3.2 we study the effect of varying parameter α on critical exponents. It is worth noting that these results are based on random initial conditions as opposed to the results shown in Table 3.1 which were based on uniform initial conditions. Our first observation is that changing the initial conditions has a significant effect on the value of critical exponents. For example, parameter ν is almost half of its value for the same α but with uniform initial conditions. Our second observation is that the exponents vary as a function of interaction strength. Comparing to the error margins based on uniform initial conditions (Table 3.1), error margins are higher for random initial conditions (Table 3.2). This is because, as we observed in Fig. 3.21, the critical region shows higher degrees of non-linearity.

Table 3.2: Critical exponents as a function of α for random initial condition

	p_c	ν	β	σ	β/ν	γ/ν
$\alpha = 0.6$	0.610 ± 0.001	0.61 ± 0.03	0.069 ± 0.004	0.76 ± 0.05	0.11 ± 0.01	1.79 ± 0.01
$\alpha = 0.8$	0.612 ± 0.001	0.67 ± 0.03	0.076 ± 0.005	0.82 ± 0.04	0.11 ± 0.01	1.79 ± 0.01
$\alpha = 1$	0.614 ± 0.001	0.74 ± 0.03	0.083 ± 0.004	0.77 ± 0.05	0.11 ± 0.01	1.79 ± 0.01
$\alpha = 1.2$	0.615 ± 0.001	0.81 ± 0.04	0.089 ± 0.005	0.80 ± 0.05	0.11 ± 0.01	1.79 ± 0.01
$\alpha = 1.4$	0.615 ± 0.001	0.94 ± 0.03	0.099 ± 0.005	0.78 ± 0.04	0.10 ± 0.01	1.79 ± 0.01

3.6 Phase transition in similar systems

3.6.1 Global Connectivity of Photoactive Robotic Swarms

In this section, we investigate the phase transition of connectivity in a similar multi-agent model developed by Mijalkov et al. [5]. This is an initial investigation of whether percolation transitions occur in dynamic multi-agent interacting systems. Their model is inspired by the motion of chemotactic cells, which use their molecular concentration receptors to climb a chemical gradient by adjusting their tumbling rate. In their work [5], they study the collective behavior of interacting autonomous photoactive robots in a continuous plane.

Agents in their model are subject to rotational Brownian motion and are in the presence of an external intensity field. Each agent emits a spatially decaying intensity field. Each agent also measures the total intensity field at its present location and adjusts its propulsion speed as a function of this measured intensity. They further introduce a sensorial delay between sensing time and speed adjustment time, resulting in collective aggregation and segregation patterns in the system.

The system of differential equations governing the dynamics of each agent's motion is depicted in (3.13)

$$\begin{cases} \frac{dx_t}{dt} = v(I_{(t-\delta)}) \cos \varphi_t \\ \frac{dy_t}{dt} = v(I_{(t-\delta)}) \sin \varphi_t \\ \frac{d\varphi_t}{dt} = \sqrt{\frac{2}{\tau}} \eta_t \end{cases} \quad (3.13)$$

$$v(I) = (v_0 - v_\infty) e^{-\frac{I}{I_c}} + v_\infty \quad (3.14)$$

where (x_t, y_t) is the position of the agent in plane at time t , φ_t is its orientation, v is its speed, τ is the reorientation characteristic time (i.e., the time after which the standard deviation of the agent's rotation is 1 rad), δ is the delay in reacting to the change in intensity field, and η_t is a white noise driving the agent's reorientation.

Eq. (3.14) shows the speed of each agent as a function of sensed intensity field. In this equation, $v(0)$ is the maximum speed, $v(\infty)$ is the residual speed at infinite intensity, and $I(c)$ is the characteristic intensity scale. As evident from the differential equations system, having a different function for $v(I)$ results in different aggregation and segregation patterns. For our work, we use the standard decaying function in (3.14).

This model of interacting agents in the continuous plane shares many similarities with our discrete interacting walker model. First and foremost, agents react to the sum of locally received intensity field, a direction-invariant function. In addition, the hopping rate of walkers in our model directly translates to speed in the photoactive robots model, which is a decaying function of intensity, meaning that agents prefer to move towards higher intensity regions and remain there. We showed that our discrete interacting walker model results in a phase transition in the global connectivity in the lattice system. In order to understand if such phase transitions in connectivity also appear in other systems, we investigate their model as another example of single-particle density dependant systems. Examining the critical exponents of this transition is out of the scope of this work, so we limit our investigation to the question of existence of such phase transition in connectivity and postpone any further analysis to the future work.

Fig. 3.22 shows the dynamic behavior of multiple agents in a positive delay regime. As is evident from the figure, agents move from a randomly distributed phase to a phase in which clusters of agents form. The size of these clusters at time-step t depends on the parameters of the system of equations. Tuning the parameters can result in a single cluster moving around collectively.

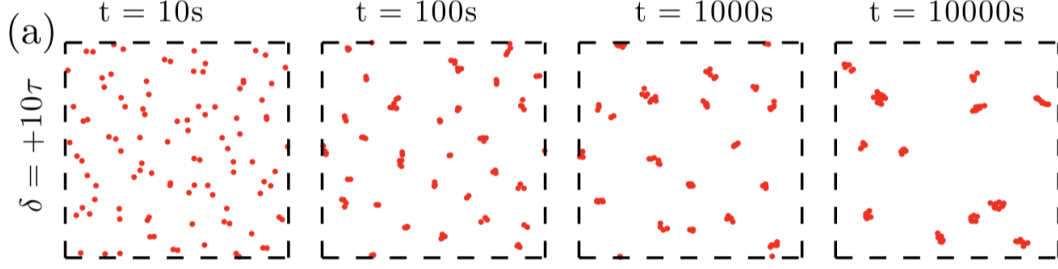


Figure 3.22: Collective aggregation patterns forming in positive delay regime. Image taken from [5]

In order to study the percolation properties of this model in a continuous plane, we run numerous multi-agent simulations on a continuous square region with periodic boundary conditions (agents which exit the plane from one side of the square re-enter from the opposite side). In each simulation, we fix the number of agents to N and randomly distribute all the agents in the beginning of the simulation. We then translate each snapshot of the dynamics to a random geometric graph. Agents that are within the connectivity radius R of one another are considered connected. We consider the system percolated if there is a connected component connecting two sides of the square region. Connectivity radius R is chosen in a way that the system is above the percolation threshold of random geometric graph [162] at the beginning of the simulation. Similar to our discrete multi-particle model, the number of simulations in which the system has percolated at time t is used to calculate the percolation probability of the system at each time-step. Fig. 3.23 shows percolation probability as a function of time for different system sizes. Like our discrete interacting walker

model, we observe the sharpening of transition in global connectivity as we increase the system size, which signals the existence of a phase transition in the time domain. The transition point can similarly be characterized by the crossing point of different system sizes. It is interesting to observe the occurrence of connectivity phase transitions in systems with very different underlying dynamics in continuous and discrete space. It is an exciting research direction to characterize the universality class of this phase transition, but it is out of the scope of the current study.

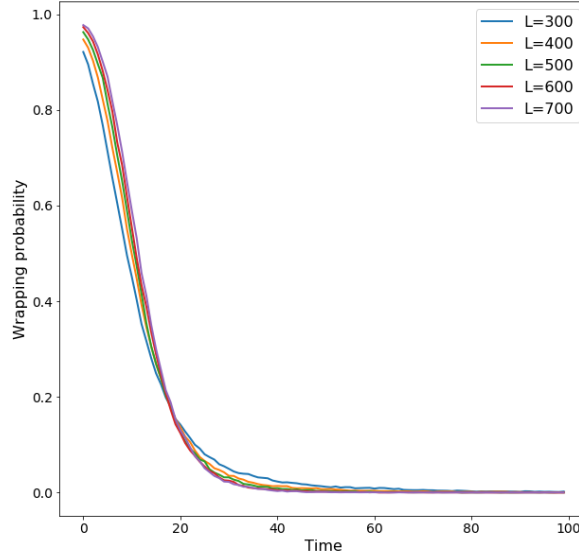


Figure 3.23: Percolation probability as a function of time for photoactive swarm of robots defined by Eq. (3.13).

In the next chapter, after introducing some tools for analyzing reaction-diffusion patterns, we will study the time-evolution of the patterns observed in our model in a more detailed and quantitative manner.

3.7 Conclusion and Future Work

In this chapter, we introduced a simple single-specie interacting particle model on a lattice or a general graph. We studied the phase transition of connectivity during the time-evolution of the system and showed that our proposed model breaks the general paradigm of universality and shows a continuous variation of critical exponents as a function of a control parameter. Contrary to regular universality classes, which are independent of the underlying lattice or initial configurations, the critical exponents in our model also vary as we change the underlying lattice or the initial conditions of the multi-particle system. During the time-evolution, our model goes through different stages of pattern formation. We argued that these patterns' formation affects the cluster size distribution and hence the correlation length in the lattice. Thus, the critical point of our system shifts to values lower/higher than the un-correlated site percolation threshold as we vary the interaction strength. To expand our study of connectivity transitions in density-driven models, we further studied the global connectivity of a system of interacting robots interacting based on an emitted density field. We empirically showed that similar to our model, this continuous system of agents also goes through a phase transition of connectivity as the dynamics of the system evolve. Dynamic percolation transitions in non-equilibrium systems have been rarely studied in the literature, and to the best of our knowledge, we are the first to report continuous variation of exponents in single species systems with local interactions. Future work includes extending this study to other reaction-diffusion and pattern formation systems.

CHAPTER 4

MACHINE LEARNING PATTERNS OF NATURE

4.1 Introduction

Complex patterns emerge in many real-world phenomena. From ecological systems such as brushlands and mussel beds to filamentation of a high-power laser beam passing through a non-linear Kerr media. The study and analysis of these patterns and the underlying non-linear dynamics governing them have been a focus of many fields of science and engineering.

Originally introduced by Turing in 1952 [39], the activator-inhibitor principle provides a potential theoretical explanation for formation of many regular patterns in nature [40, 149, 150]. The underlying principle is based on the diffusive interaction of a local positive activating feedback with a large-scale inhibitory feedback. This activator inhibitor principle can account for many naturally occurring phenomena like growth, birth, mortality, decay, respiration, etc. Similar pattern formation mechanisms such as the Cahn-Hilliard [127] and the Gray-Scott model [12] were later introduced to explain various natural phenomena ranging from spatial ecology to chemical reactions. In this work, we use the Gray-Scott model as a reference model to generate various patterns. The Gray-Scott model generates a large set of different stable and dynamic patterns with small changes in its parameter space. This characteristic makes it an ideal candidate for any study that aims to deduce or predict parameters of a model given an instance of a pattern.

Although numerous studies focused on the mathematical modeling of different pattern formation phenomena, analyzing and quantifying generated patterns from

different phenomena remains scarce. Most of the existing literature on pattern formation and analysis uses a qualitative approach to explain patterns in various systems, and this qualitative analysis is limited by our visual ability to distinguish patterns such as stripes, dots, filaments, etc. Some researchers [1, 45] showed that certain geometric characteristics of patterns can be used to map to a lower-dimensional space and differentiate them. Others used methods from persistent homology, and topological data analysis [43, 163] to classify spatial patterns based on their topological characteristics. Many of these methods are computationally complex and need careful design to be applicable to specific patterns observed in various domains.

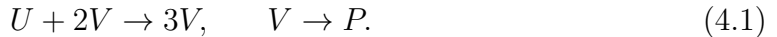
Machine learning methods have seen incredible performance boosts in the past decade due to data availability and the growth of processing power. Specifically, deep learning methods in the field of image recognition and analysis have produced incredible results in terms of accuracy and scalability. In recent years, many researchers in the physics community have started using machine learning algorithms to derive insights from the wealth of real-world and simulation data available to them. Carrasquilla et al. [164] used supervised learning to classify phases of Ising models based on simulated data of the Ising configurations in different temperatures. Wang et al. [165] used unsupervised learning techniques to discover phase transitions in various physical systems. There have been numerous other recent uses of machine learning approaches in physical sciences [166–175]. In this Chapter, we use supervised and unsupervised learning methods to analyze patterns generated by the Gray-Scott model. Specifically, we use unsupervised and supervised classification algorithms to classify patterns generated by the Gray-Scott model. Similarly, we apply supervised regression models to find the underlying differential equation parameters of the Gray-Scott model given a set of images. In order to show the effectiveness of our approach, we generate synthetic patterns from these models and use various machine learning methods for classification and regression. The pre-trained neural network models

can be used in various branches of science to classify or obtain the parameters of experimentally observed patterns. This way, one can use a database of previously observed patterns and see how a specific new observation falls into other categories of patterns. This can further help researchers from various fields of science to categorize and analyze their observed patterns in a more unified manner.

The outline of the Chapter is as follows. In Section we will introduce the pattern generating models that serve as a data generator for training our machine learning algorithms. Sections 4.3 and 4.4 will introduce different machine learning algorithms utilized in our analysis. In Section 4.5, we introduce various classification and regression tasks and analyze the performance of applying various machine learning algorithms applied to these tasks. For the unsupervised learning task, we also implement Mecke’s [1] work on geometrical properties of patterns and use that to compare our results with the existing literature in the field. Section 4.6 concludes and summarizes our findings.

4.2 Gray-Scott Model

The Gray-Scott model is one of the important models for studying pattern formation in reaction-diffusion systems. It models the chemical reaction between two species, U and V [12]. The governing chemical reaction is:



In this reaction, V is converted to an inert product P , which does not interact with the reaction of the system. Species V catalyzes its own creation and therefore appears on both sides of the equation. Gray and Scott developed the following set of partial differential equations to model this chemical reaction.

$$\frac{\partial u}{\partial t} = d_u \nabla^2 u - uv^2 + F(1 - u) \quad (4.2)$$

$$\frac{\partial v}{\partial t} = d_v \nabla^2 v + uv^2 - (F + K)v \quad (4.3)$$

Here u and v represent the local density of chemicals U and V , respectively. We assume that the boundary conditions are periodic and that F and K are constants. The first term in each equation is a diffusion term, similar to the diffusion of heat in the heat equation. d_u and d_v are diffusion coefficients, determining the rate of diffusion for the two chemicals. The term $\pm uv^2$ represent the reaction term, which accounts for conversion of U into V . Increasing v results in a decrease in u . The term $F(1 - u)$ is the replenishment term that reintroduces chemical U to the system. Similarly, the term $(F + K)v$ removes V from the system and serves as the diminishment term.

One naturally occurring example of this system of equations is the development of an embryo. In this case, the bloodstream might serve as the supply of chemicals and the rates by which chemicals permeate through the cell determine parameters F and K for replenishment and diminishment.

The Gray-Scott model, produces a wide range of irregular patterns. Pearson [6], identified 12 different pattern types, all of which correspond to different values of F and K when d_u and d_v are fixed. Figure 4.1 shows the 12 different patterns classified by Pearson using standard methods of nonlinear analysis [176]. The figure shows the chemical concentration of U in the simulated region. Figure 4.1 provides a mapping between the F and K parameter space and the patterns classified by Pearson. Many of the patterns generated by Gray-Scott equations are dynamic patterns showing patterns of turbulence and many others have a more static character resembling natural patterns like corals or the growth of bacterial colonies.

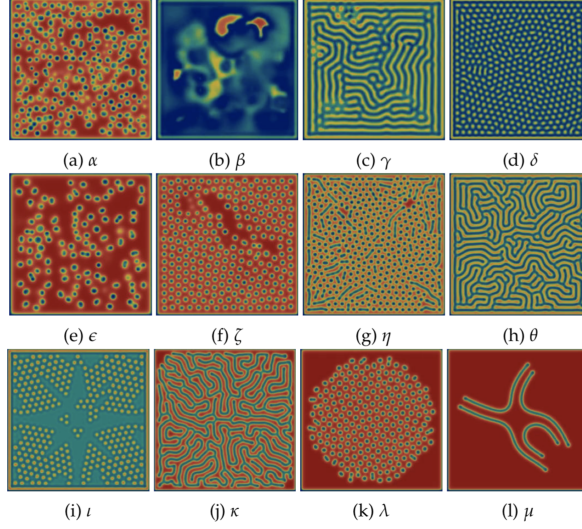


Figure 4.1: Set of 12 distinct Gray-Scott patterns taken from ref. [6]. Colors represent concentration of chemical U where red represents $U = 1$ and blue represents $U = 0.2$. Yellow is intermediate to red and blue.

4.3 Supervised Learning Methods

Convolutional Neural Networks

In recent years, deep learning has found many useful applications in various fields of science. Convolutional neural networks (CNNs) [177] are a class of deep learning methods primarily used for image classification, recognition and analysis. CNNs are regularized versions of multi-layer perceptrons, which were inspired by the structure of the visual cortex, the part of the brain which processes visual sensory inputs. The use of convolution filters significantly reduces the parameter space of the data and hence increases the learning performance. Fig 4.2 shows a schematic representation of a CNN. In this example, the input of the CNN is a 2-dimensional image. The training procedure consists of iteratively changing the weights of the network based on known values in the output layer of the network. The input data to the network can be represented by matrix $X_{N \times (L \times L)}$, which consists of N training images of size $L \times L$.

The first layer applies a number of different convolution filters to the image. In the training stage, these filters are trained to capture the distinctive features of the data. The convolution layer is followed by a non-linear function and the output is passed to a sub-sampling layer. The sub-sampling layer further reduces the parameter space and increases the feasibility of learning. In modern CNNs, many successive convolution-subsampling layers are applied to the data in order to capture features at different length scales. The output of the convolution and sub-sampling operations are connected to a fully connected neural network layer and the fully connected layer is connected to the output layer. The number of neurons in the final layer is determined by the task. For example, for a multi class classification task with M classes, the final layer has M neurons and for a regression task with scalar output, the final layer has a single neuron that is used to predict a scalar value. The model is trained by minimizing a predefined loss function that captures the difference between the prediction and the known output. For our regression tasks we use Root Mean Squared Error (RMSE) loss and for classification problems we use Cross-entropy loss,

$$\text{RMSE Loss} = \sqrt{\frac{1}{N} \sum_{i=1}^N \left(y_i^{\text{predicted}} - y_i \right)^2}, \quad (4.4)$$

$$\text{Cross-entropy Loss} = \sum_{i=1}^N \left(\sum_{c=1}^M y_{i,c} \log(p_{i,c}) \right). \quad (4.5)$$

In (4.4), $y_i^{\text{predicted}}$ is the scalar value predicted by the neural network and y_i is the true value of the output. In (4.5), the first sum runs over the different data-points and the second sum runs over the different classes. Here $p_{i,c}$ is the probability predicted by the model that data-point i belongs to class c and $y_{i,c}$ is a binary indicator if class label c is the correct classification for data-point i .

For a given task, at each iteration, the loss is backpropagated in the network and the weights of the neural network along with the CNN filter are re-tuned. The learned

convolutional filters at different layers of the network are known to capture the patterns present in the image data at different scales.

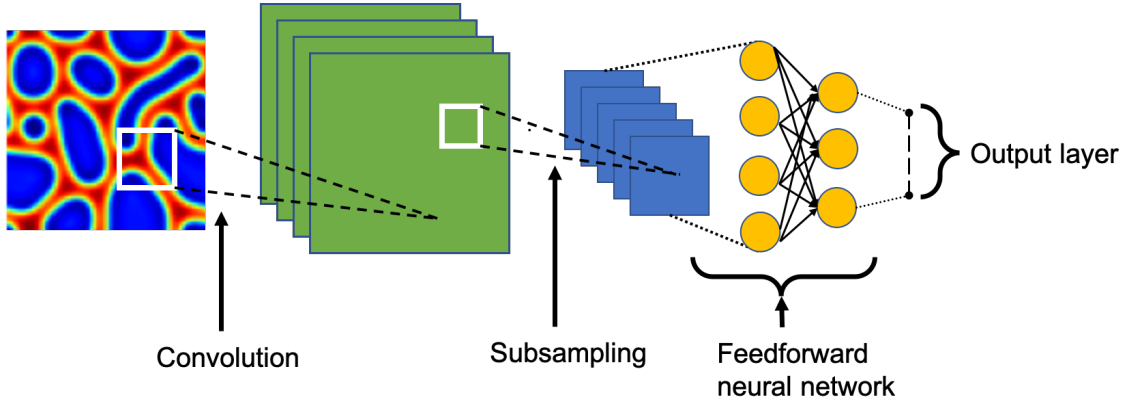


Figure 4.2: Schematic overview of a CNN architecture used in this work. An image is passed through the network. Network weights are iteratively updated by back-propagating the error from the output layer.

4.4 Unsupervised Learning Methods

In this Chapter, the goal of our unsupervised analysis is to cluster a given dataset into groups of similar points without any prior known labels. Clustering techniques usually use distance metrics to group data-points together. However, most often, the data resides in an extremely high-dimensional space. This is particularly true with image data. High dimensionality, makes the use of distance metrics noisy and computationally infeasible. Therefore, unsupervised segmentation is usually performed in two successive steps, namely Dimensionality Reduction, and Clustering. In this section, we briefly describe the dimensionality reduction and clustering techniques utilized in our analysis.

4.4.1 Dimensionality Reduction

Principal Component Analysis

Principal Component Analysis (PCA) [178] is a linear dimensionality reduction technique that projects the data into a lower dimensional space. PCA is typically used for image compression and dimensionality reduction for high-dimensional data. The principal components of the data are a set of mutually orthogonal vectors. The first principal component points in the direction of the space for which the data has the highest variance. The next principal components are the subsequent mutually orthogonal vectors ranked based on the variance of the data points. The components in PCA are found by diagonalizing the empirical covariance matrix of the data. Similar to the CNN setting, suppose that our data is represented by tensor $X_{N \times (L \times L)}$, where N is the number of observations in the data-set and L is the length of our square image.

We can flatten this matrix into a 2-dimensional matrix of the form $X_{N \times D}$, where $D = L \times L$. We start by setting the mean of every row in matrix X to zero. Applying an orthogonal transformation to the result $X^T X$ and performing an eigendecomposition yields:

$$(X^T X)W_l = \lambda_l W_l \quad (4.6)$$

where $\{W_l\}_{l=1}^D$ is the set of eigenvectors, sorted by their corresponding eigenvalues. All of the eigenvalues λ_l are larger than zero because the covariance matrix is positive semidefinite. Intuitively, the eigenvectors with the largest eigenvalues, correspond to directions in the D -dimensional space for which the data-points have the largest variance. For this reason, we can use the top K eigenvectors as a linear dimensionality reduction method. One can build a columnwise orthogonal T such that $T = (W_1, W_2, W_3, \dots, W_K)$. When applied as a dimensionality reduction technique, we can select the $K \leq D$ elements. Then the optimal K -dimensional representation of data $X_{N \times D}$ is given by:

$$Z_{N \times K} = X_{N \times D} T_{D \times K} \quad (4.7)$$

The above equation, projects the original data matrix into a K dimensional space spanned by the top K eigenvectors found by PCA. In other words, PCA finds a lower dimensional space in which the data has the highest variance and projects the data into that space so as to capture the most variability in the data.

Autoencoders

Neural networks, unlike PCA, which applies a linear transformation to the input data, apply nonlinear transformations to the data in order to build the low-dimensional representation of the data.

For this reason, we have also examined the use of autoencoders. Autoencoders [177, 179] are artificial neural networks that are used for unsupervised learning of efficient low-dimensional representations of data. The main idea behind autoencoders is to pass the data through an intermediate layer whose number of learnable parameters is considerably smaller than the original information content of the data. The goal is to reconstruct the original data after passing through this bottleneck of information. This way, the neural network is forced to discover a nonlinear transformation that preserves the most important "patterns" or "structures" in the data to reconstruct the original data.

Fig 4.3 shows a schematic autoencoder with three hidden layers. Since we intend to apply autoencoders to image data for better clustering of naturally occurring patterns, we use Convolutional Neural Networks (CNNs) as our encoder and our decoder. Since CNNs use a method called parameter sharing to minimize the number of learnable parameters, using convolutional autoencoders significantly reduces the number of parameters needed to learn the most important features of the data. The latent variables are learned by passing training examples through the network and calculating the reconstruction-loss associated with reconstructing the original data-points

after passing through the bottleneck. Equation (4.8) below shows the loss function used in training the network,

$$\text{Reconstruction Loss} = \frac{1}{N} \sum_{i=1}^N \left(X_i^{\text{predicted}} - X_i \right)^2. \quad (4.8)$$

In the above equation, X_i is the i -th image in the dataset. Reconstruction loss is then backpropagated to re-tune the weights of the network. The number of latent variables in the center of an autoencoder, determines the number of dimensions of our learned representation. For example, in Fig. 4.3, there are three neurons in the central layer which means any given image is transformed into a 3-dimensional vector representation. Similar to PCA, the application of an autoencoder for dimensionality reduction can be formulated as follows:

$$Z_{N \times K} = f(X_{N \times D}) \quad (4.9)$$

Here, function $f()$ represents the nonlinear transformation applied by the trained neural network and K is the number of neurons (latent variables) in the center of autoencoder.

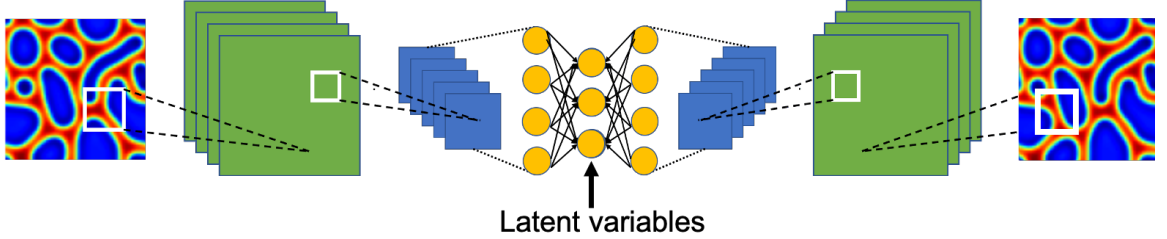


Figure 4.3: Convolutional autoencoder is built by stacking a convolutional neural network with a mirror version of itself. The latent variables in the middle layer are forced to capture the most important features of the image to recreate it in the output.

Variational autoencoders (VAE) [180] are a modern version of autoencoders. Compared to autoencoders, VAEs impose additional constraints on the encoded representations. Regular autoencoders learn an arbitrary function to encode and decode the

data, however, VAEs learn the parameters of a probability distribution modelling the data. In simple words, a variational autoencoder (VAE) provides a probabilistic approach for describing an observation in latent space. VAEs model latent variables as probability distributions rather than fixed values.

In VAEs the weights of the neural network are simultaneously optimized using two loss functions, reconstruction loss, which captures the difference between the generated data and the original data, and the KL divergence between the learned latent latent distribution and a prior unit Gaussian probability distribution. The second loss function enforces the learned representation of similar images to be close in the latent space by penalizing the network when the learned probability distribution is far from a prior unit Gaussian distribution. VAEs are especially more effective than regular autoencoders when the goal is to learn the latent parameters of a stochastic process. This is because they tend to learn the generative process that generates the data rather than trying to reconstruct a specific instance.

4.4.2 Clustering

***k*-means Clustering**

k-means is a clustering algorithm that clusters N points into k cluster [181]. It operates by minimizing the sum of squared distances between the points and their respective cluster centroids. The goal is to assign each point to its nearest cluster center and to have the cluster centers as distant from each other as possible. *k*-means takes the number of clusters k as an input to the algorithm. The algorithm starts with a random assignment of points to clusters and finds cluster centroids. In the next step, the algorithm re-assigns points to clusters based on current coordinates of the cluster centroids and recalculate new centeroid based on new assignments. The algorithm then repeats this process until some convergence criteria is satisfied. This also allows for new points to be classified based on their nearest cluster centroid.

Gaussian Mixture Clustering

Gaussian Mixture Models (GMMs) [182] is another algorithm used for segmenting a data-set into a number of clusters. GMM assumes that the data are characterized by a number of multivariate Gaussian distributions in the data, and each of these distributions represent a cluster. GMM is considered a soft clustering algorithm because cluster assignments are probabilistic. Given a data-set and a given number of clusters k , the GMM tries to find the parameters of k multivariate Gaussian distributions that best fit the data.

4.5 Results and Analysis

4.5.1 Supervised Classification of Patterns Generated by Gray-Scott Model

Supervised classification assumes there is a pre-classified training set. These data points, in our application, are manually classified by a human or another pre-existing algorithm. The network learns to predict the labels of the samples in the training set by iteratively readjusting its weights based on the error corresponding to its predictions in the latest iteration. The neural network is then tested by feeding it a test set that is unseen by the model. The neural network used in this section is a convolutional neural network with two convolution layers, each having 32 filters, followed by a dense layer with 100 neurons and an output layer with number of neurons equal to the number of classes, in this case 7. Here we generate a series of patterns by simulating the system of equations in the the Gray-Scott model with certain values for F and K . Since we manually generate the images with specific parameters, we know the general class that each image belongs to. We use these labels to train and evaluate the model. Figure 4.4 shows the patterns used for the supervised classification model. In this experiment, we generated 2000 images for each of the 7 patterns. We used 80 percent of the data in the training set and evaluated the data using the remaining 20 percent.

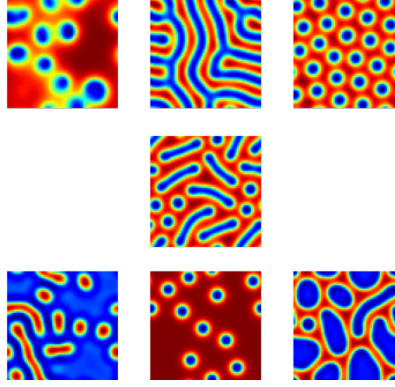


Figure 4.4: Collection of 7 patterns from Gray-Scott equations chosen for this work.

Figure 4.5 shows the accuracy of the model as a function of number of training iterations. As we observe, the accuracy of the model quickly goes up and reaches a plateau. Further training the model might result in over-fitting to the training data and hence decrease its performance on the test set. In the final training iteration, the accuracy of the pattern classifier is approximately 99%.

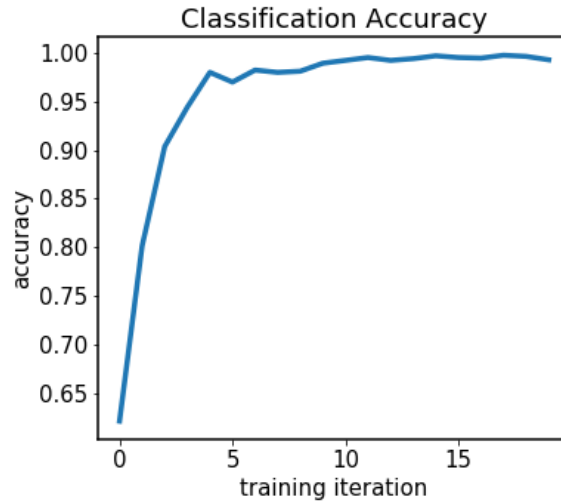


Figure 4.5: Classification accuracy as a function of training iterations. The model reaches the maximum accuracy of around 99% in early stages of training.

The performance of the model is impressive. Among the 2800 images which were unseen by the model, it only miss-classified 6 images. It is worth noting that there are

many hyper-parameters involved in defining a convolutional neural network model. For this reason, in order to obtain the maximum achievable performance on a data-set, one should perform a hyper-parameter search in the space of possible hyper-parameters and use the set of hyper-parameters with the highest accuracy results on test data.

4.5.2 Supervised Regression of Patterns of Gray-Scott Model

Finding the underlying generative process that gives rise to a specific pattern is a central problem in fields ranging from ecology to materials science. In this section, we use supervised learning techniques to map a given pattern to a set of F and K parameters in the Gray-Scott system of equations. The task of predicting a continuous dependant variable given a number of independent variables or features is called regression analysis. In order to predict F and K parameters given an observed spatial pattern we train a convolutional neural network. The data-set for training this model is created by simulating the set of Gray-Scott equations with random F and K parameters and random initial conditions. In the training phase, the images are fed to the convolutional neural network. The output layer of the network consists of two neurons with linear activation functions that serve as predictors of our F and K parameters. The network is trained by backpropagating the loss associated with the learning process. The loss function in this case is root mean squared error (RMSE) between model predictions and actual values of the F and K parameters.

Figure 4.6 shows the result of applying our trained regression model on Gray-Scott patterns. The first row is the test images generated by simulating the Gray-Scott equations by picking a set of random F and K parameters. The images in the first row are fed into the trained neural network and the corresponding predicted F and K are extracted. In order to visually compare the results, we use the predicted F and

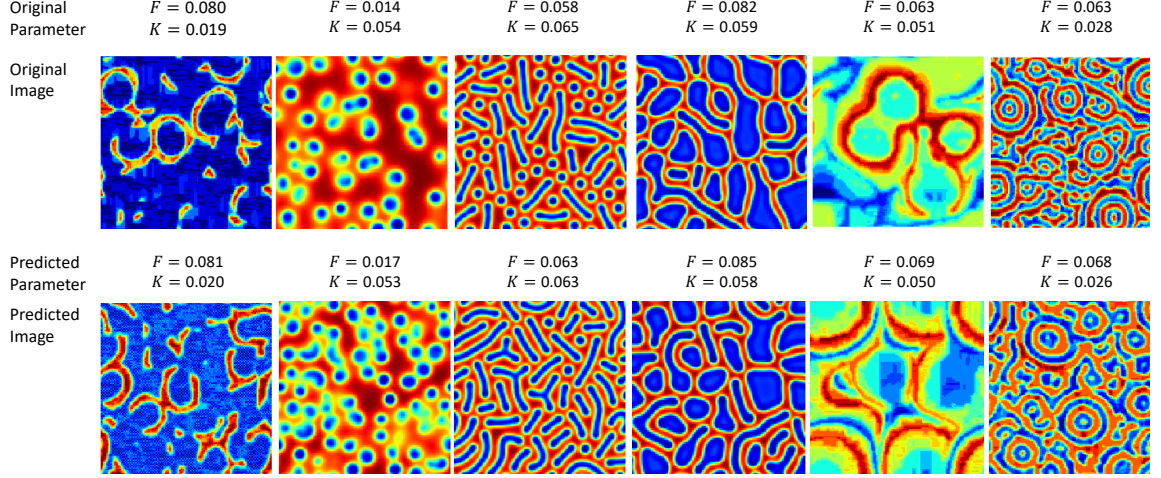


Figure 4.6: First row shows images generated from simulating the Gray-Scott equations with random set of F and K parameters. Images in the second row are generated by feeding the first row images to our trained regression model, getting model predictions for F and K , and simulating the Gray-Scott equations with these F and K parameters with random initial conditions.

K parameters to generate the second row of images. F and K values corresponding to original and predicted images are shown in the image. It is worth noting that the initial condition for the set of differential equations in all of our experiments is set to random Gaussian noise with a randomly changing seed.

In order to evaluate our model in a real-world scenario where a researcher observes a new spatial pattern in a driven-diffusive system and is looking to find the appropriate model that can generate a similar spatial distribution, we take three real images from [7] that are examples of vegetation patterns formed in dry-lands and apply our trained model to find the corresponding parameters in Gray-Scott equations that produce a similar spatial patterns.

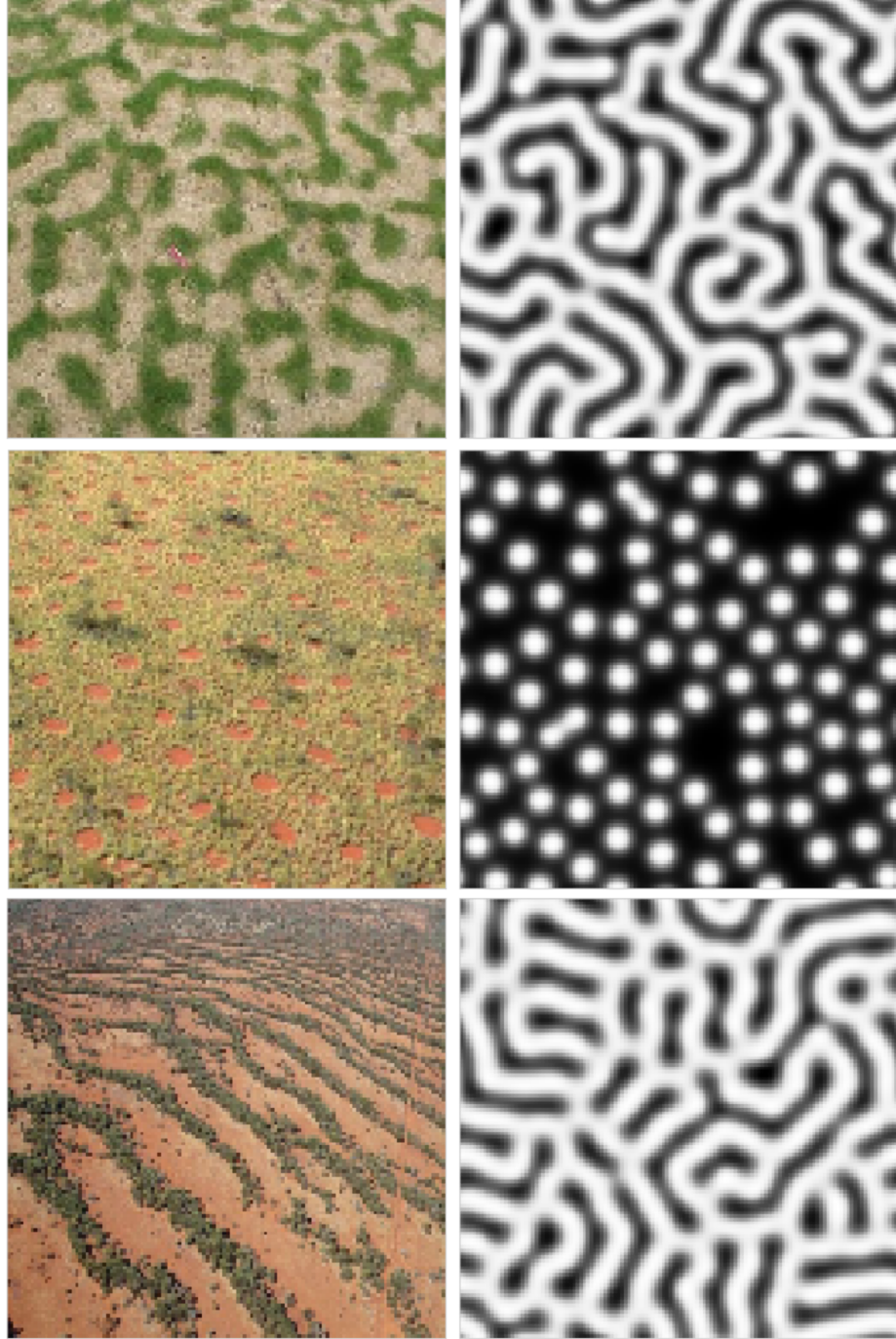


Figure 4.7: The left column shows real vegetation patterns taken from [7]. The right column shows the mapping of these patterns to the Gray-Scott patterns based on the predictions of our trained model.

Figure 4.7 shows real images taken from [7] along with our model’s predictions. For each image in the left column, our model predicts an F and K value, which we

feed to the Gray-Scott equations with random initial conditions to create the images on the right. In the first two examples, our model was able to successfully find very close mappings of such patterns in the Gray-Scott system of equations. However, on the third row, our model fails to find a comparable pattern. In this specific example the vegetation pattern developed on slope, which induces an external field and directionality to the patterned system. However, such examples with non-homogeneous directionality are absent in the training set created by Gray-Scott system of equations. This inability to detect similar patterns also carries some information about the set of generatable patterns in the system under investigation.

4.5.3 Unsupervised Learning Patterns of Gray-Scott Model

As discussed earlier in Section 4.4, unsupervised learning techniques are used in data segmentation and classification when there are no known labels or classes associated with the data. In this section, we first apply dimensionality reduction techniques on patterns of Gray-Scott model shown in Fig. 4.4. We then utilize the k -means clustering and Gaussian mixture models to cluster the resulting data-points into different classes. The data used in all future subsections is 14000 images generated by simulating the Gray-Scott model with 7 sets of different parameters. This means that for each pattern, there are 2000 data-points in the data-set.

PCA

Fig. 4.8 shows result of applying PCA on the data. The figure is colored using our prior knowledge of the class the data-points belong to. The algorithm has no information about these labels we use them only to visualize how the model performs in terms of creating visually differentiable clusters. After applying this dimensionality reduction method, we need to apply a clustering algorithm to see how we perform on segmenting these embedded points into correct clusters. For this purpose, we use both k -means and GMM clustering. It is worth noting that, in this Section and the

following Section, the patterns are mapped into a 2-dimensional space for illustrative purposes. The number of dimensions of the mapping space is a hyper-parameter of these models and can have significant effects on performance. Therefore, in a real-world scenario, a careful hyper-parameter search is required to find the size of the latent space which yields the highest performance. In Section 4.5.3.2, we choose a different latent space size to quantitatively compare the results of various algorithms.

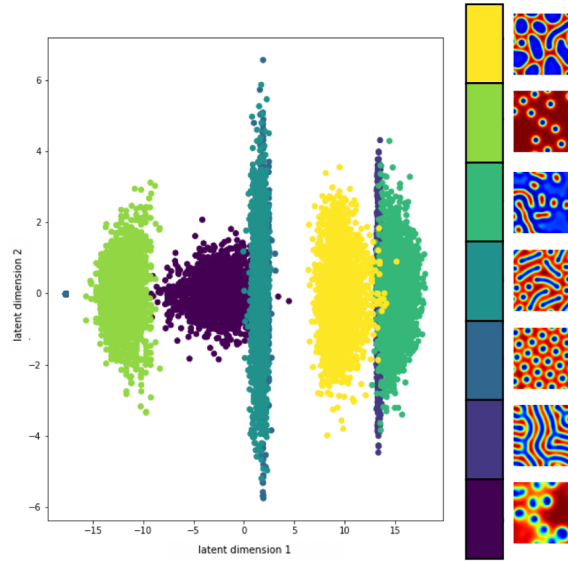


Figure 4.8: PCA applied to 7 patterns of Fig 4.4. Each color refers to a specific type of pattern generated from a specific set of F and K parameters. The figure is colored based on our previous knowledge for visualization purposes and the algorithm does not have access to these labels.

Fig 4.9 shows the result of using the GMM algorithm with a mixture of 7 Gaussian distributions on the PCA-transformed data. Here, we show these results as an illustrative example for the reader. In Section 4.5.3.2, we compare different dimensionality reduction and clustering algorithms using quantitative metrics.

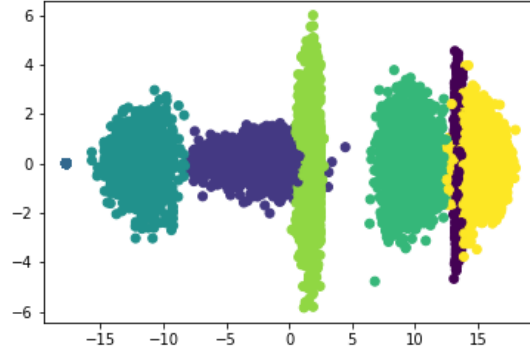


Figure 4.9: GMM clustering applied to the results of PCA. Here the colors denote the way GMM has separated different clusters. Compared to k -means, we see more accurate differentiation between clusters.

Variational Autoencoder

Figure 4.10 shows the result of applying VAEs to the pattern images. Again, points are colored based on our prior knowledge for the purpose of visualization. Compared to PCA, VAE generates clusters that are more visually distinguishable.

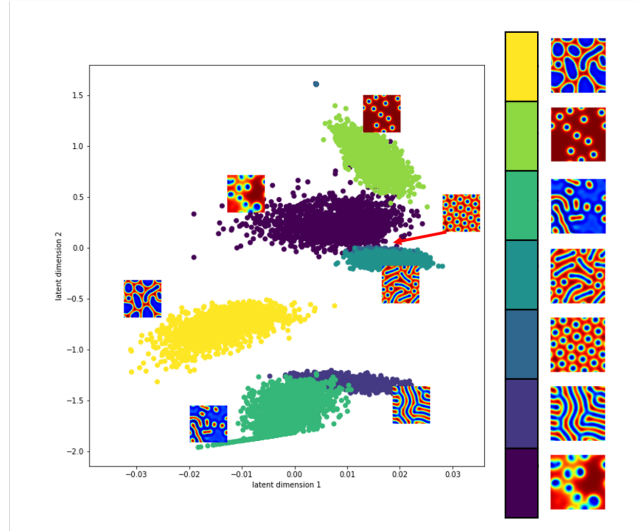


Figure 4.10: VAE applied to 7 patterns of Fig 4.4. Each color refers to a specific type of pattern generated from a specific set of F and K parameters. The figure is colored based on our previous knowledge for visualization purposes and the algorithm does not have access to these labels.

This means that without any supervision, the algorithm has been able to separate different patterns solely based on their visual features. In this figure, we have plotted the patterns next to their corresponding clusters to show how spatial distance in this transformed space matches the visual similarity/non-similarity of images. The upper right region of the plot, belong to patterns that are dominantly red and are very similar in composition. Colors ranging from red to blue correspond to dominance and concentration of one of the two reactants in Gray-Scott system of equations. In particular, patterns 3 and 4 from the bottom in the color-bar are very closely packed together in the plot. This is interesting since the combination of worms and dots are very close in the space of patterns of Gray-Scott equations and converge to one-another in many scenarios depending on the initial conditions. It is also worth noting that these two patterns are not well-separated in the 2-dimensional mapping shown in the figure; however, if mapped to a higher dimensional space, they might become better separable. The left bottom side of the figure belongs to mostly dominant blue patterns which have some level of similarity. The yellow cluster that belongs to bubble patterns is somewhat far from most of the clusters present in the figure. This is also true in the actual F and K phase space of Gray-Scott patterns, since bubble patterns form in regions with very large values of F and K compared to the other patterns under study. The meaningfulness of this distance metric can have far-reaching implications in a more quantitative study of patterned systems.

Fig 4.11 shows the result of using the GMM algorithm with 7 Gaussian distributions on the VAE-transformed data. Similar to what we mentioned above about PCA, Fig 4.11 is only an illustrative example of how GMM works on the VAE-transformed data. We will investigate these algorithms in a more quantitative manner in Section 4.5.3.2.

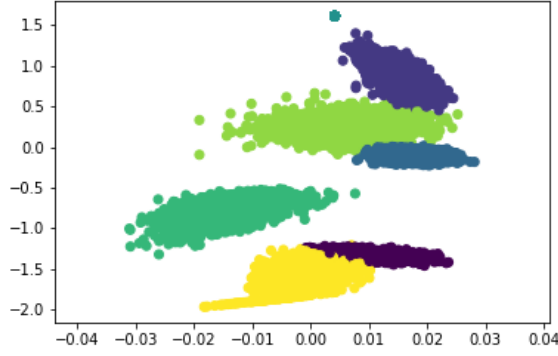


Figure 4.11: GMM clustering applied to the result of VAE. Colors are specified by the algorithm to separate different detected Gaussian distributions.

Minkowski Measures

As discussed in the Introduction Chapter, the literature on categorizing patterns based on quantitative metrics is limited. The most prominent work in this area is the work of Mecke [1] on morphological characterization of patterns in reaction-diffusion systems. In this work, he introduced Minkowski measures along with some thresholding techniques to map images of patterns into a lower-dimensional space. He argues that this low-dimensional representation can serve as a quantitative measure to distinguish and categorize reaction-diffusion patterns. A pattern is considered to be an image with different values at each pixel. This can be represented by a gray-scale image, in which different pixel values can be regarded as different values of a certain quantity (i.e., density). According to [1], in order to extract geometric characteristics of a pattern, we first need to convert it to a binary image. For this purpose, threshold ρ is introduced. We sweep over the image pixel by pixel, and if the pixel value is larger than ρ , the pixel is declared black; otherwise, the pixel is declared white. After transforming the pattern into a two-dimensional black and white image, the following characteristics, called Minkowski measures, are calculated for the image.

- The area fraction $v(\rho)$ defined as the fraction of black pixels.

- The length of the boundary line $s(\rho)$ between black and white regions measured as the number of pairs of neighboring black and white pixels normalized by the total number of pixels.
- The so-called Euler characteristic $\chi(\rho)$ defined as the difference between the number of white connected components and black connected components normalized by the total number of pixels.

All these quantities are functions of ρ , the threshold to transform a grey-scale image to a black and white image. Therefore, Mecke postulated that plotting these quantities as a function of ρ should produce a different plot for different types of patterns with different morphological characteristics. Fig. 4.12 illustrates an example set of plots gained by varying the threshold and calculating the Minkowski measures introduced earlier. The plots in Fig. 4.12 are averaged over a large number of realizations of the pattern shown.

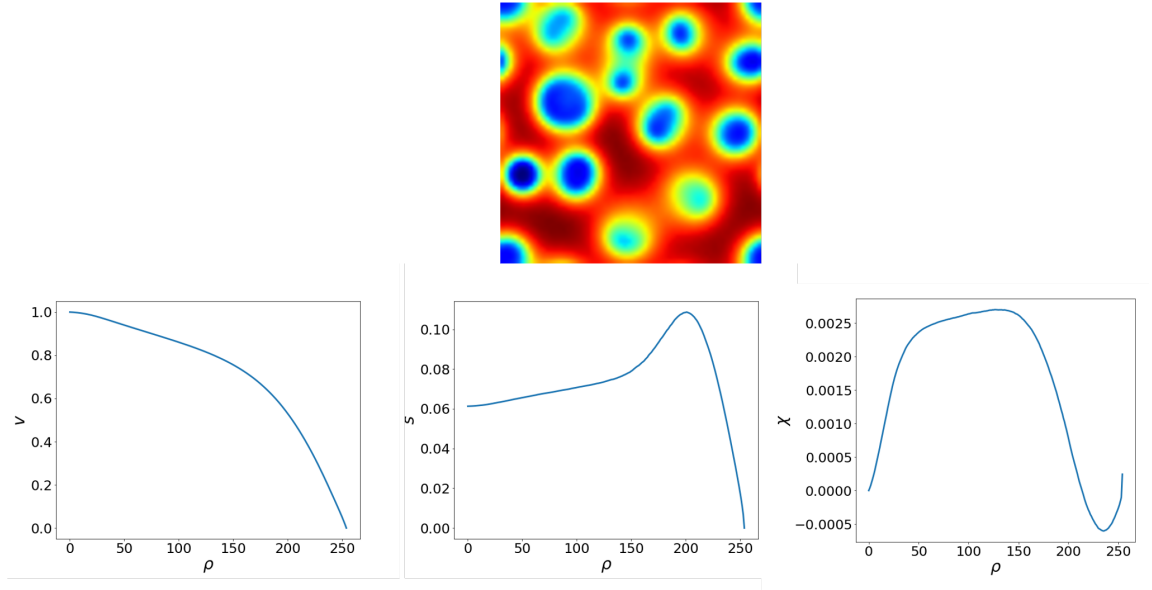


Figure 4.12: Minkowski measures as a function of threshold parameter ρ . All of the plots are averaged over a large number of realizations of the pattern shown above.

Mecke [1] argued that there are simple analytic combinations of the quantities $v(\rho)$, $s(\rho)$, and $\chi(\rho)$ that can be accurately described by low-degree polynomials. The coefficients of these low-degree polynomials can serve as a means to categorize different patterns observed in reaction-diffusion systems. Quantities P_v , P_s , and P_χ are defined as:

$$\begin{aligned} P_v(\rho) &= \tanh^{-1}(2v(\rho) - 1) \\ P_s(\rho) &= \frac{s(\rho)}{v(\rho)(1 - v(\rho))} \\ P_\chi(\rho) &= \frac{\chi(\rho)}{s(\rho)} \end{aligned} \tag{4.10}$$

We will use these quantities and the coefficients of low-degree polynomials derived from them to cluster and categorize Gray-Scott patterns in the future sections. We will then compare these results with the clustering results obtained from the machine learning algorithms introduced above.

4.5.3.1 Evaluation Metrics

In order to evaluate the performance of our dimensionality reduction and clustering algorithms, we use a metric commonly used in the unsupervised clustering literature, namely Adjusted Rand Index (ARI) [183, 184]. Given a set of n objects $S = \{o_1, \dots, o_n\}$, assume $U = \{u_1, \dots, u_R\}$ and $V = \{v_1, \dots, v_C\}$ represent two partitions of the objects in S . In other words, U divides the objects in S into R clusters and V divides the objects in S into C clusters. Note that the following relations hold for U and V :

$$\begin{cases} \bigcup_{i=1}^{i=R} u_i = \bigcup_{i=1}^{i=C} v_i = S \\ u_i \cap u_{i'} = v_i \cap v_{i'} = \emptyset \end{cases}$$

We also assume that clustering U is our ground truth, meaning that we have prior knowledge on the true partitioning of S . In order to define an accuracy metric which compares partitioning V to the ground truth U , we define the following:

- a , the number of pairs of elements in S that are in the same subset in U and in the same subset in V
- b , the number of pairs of elements in S that are in different subsets in U and in different subsets in V
- c , the number of pairs of elements in S that are in the same subset in U and different subsets in V
- d , the number of pairs of elements in S that are in different subsets in U and in the same subset in V

The Rand Index [183], RI is defined as:

$$RI = \frac{a + b}{a + b + c + d} = \frac{a + b}{\binom{n}{2}} \quad (4.11)$$

Here the denominator counts the total number of pairs of objects that one can choose from S . Equation 4.11 can be regarded as the number of correct decisions of clustering V compared to the ground truth clustering U . One key shortcoming of the Rand Index is that the expected Rand Index of two random partitions does not take a constant value. In [184], Hubert et al. proposed an adjusted version of the Rand Index which accounts for expected value of random partitions. Adjusted Rand Index (ARI), which is one of the most prevalent cluster validation metrics in the literature, takes the following form (for detailed derivation, please refer to [184, 185]):

$$ARI = \frac{\binom{n}{2}(a + b) - [(a + c)(a + d) + (b + d)(b + c)]}{\binom{n}{2}^2 - [(a + c)(a + d) + (b + d)(b + c)]}. \quad (4.12)$$

ARI , takes the value of 1 when the two partitionings are identical (Fig. 4.13) and takes the value of 0 when comparing two random partitioning.

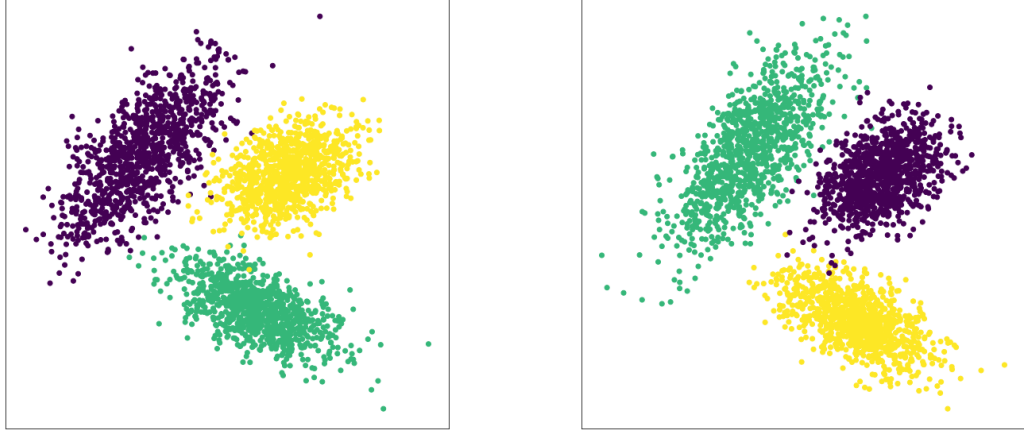


Figure 4.13: The two figures shown above represent two different clusterings of a set of data points in a two-dimensional space. In this case, the clusterings of the points are identical but are labeled (colored) differently. Therefore, in this case, $ARI = 1$.

ARI as defined above gives us the appropriate metric to compare different dimensionality reduction and clustering algorithms presented in the previous sections. As mentioned earlier, research works on quantitative definitions for pattern analysis are scarce in the literature. We presented Minkowski measures introduced in [1] as the one most similar to our dimensionality reduction techniques. Mecke's work is also the most representative example of the literature on pattern analysis as it is a general technique that can be applied to patterns formed in different fields of science. Therefore, we utilize Minkowski measures as a baseline to compare our results with the existing literature.

4.5.3.2 Clustering Results

In this section, we compare the clustering results using the ARI metric introduced above. There are three Minkowski measures introduced in section 4.5.3. As discussed earlier, the curves associated with simple analytic combinations of these measures

can be approximated using a low-degree polynomial (4.10). Mecke [1] showed that the combinations of these coefficients are different for different patterns. For this dissertation, we choose to approximate the quantities mentioned above (4.10) by degree 4 polynomials. Therefore, for a given pattern, each of the three quantities in (4.10) gives us a four-dimensional vector. We concatenate these four-dimensional vectors to create a 12-dimensional vector representation of an image. This can be viewed as a pre-engineered dimensionality reduction algorithm, in which each pattern image is mapped to a 12-dimensional space. Note that in all the dimensionality reduction algorithms introduced in this dissertation, one can choose the number of dimensions of the output space. In PCA, which applies a linear transformation to the image, one can simply choose the number of output dimensions. Similarly, in VAEs, one can choose the number of output dimensions by setting the number of latent variables. To make the results of different algorithms comparable, we choose the output dimensionality of all the algorithms to be 12. After applying various dimensionality reduction techniques to all of the images in the data set, we have a set of 14000, 12-dimensional vectors. We then apply k -means and GMM to cluster these 12-dimensional points into 7 clusters. It is worth noting that in section 4.5.3, we mapped all of the data points in the data-set into a two-dimensional space for the sake of visualization. In a real-world problem, one should vary the number of latent dimensions and observe the algorithms' performance to select the most efficient mapping. There is always a trade-off between mapping into a low-dimensional space and a high-dimensional space. If the number of latent dimensions is low, we might lose important information. On the other hand, increasing the number of latent dimensions will result in the problem of the sparsity of data points in the mapped space. Clustering algorithms will perform poorly on sparse high-dimensional data.

In Table 4.1, we compare various combinations of dimensionality reduction and clustering algorithms and compare the obtained clusterings with the ground truth

clustering to calculate the *ARI* value for each set of algorithms. In terms of clustering algorithms, GMM consistently outperforms *k*-means clustering. The best performing model which achieves $ARI = 0.96$ is the combination of VAE and GMM. Minkowski measures achieve a decent performance but fall short comparing to VAE. We also created a Combined model which outperforms all of the other single algorithms. We built this Combined model by taking the 12-dimensional representations from all three models (PCA, VAE, and Minkowski), projecting each 12-dimensional vector into a 4-dimensional space using PCA (note that PCA is a linear method that can be applied as many times to reduce the dimensionality of any given vector), and concatenating the three, 4-dimensional vectors to obtain a new 12-dimensional representation. This new 12-dimensional representation contains the most important information extracted by all three algorithms. The *ARI* value for this Combined model is 0.99 which is an outstanding result. This finding also proves that each of the three methods introduced in this Chapter, extract different types of information from the pattern images and can complement one another.

It is worth noting that the only input to the unsupervised learning algorithms such as PCA and VAE is the pattern images. On the other hand, geometric characteristics such as Mikowski measures are carefully hand-designed based on years of research and observation of many patterns. In light of these notions, the performance of unsupervised learning algorithms in clustering and classifying patterns is impressive and needs more attention from the research community in this field.

	PCA	VAE	Minkowski	Combined
<i>k</i> -means	0.77	0.82	0.38	0.26
GMM	0.88	0.96	0.92	0.99

Table 4.1: *ARI* value of different combinations of dimensionality reduction and clustering techniques. To calculate *ARI*, each clustering is compared to the ground. The Combined model which achieves an outstanding performance is created by combining the results of all three models.

4.6 Conclusion and Future Work

To conclude, we show that machine learning algorithms can aid researchers in different stages in life-cycle of the study of patterns. A class of problems arises when there is a finite set of observable patterns in a given system, and researchers wish to classify a new pattern instance in an efficient and accurate manner. One example is to distinguish the vegetation patterns observed in a stream of satellite images. We showed that classification algorithms are suitable for this task given a small set of training data. Given 2800 samples from different patterns that were unseen by the model, our model achieved an accuracy of 99%. The second class of problems arises when a pattern is known to be generated by a specific generative model or needs to be mapped to a specific system of equations, i.e., predicting the underlying parameters of an observed instance of a chemical reaction-diffusion system. Using an image convolutional neural network, we showed that a neural network can be trained to predict the F and K parameters of the Gray-Scott model. Our model was successful in predicting the F and K parameters with reasonable accuracy. Similarly, this method can be used to map a given instance of a pattern into a set of candidate generative models, which gives researchers an exploratory tool for analyzing newly observed systems. One commonly overlooked shortcoming in the study of patterns is that there is no quantitative approach in distinguishing patterns generated from diverse systems. The literature usually refers to observed patterns by general terms such as mazes, stripes, etc. However, this approach is bounded by our cognitive limits and lacks a universal method to define the patterns. In the last section, we use unsupervised learning techniques to learn the common discriminative features that partition a set of patterns. We perform this by learning a transformation to map a set of patterns into a lower-dimensional space. We observe that patterns belonging to different classes are naturally separated into distinguishable clusters and utilize unsupervised clustering algorithms to separate them. In addition, we compare

our results with Mecke’s [1] work on using morphological and geometric features of patterns to map them to a lower-dimensional space. Our extensive experiments using various unsupervised learning and geometric techniques show that VAEs combined with GMMs outperform all other methods in clustering our data-set of patterns. It should be noted that one of the most important characteristics of this mapping is the observation that proximity in the pattern space is preserved in the transformed space, meaning that patterns that have visual similarities are more closely clustered together, and patterns that look visually different are further apart in the transformed space. This could be a significant finding since, given a sufficient amount of input data, the distances in the transformed space can become a good quantitative measure to find where a newly observed pattern belongs in the space of all patterns.

One important property of our unsupervised learning approach is that it can be applied in a hierarchical manner. A model trained on all the variants of patterns observed on leopards will be able to map a newly observed instance in a fine-grained space of leopard patterns. Similarly, a large model can be trained using a zoo of patterns generated from various generative models. This comprehensive model can play the role of quantitatively determining where a pattern belongs in the space of all the given patterns. This could also open up the possibility of having hybrid class memberships, i.e., maze-spots for a pattern that lies halfway between mazes and spots in the transformed space.

There are many open areas for future work in this area. Both supervised and unsupervised classification models introduced in this work can be extended to combinations of patterns generated from distinct underlying dynamics. Another interesting future direction would be to use the dynamic behavior of these patterns instead of a single image. This can be done by changing the structure of our neural network to a convolutional-recurrent structure that can capture the spatial and temporal behavior of the patterns simultaneously.

CHAPTER 5

CONCLUSION AND FUTURE WORK

In this Chapter, I pose some of the open questions relevant to each chapter of this work based on the conclusions and findings of this dissertation. Each of the following sections will focus on one of the chapters of this dissertation.

5.1 Robust Network Connectivity

In Chapter 2, we introduced a hierarchy of robustness measures for quantifying various levels of connectivity in graphs. We studied the critical thresholds and critical behavior of these robustness measure on the square lattice. Our theoretical and numerical analysis showed that percolation thresholds do not necessarily change as we increase the levels of robustness in the network. In fact, 2-stub, 2-core, 2 and 3-connectivity, and 2-strong connectivity all have the same threshold as ordinary percolation on the square lattice. In addition, we numerically found the thresholds for all other robustness measures for all k except for 4-connectivity. We left 4-connectivity out due to the computational complexity of finding the 4-connected components. However, numerical and theoretical study of 4-connectivity on the square lattice is very important for the field and can have far-reaching implications in network design and analysis.

5.1.1 Exploring Naturally Formed Networks

Many technological innovations have been inspired by the observation of precise algorithmic behaviors in nature. One interesting future direction of this work is to

investigate naturally formed networks and find the levels of robustness that these networks maintain in order to avoid catastrophic failures. It has been shown that many biological networks [32] ensure the existence of different pathways to ensure robustness. Investigating degrees of robustness in various naturally formed networks can help us understand how naturally formed networks maintain stability in complex dynamic environments.

5.1.2 Robust Connectivity in Real-World Networks and Random Graphs

Although square lattice is a good simplified representation of many real-world networks such as molecular networks, it fails to capture many of the complex structures present in real-world problems. One natural extension of our work is to study these robustness measures on spatial networks such as road networks, random geometric graphs, and power grids. Random geometric graphs are especially interesting since as one increases the number of nodes per unit area, the network becomes denser and denser; therefore, these measures of robustness can be studied for all possible values of k up to infinity. Random geometric networks are formed in a continuous plane. Introducing dynamics in a geometric graph formed in a plane can model many real-world temporal phenomena. Mobile ad-hoc networks are an example of such networks. These networks evolve in time as the components of the networks are dynamically changing and moving in space. Robustness to random failures in the aforementioned networks is crucial for their proper functionality, therefore studying the robustness measures introduced in this dissertation on mobile ad-hoc networks in an interesting future direction. A phenomenological study of emergence of robust connectivity in the systems mentioned above always poses the question of design and control. Therefore, the next meaningful question is how to design robust networks or how to manipulate a given network to make it robust? For example, given a sub-critical mobile ad-hoc network or a random geometric graph on a continuous plane,

how can we manipulate a finite number of nodes/edges to make it robust based on different definitions of robustness?

As mentioned in Chapter 2, Newman et al. [31] studied 2-connectivity on real-world networks and showed that the thresholds for 2-connectivity are the same as the threshold for ordinary percolation. However, a rigorous study of the critical behavior of various robustness measures in real-world networks and random graphs is missing in the literature. In this dissertation, we showed that we observe significant deviations from ordinary percolation behavior for different values of k and different robustness measures. Some robustness measures undergo discontinuous phase transitions, and others belong to not previously observed universality classes. Understanding the critical behavior of these transitions in real-world networks and random graphs is of utmost importance for their design and analysis. The sharpness of the phase transition, cluster size distribution at the different stages of criticality, and the nature of transition (continuous vs. discontinuous) are essential in real-world scenarios such as road traffic networks or communication networks.

5.1.3 Robustness in Heterogeneous Networks

Many real-world networks are not made of a single component type. For this reason, studying the robustness of such networks due to the failure of components needs more careful analysis. For example, a power grid consists of nodes of different types, namely, power plants, substations, etc. The probability of failure of each type of component is different since they are built using different standards. One fascinating and practical question to ask is, how does the interplay between these different probabilities impact the emergence of global connectivity in the system? How does this multi-threshold phenomenon change the critical behavior of the percolation transition?

5.2 Connectivity Transitions in Non-equilibrium Systems

In Chapter 3, we studied the transition of connectivity in the time-evolution of an interacting multi-particle system. We introduced a multi-particle interaction model, that produced a continuous phase transition. We showed that by varying a parameter of this interaction model, we can continuously change this transition's critical exponents and thresholds. The phase transitions observed in our model belong to the weak universality paradigm, in which critical exponents vary continuously, however, their ratios remain constant. The aforementioned model undergoes different regimes of pattern formation until it reaches a steady state. One straightforward future extension of this work is to study the same multi-particle model under different initial conditions and with other types of lattice structures or general networks. Regular lattices have a uniform degree distribution, meaning that all the nodes have the same degree across the network; therefore, we expect to observe a similar behavior on other regular lattices. On the other hand, the non-uniform degree distribution of general networks ensures the existence of some high degree nodes. Depending on the initial conditions of the multi-particle system, these high degree nodes (with a high number of neighbors) can act as sink-hole of particles. Any particle that resides on one of these high degree nodes has a high probability of staying on the same node in future time-steps. The scenario above is an intuitive example of how particles might evolve on general graphs. Detailed simulations and theoretical studies are needed to understand the behavior of our model on general graph structures. In the following sections, I will elaborate on other possible future directions of this work.

5.2.1 Cluster Analysis of Multi-Particle Model

A preliminary analysis of cluster size distribution at the critical point showed that increasing the interaction strength delays the phase transition. For this reason, the number of clusters with small numbers of particles decreases significantly at the crit-

ical point. As the number of free particles or small clusters decreases, most of the particles join the largest connected component. This enhanced correlation between particles results in a decrease in the percolation threshold of this system. One important question that remains unanswered in this dissertation is the functional behavior of the percolation threshold and critical exponents as α increases to infinity. In this work, we observed the appearance of filamentation patterns as the system approaches the critical point. However, there are distinguishable visual differences (Fig. 5.1) between filamentation patterns as α is varied. At higher values of α , the clusters look denser and with fewer holes in them. Studying the hole size distribution in this problem and similar problems could give us great insights into the phase transition shape and point of occurrence.

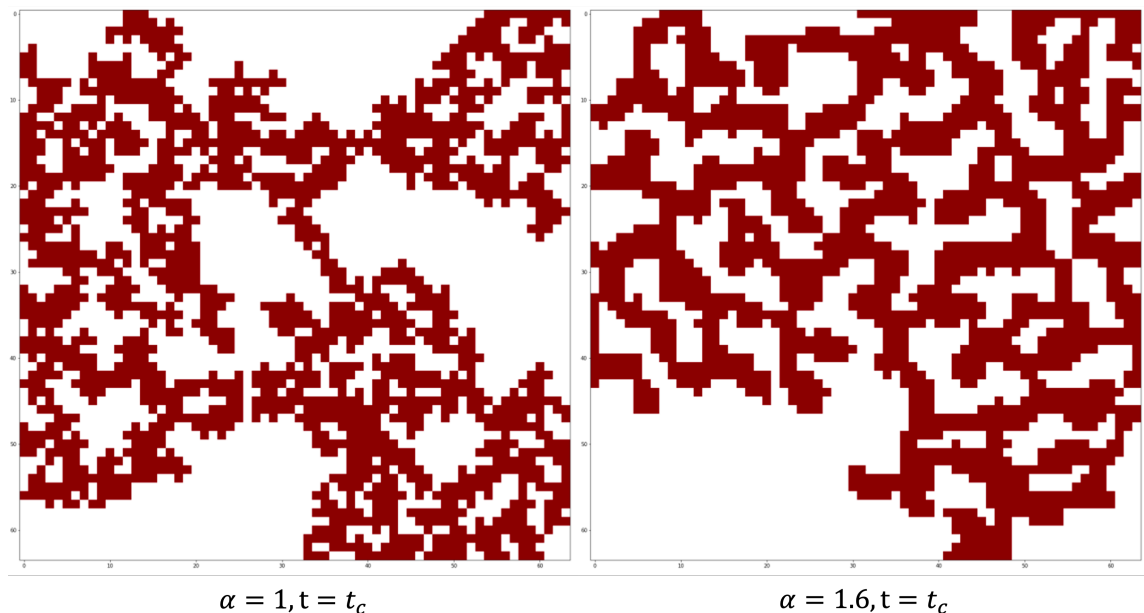


Figure 5.1: Largest connected component (LCC) for different values of α at $t = t_c$. There are significant qualitative differences between the two patterns. One observable difference between the two images is the hole size distribution in the LCC.

5.2.2 Connectivity Transitions in Other Reaction-Diffusion Systems

In Section 3.6, we studied a model similar to our multi-particle system in a continuous plane. We showed that if we generate a network based on nearest neighbors in the continuous plane and study the temporal evolution of connectivity, we observe a continuous phase transition. This interesting observation shows that our multi-particle model is part of a class of models that undergo a phase transition of connectivity. One interesting future direction of this work is to investigate the temporal behavior of connectivity in various types of multi-particle and reaction-diffusion systems. As an example, in Chapter 4, we introduced Gray-Scott equations. In this system of equations, different parameter regimes lead to the formation of different patterns. One can study the transition of connectivity in such systems and investigate the effect of steady-state patterns on the existence of a phase transition. There are numerous other multi-particle systems that can be the subject of such a study. The study of connectivity in these systems can have a crucial impact on different fields of science and engineering. For example, vegetation patterns in forests and dry-lands are very important in ecological studies and in managing environmental disasters such as forest fires. Many studies [186] focus on modelling the generative processes behind the evolution of these patterns. Global connectivity of these systems and their temporal dynamics through seasons and climates can play a central role in preventing uncontrollable fires that spread quickly.

5.3 Machine Learning Analysis of Patterns

In Chapter 4, we used machine learning algorithms to analyze patterns generated from reaction-diffusion systems. Although we tested these algorithms on a specific set of patterns generated from the Gray-Scott model, these techniques can be used to analyze any pattern that can be represented as a two-dimensional matrix. To the best of our knowledge, this is the first comprehensive study of application of

machine learning algorithms in reaction-diffusion patterns analysis. We introduced three different types of tasks in pattern analysis and addressed each task with a set of algorithms from the field of machine learning:

1. Pattern Regression: Given an instance of a pattern with a known generative function, predict specific parameters of the generative function that produces a similar pattern.
2. Supervised Pattern Classification: Given an instance of a pattern and a catalog of predefined patterns, detect which category the instance belongs to.
3. Unsupervised Pattern Classification: Given a large data-set of various types of patterns, partition this data-set into groups of similar patterns.

In tasks 1 and 2, we used supervised convolutional neural networks. We showed that this method achieves exceptionally high accuracy in both tasks. For task 3, we utilized a combination of different dimensionality reduction techniques combined with different clustering algorithms. In order to compare our work with pre-existing methods, we implemented Mecke’s [1] pattern analysis method as a dimensionality reduction algorithm. Our results showed that auto-encoder, which is a neural network-based architecture, outperforms geometric measures introduced in [1]. Another significant finding was that combining various types of dimensionality reduction methods to capture various underlying features of the images performs significantly better than any individual method. Using this combined method, we achieved an ARI (Adjusted Rand Index, an accuracy measure introduced in Chapter 4) of 0.99. In the following sections, I will go over some future directions of this work.

5.3.1 Classifying Patterns From Diverse Generating Functions

In this dissertation, we studied the problem of pattern classification on various patterns generated from the same generative model (Gray-Scott model). One natural

continuation of the current work is generating patterns from multiple generative models, labeling them, and training a convolutional neural network to classify them. This also naturally plays the role of detecting the underlying generative model of a given pattern. If successful, this will be a breakthrough in pattern analysis since finding the appropriate generative model always puzzles researchers and requires extensive amounts of effort to solve.

5.3.2 Embedding Pattern Dynamics

Many pattern generative models result in visually indistinguishable patterns. Patterns of spots generated from the Gray-Scott and Cahn-Hilliard [187] models may look visually and geometrically the same but are generated from entirely different dynamics. The methods introduced in this dissertation are incapable of distinguishing such similar patterns based on single snapshots. Therefore, there is a necessity for creating algorithms that can take the temporal aspects of pattern formation into account.

One approach to this problem is to use the same techniques introduced in this dissertation for the embedding of an image into a d -dimensional space and embed temporal snapshots of the pattern dynamics into this space. This way, one creates a path in a d -dimensional space. Fig. 5.2 shows an example of such temporal embedding. In this figure, each data point is created by mapping the image of the pattern at time t to a 2-dimensional space using PCA. In Fig. 5.2, colors denote time. One can perform this embedding for various types of pattern formation dynamics and study the difference between the low-dimensional representation of the paths.

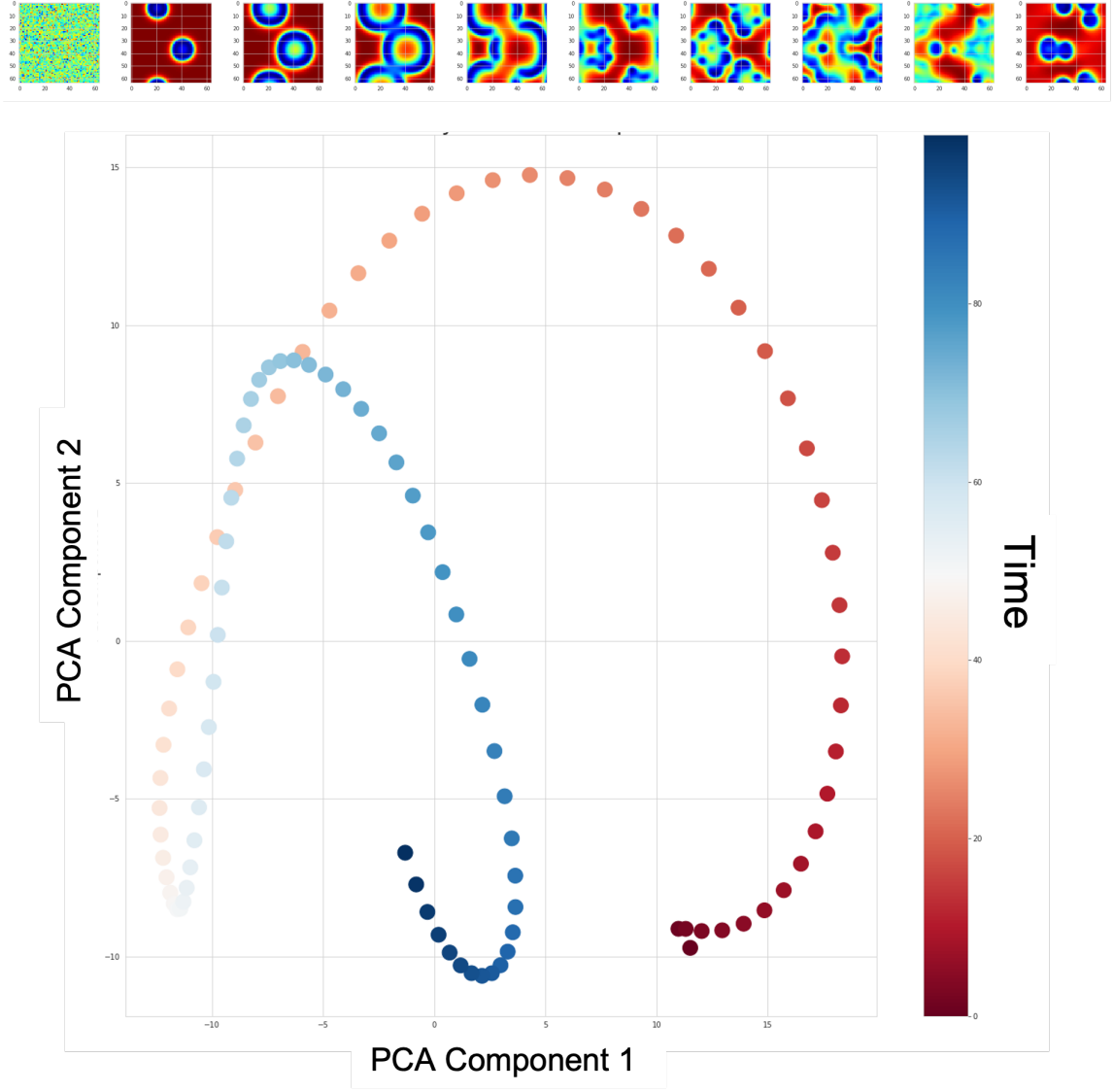


Figure 5.2: Path of a pattern in PCA space. Colors denote time. Dark red denotes $t = 0$ and dark blue denotes $t = 100$. At the top, we see example snapshots of the evolution of the pattern in time. The pattern is called Chaos in Gray-Scott category of patterns.

Another interesting possible approach is to use a machine learning algorithm that incorporates time into its embedding generation. For this purpose, recurrent neural networks (RNNs) are a great candidate. One can build a recurrent-convolutional neural network architecture and embed the temporal dynamics of a pattern into a point in a low-dimensional space. When the embedding step is done, all the clustering

methods introduced in this dissertation can be applied to cluster points into similar groups in a supervised or unsupervised manner.

BIBLIOGRAPHY

- [1] K. Mecke, “Morphological characterization of patterns in reaction-diffusion systems,” *Physical Review E*, vol. 53, no. 5, p. 4794, 1996.
- [2] J. C. Gimel, D. Durand, and T. Nicolai, “Transition between flocculation and percolation of a diffusion-limited cluster-cluster aggregation process using three-dimensional monte carlo simulation,” *Physical Review B*, vol. 51, no. 17, p. 11348, 1995.
- [3] P. Bruschi, P. Cagnoni, and A. Nannini, “Temperature-dependent monte carlo simulations of thin metal film growth and percolation,” *Physical Review B*, vol. 55, no. 12, p. 7955, 1997.
- [4] W. Ettoumi, J. Kasparian, and J.-P. Wolf, “Laser filamentation as a new phase transition universality class,” *Physical review letters*, vol. 114, no. 6, p. 063903, 2015.
- [5] M. Mijalkov, A. McDaniel, J. Wehr, and G. Volpe, “Engineering sensorial delay to control phototaxis and emergent collective behaviors,” *Physical Review X*, vol. 6, no. 1, p. 011008, 2016.
- [6] J. E. Pearson, “Complex patterns in a simple system,” *Science*, vol. 261, no. 5118, pp. 189–192, 1993.
- [7] E. Meron, “Vegetation pattern formation: The mechanisms behind the forms,” *Physics Today*, vol. 72, no. 11, pp. 30–36, 2019.
- [8] A. Chaudhary and R. D. Yadav, “A review on virus protein self-assembly,” *Journal of Nanoparticle Research*, vol. 21, no. 11, pp. 1–13, 2019.
- [9] F. Cucker and S. Smale, “Emergent behavior in flocks,” *IEEE Transactions on automatic control*, vol. 52, no. 5, pp. 852–862, 2007.
- [10] L. Wang, X. Li, Y.-Q. Zhang, Y. Zhang, and K. Zhang, “Evolution of scaling emergence in large-scale spatial epidemic spreading,” *PloS one*, vol. 6, no. 7, p. e21197, 2011.
- [11] J.-M. Lehn, “Perspectives in supramolecular chemistry—from molecular recognition towards molecular information processing and self-organization,” *Angewandte Chemie International Edition in English*, vol. 29, no. 11, pp. 1304–1319, 1990.

- [12] P. Gray and S. Scott, "Autocatalytic reactions in the isothermal, continuous stirred tank reactor: Oscillations and instabilities in the system $a + 2b \rightarrow 3b$; $b \rightarrow c$," *Chemical Engineering Science*, vol. 39, no. 6, pp. 1087–1097, 1984.
- [13] P. Csermely, *Weak links: the universal key to the stability of networks and complex systems*. Springer Science & Business Media, 2009.
- [14] M. T. Gastner and M. E. Newman, "The spatial structure of networks," *The European Physical Journal B-Condensed Matter and Complex Systems*, vol. 49, no. 2, pp. 247–252, 2006.
- [15] S. V. Buldyrev, R. Parshani, G. Paul, H. E. Stanley, and S. Havlin, "Catastrophic cascade of failures in interdependent networks," *Nature*, vol. 464, no. 7291, p. 1025, 2010.
- [16] F. Croccolo and H. E. Roman, "Spreading of infections on random graphs: A percolation-type model for covid-19," *Chaos, Solitons & Fractals*, vol. 139, p. 110077, 2020.
- [17] T. Beer and I. Enting, "Fire spread and percolation modelling," *Mathematical and Computer Modelling*, vol. 13, no. 11, pp. 77–96, 1990.
- [18] S. R. Broadbent and J. M. Hammersley, "Percolation processes: I. crystals and mazes," in *Mathematical proceedings of the Cambridge philosophical society*, vol. 53, pp. 629–641, Cambridge University Press, 1957.
- [19] G. H. Weiss, *Contemporary problems in statistical physics*. SIAM, 1994.
- [20] S. Havlin and A. Bunde, "Percolation ii," in *Fractals and disordered systems*, pp. 97–150, Springer, 1991.
- [21] I. Essam, D. Gaunt, and A. Guttmann, "Percolation theory at the critical dimension," *Journal of Physics A: Mathematical and General*, vol. 11, no. 10, p. 1983, 1978.
- [22] M. Sykes and M. Wilkinson, "Derivation of series expansions for a study of percolation processes," *Journal of Physics A: Mathematical and General*, vol. 19, no. 16, p. 3415, 1986.
- [23] R. M. Ziff, "Spanning probability in 2d percolation," *Physical review letters*, vol. 69, no. 18, p. 2670, 1992.
- [24] L. Kadanoff, "Critical behavior, universality and scaling, proceedings of the 1970 varenna summer school on critical phenomena, edited by ms green," 1971.
- [25] V. Privman, P. Hohenberg, and A. Aharony, "Universal critical-point amplitude relations (phase transitions and critical phenomena vol 14, ed c dombo and jl lebowitz (new york: Academic), chapter 1," *and*, vol. 3647, p. 1134, 1991.

- [26] A. A. Saberi, “Recent advances in percolation theory and its applications,” *Physics Reports*, vol. 578, pp. 1–32, 2015.
- [27] A. V. Goltsev, S. N. Dorogovtsev, and J. F. F. Mendes, “k-core (bootstrap) percolation on complex networks: Critical phenomena and nonlocal effects,” *Physical Review E*, vol. 73, no. 5, p. 056101, 2006.
- [28] G. J. Baxter, S. N. Dorogovtsev, A. V. Goltsev, and J. F. Mendes, “Heterogeneous k-core versus bootstrap percolation on complex networks,” *Physical Review E*, vol. 83, no. 5, p. 051134, 2011.
- [29] S. B. Seidman, “Network structure and minimum degree,” *Social networks*, vol. 5, no. 3, pp. 269–287, 1983.
- [30] G. D. Bader and C. W. Hogue, “An automated method for finding molecular complexes in large protein interaction networks,” *BMC bioinformatics*, vol. 4, no. 1, pp. 1–27, 2003.
- [31] M. Newman and G. Ghoshal, “Bicomponents and the robustness of networks to failure,” *Physical Review Letters*, vol. 100, no. 13, p. 138701, 2008.
- [32] P. Kim, D.-S. Lee, and B. Kahng, “Phase transition in the biconnectivity of scale-free networks,” *Physical Review E*, vol. 87, no. 2, p. 022804, 2013.
- [33] S. Trajanovski, S. Scellato, and I. Leontiadis, “Error and attack vulnerability of temporal networks,” *Physical Review E*, vol. 85, no. 6, p. 066105, 2012.
- [34] M. J. Williams and M. Musolesi, “Spatio-temporal networks: reachability, centrality and robustness,” *Royal Society open science*, vol. 3, no. 6, p. 160196, 2016.
- [35] D. S. Callaway, J. E. Hopcroft, J. M. Kleinberg, M. E. Newman, and S. H. Strogatz, “Are randomly grown graphs really random?,” *Physical Review E*, vol. 64, no. 4, p. 041902, 2001.
- [36] D. Achlioptas, R. M. D’Souza, and J. Spencer, “Explosive percolation in random networks,” *science*, vol. 323, no. 5920, pp. 1453–1455, 2009.
- [37] P. Meakin, “Formation of fractal clusters and networks by irreversible diffusion-limited aggregation,” *Physical Review Letters*, vol. 51, no. 13, p. 1119, 1983.
- [38] M. Kolb, R. Botet, and R. Jullien, “Scaling of kinetically growing clusters,” *Physical Review Letters*, vol. 51, no. 13, p. 1123, 1983.
- [39] A. Turing, “The chemical basis of morphogenesis. phil. trans. roy. soc,” 1952.
- [40] V. Castets, E. Dulos, J. Boissonade, and P. De Kepper, “Experimental evidence of a sustained standing turing-type nonequilibrium chemical pattern,” *Physical Review Letters*, vol. 64, no. 24, p. 2953, 1990.

- [41] G. Turk, “Generating textures on arbitrary surfaces using reaction-diffusion,” *Acm Siggraph Computer Graphics*, vol. 25, no. 4, pp. 289–298, 1991.
- [42] A. Witkin and M. Kass, “Reaction-diffusion textures,” in *Proceedings of the 18th annual conference on computer graphics and interactive techniques*, pp. 299–308, 1991.
- [43] J. Shen and Y. M. Jung, “Geometric and stochastic analysis of reaction-diffusion patterns,” *Int J Pure Appl Math*, vol. 19, pp. 195–244, 2005.
- [44] Q. Ouyang and H. L. Swinney, “Transition to chemical turbulence,” *Chaos: An Interdisciplinary Journal of Nonlinear Science*, vol. 1, no. 4, pp. 411–420, 1991.
- [45] K. R. Mecke and D. Stoyan, “Morphological characterization of point patterns,” *Biometrical Journal: Journal of Mathematical Methods in Biosciences*, vol. 47, no. 4, pp. 473–488, 2005.
- [46] K. R. Mecke and D. Stoyan, *Morphology of condensed matter: physics and geometry of spatially complex systems*, vol. 600. Springer, 2008.
- [47] A. Krizhevsky, I. Sutskever, and G. E. Hinton, “Imagenet classification with deep convolutional neural networks,” *Advances in neural information processing systems*, vol. 25, pp. 1097–1105, 2012.
- [48] W. Xiong, L. Wu, F. Alleva, J. Droppo, X. Huang, and A. Stolcke, “The microsoft 2017 conversational speech recognition system,” in *2018 IEEE international conference on acoustics, speech and signal processing (ICASSP)*, pp. 5934–5938, IEEE, 2018.
- [49] J. Howard and S. Ruder, “Universal language model fine-tuning for text classification,” *arXiv preprint arXiv:1801.06146*, 2018.
- [50] P. Rajpurkar, J. Irvin, K. Zhu, B. Yang, H. Mehta, T. Duan, D. Ding, A. Bagul, C. Langlotz, K. Shpanskaya, *et al.*, “Chexnet: Radiologist-level pneumonia detection on chest x-rays with deep learning,” *arXiv preprint arXiv:1711.05225*, 2017.
- [51] G. Cammarota, G. Ianiro, A. Ahern, C. Carbone, A. Temko, M. J. Claesson, A. Gasbarrini, and G. Tortora, “Gut microbiome, big data and machine learning to promote precision medicine for cancer,” *Nature reviews gastroenterology & hepatology*, vol. 17, no. 10, pp. 635–648, 2020.
- [52] N. Banaei, J. Moshfegh, A. Mohseni-Kabir, J. M. Houghton, Y. Sun, and B. Kim, “Machine learning algorithms enhance the specificity of cancer biomarker detection using sers-based immunoassays in microfluidic chips,” *RSC advances*, vol. 9, no. 4, pp. 1859–1868, 2019.
- [53] L. Adlung, Y. Cohen, U. Mor, and E. Elinav, “Machine learning in clinical decision making,” *Med*, 2021.

- [54] S. N. Khatami and C. Gopalappa, “A reinforcement learning model to inform optimal decision paths for hiv elimination1,” *medRxiv*, pp. 2021–07, 2021.
- [55] A. Li, R. Chen, A. B. Farimani, and Y. J. Zhang, “Reaction diffusion system prediction based on convolutional neural network,” *Scientific reports*, vol. 10, no. 1, pp. 1–9, 2020.
- [56] A.-L. Barabási, “The network takeover,” *Nature Physics*, vol. 8, no. 1, p. 14, 2011.
- [57] S. H. Strogatz, “Exploring complex networks,” *nature*, vol. 410, no. 6825, p. 268, 2001.
- [58] M. E. Newman, “The structure and function of complex networks,” *SIAM review*, vol. 45, no. 2, pp. 167–256, 2003.
- [59] S. N. Dorogovtsev, A. V. Goltsev, and J. F. Mendes, “Critical phenomena in complex networks,” *Reviews of Modern Physics*, vol. 80, no. 4, p. 1275, 2008.
- [60] R. Albert and A.-L. Barabási, “Statistical mechanics of complex networks,” *Reviews of modern physics*, vol. 74, no. 1, p. 47, 2002.
- [61] D. S. Callaway, M. E. Newman, S. H. Strogatz, and D. J. Watts, “Network robustness and fragility: Percolation on random graphs,” *Physical review letters*, vol. 85, no. 25, p. 5468, 2000.
- [62] R. Cohen, K. Erez, D. Ben-Avraham, and S. Havlin, “Resilience of the internet to random breakdowns,” *Physical review letters*, vol. 85, no. 21, p. 4626, 2000.
- [63] A. Vespignani, “Modelling dynamical processes in complex socio-technical systems,” *Nature physics*, vol. 8, no. 1, p. 32, 2012.
- [64] M. Kitsak, L. K. Gallos, S. Havlin, F. Liljeros, L. Muchnik, H. E. Stanley, and H. A. Makse, “Identification of influential spreaders in complex networks,” *Nature physics*, vol. 6, no. 11, p. 888, 2010.
- [65] R. Pastor-Satorras and A. Vespignani, “Epidemic spreading in scale-free networks,” *Physical review letters*, vol. 86, no. 14, p. 3200, 2001.
- [66] G. Grimmett, “What is percolation?,” in *Percolation*, pp. 1–31, Springer, 1999.
- [67] S. Shao, X. Huang, H. E. Stanley, and S. Havlin, “Percolation of localized attack on complex networks,” *New Journal of Physics*, vol. 17, no. 2, p. 023049, 2015.
- [68] Y. Berezin, A. Bashan, M. M. Danziger, D. Li, and S. Havlin, “Localized attacks on spatially embedded networks with dependencies,” *Scientific reports*, vol. 5, p. 8934, 2015.

- [69] G. Dong, J. Gao, L. Tian, R. Du, and Y. He, “Percolation of partially interdependent networks under targeted attack,” *Physical Review E*, vol. 85, no. 1, p. 016112, 2012.
- [70] X. Huang, J. Gao, S. V. Buldyrev, S. Havlin, and H. E. Stanley, “Robustness of interdependent networks under targeted attack,” *Physical Review E*, vol. 83, no. 6, p. 065101, 2011.
- [71] D. Stauffer and A. Aharony, *Introduction to percolation theory*. Taylor & Francis, 2018.
- [72] J. Wang, Z. Zhou, W. Zhang, T. M. Garoni, and Y. Deng, “Bond and site percolation in three dimensions,” *Physical Review E*, vol. 87, no. 5, p. 052107, 2013.
- [73] S. Mertens and C. Moore, “Percolation thresholds in hyperbolic lattices,” *Physical Review E*, vol. 96, no. 4, p. 042116, 2017.
- [74] J. L. Jacobsen, “Critical points of potts and o (n) models from eigenvalue identities in periodic temperley–lieb algebras,” *Journal of Physics A: Mathematical and Theoretical*, vol. 48, no. 45, p. 454003, 2015.
- [75] C. R. Scullard and J. L. Jacobsen, “Bond percolation thresholds on archimedean lattices from critical polynomial roots,” *Physical Review Research*, vol. 2, no. 1, p. 012050, 2020.
- [76] S. N. Dorogovtsev, A. V. Goltsev, and J. F. F. Mendes, “K-core organization of complex networks,” *Physical Review Letters*, vol. 96, no. 4, p. 040601, 2006.
- [77] X. Yuan, Y. Dai, H. E. Stanley, and S. Havlin, “k-core percolation on complex networks: Comparing random, localized, and targeted attacks,” *Physical Review E*, vol. 93, no. 6, p. 062302, 2016.
- [78] D. Lee, M. Jo, and B. Kahng, “Critical behavior of k-core percolation: Numerical studies,” *Physical Review E*, vol. 94, no. 6, p. 062307, 2016.
- [79] M. Li, Y. Deng, and B.-H. Wang, “Clique percolation in random graphs,” *Physical Review E*, vol. 92, no. 4, p. 042116, 2015.
- [80] I. Derényi, G. Palla, and T. Vicsek, “Clique percolation in random networks,” *Physical review letters*, vol. 94, no. 16, p. 160202, 2005.
- [81] A. Furlan, D. C. dos Santos, R. M. Ziff, and R. Dickman, “Jamming and percolation of dimers in restricted-valence random sequential adsorption,” *Physical Review Research*, vol. 2, no. 4, p. 043027, 2020.
- [82] S. Carmi, S. Havlin, S. Kirkpatrick, Y. Shavitt, and E. Shir, “A model of internet topology using k-shell decomposition,” *Proceedings of the National Academy of Sciences*, vol. 104, no. 27, pp. 11150–11154, 2007.

- [83] J. I. Alvarez-Hamelin, L. Dall'Asta, A. Barrat, and A. Vespignani, "How the k-core decomposition helps in understanding the internet topology," in *ISMA Workshop on the Internet Topology*, vol. 1, 2006.
- [84] J. E. Hopcroft and R. E. Tarjan, "Dividing a graph into triconnected components," *SIAM Journal on Computing*, vol. 2, no. 3, pp. 135–158, 1973.
- [85] J. Cheriyan and R. Thurimella, "Algorithms for parallel k-vertex connectivity and sparse certificates," in *Proceedings of the twenty-third annual ACM Symposium on Theory of Computing*, pp. 391–401, ACM, 1991.
- [86] G. Grimmett, "Percolation and disordered systems," in *Lectures on Probability Theory and Statistics*, pp. 153–300, Springer, 1997.
- [87] M. Newman and R. Ziff, "Efficient monte carlo algorithm and high-precision results for percolation," *Physical Review Letters*, vol. 85, no. 19, p. 4104, 2000.
- [88] C. Gutwenger and P. Mutzel, "A linear time implementation of spqr-trees," in *International Symposium on Graph Drawing*, pp. 77–90, Springer, 2000.
- [89] J. I. Alvarez-Hamelin, L. Dall'Asta, A. Barrat, and A. Vespignani, "k-core decomposition: a tool for the analysis of large scale internet graphs," *arXiv preprint cs.NI/0511007*, 2005.
- [90] S. Wuchty and E. Almaas, "Evolutionary cores of domain co-occurrence networks," *BMC evolutionary biology*, vol. 5, no. 1, p. 24, 2005.
- [91] P. Kogut and P. Leath, "Bootstrap percolation transitions on real lattices," *Journal of Physics C: Solid State Physics*, vol. 14, no. 22, p. 3187, 1981.
- [92] J. Gravner, A. E. Holroyd, and R. Morris, "A sharper threshold for bootstrap percolation in two dimensions," *Probability Theory and Related Fields*, vol. 153, no. 1-2, pp. 1–23, 2012.
- [93] D. P. Landau and K. Binder, *A guide to Monte Carlo simulations in statistical physics*. Cambridge University Press, 2014.
- [94] F. Radicchi and S. Fortunato, "Explosive percolation: A numerical analysis," *Physical Review E*, vol. 81, no. 3, p. 036110, 2010.
- [95] D. Stauffer and A. Aharony, *Introduction to percolation theory*. Taylor & Francis, 2014.
- [96] S.-K. Ma, *Modern theory of critical phenomena*. Routledge, 2018.
- [97] N. Azimi-Tafreshi, J. Gómez-Gardenes, and S. Dorogovtsev, "k- core percolation on multiplex networks," *Physical Review E*, vol. 90, no. 3, p. 032816, 2014.

- [98] G. Shlifer, W. Klein, P. Reynolds, and H. Stanley, “Large-cell renormalisation group for the backbone problem in percolation,” *Journal of Physics A: Mathematical and General*, vol. 12, no. 7, p. L169, 1979.
- [99] M. Sahimi, “Scaling relation for the critical exponents of the backbone of percolation clusters,” *Journal of Physics A: Mathematical and General*, vol. 17, no. 15, p. 3073, 1984.
- [100] D. Kreutz, F. M. Ramos, P. E. Verissimo, C. E. Rothenberg, S. Azodolmolky, and S. Uhlig, “Software-defined networking: A comprehensive survey,” *Proceedings of the IEEE*, vol. 103, no. 1, pp. 14–76, 2014.
- [101] É. Fodor and M. C. Marchetti, “The statistical physics of active matter: From self-catalytic colloids to living cells,” *Physica A: Statistical Mechanics and its Applications*, vol. 504, pp. 106–120, 2018.
- [102] Q.-X. Liu, M. Rietkerk, P. M. Herman, T. Piersma, J. M. Fryxell, and J. van de Koppel, “Phase separation driven by density-dependent movement: a novel mechanism for ecological patterns,” *Physics of life reviews*, vol. 19, pp. 107–121, 2016.
- [103] J. Krug and P. A. Ferrari, “Phase transitions in driven diffusive systems with random rates,” *Journal of Physics A: Mathematical and General*, vol. 29, no. 18, p. L465, 1996.
- [104] M. Moussaïd, D. Helbing, S. Garnier, A. Johansson, M. Combe, and G. Theraulaz, “Experimental study of the behavioural mechanisms underlying self-organization in human crowds,” *Proceedings of the Royal Society B: Biological Sciences*, vol. 276, no. 1668, pp. 2755–2762, 2009.
- [105] R. Doursat, H. Sayama, and O. Michel, *Morphogenetic engineering: toward programmable complex systems*. Springer, 2012.
- [106] E. V. Timofeeva, A. N. Gavrilov, J. M. McCloskey, Y. V. Tolmachev, S. Sprunt, L. M. Lopatina, and J. V. Selinger, “Thermal conductivity and particle agglomeration in alumina nanofluids: experiment and theory,” *Physical Review E*, vol. 76, no. 6, p. 061203, 2007.
- [107] S. Khatami and Z. Aksamija, “Lattice thermal conductivity of the binary and ternary group-iv alloys si-sn, ge-sn, and si-ge-sn,” *Physical Review Applied*, vol. 6, no. 1, p. 014015, 2016.
- [108] J. Werfel, K. Petersen, and R. Nagpal, “Designing collective behavior in a termite-inspired robot construction team,” *Science*, vol. 343, no. 6172, pp. 754–758, 2014.
- [109] B. Yigit, Y. Alapan, and M. Sitti, “Programmable collective behavior in dynamically self-assembled mobile microrobotic swarms,” *Advanced Science*, vol. 6, no. 6, p. 1801837, 2019.

- [110] J. Palacci, S. Sacanna, A. P. Steinberg, D. J. Pine, and P. M. Chaikin, “Living crystals of light-activated colloidal surfers,” *Science*, vol. 339, no. 6122, pp. 936–940, 2013.
- [111] M. Rubenstein, A. Cornejo, and R. Nagpal, “Programmable self-assembly in a thousand-robot swarm,” *Science*, vol. 345, no. 6198, pp. 795–799, 2014.
- [112] M. Droz, Z. Rácz, and J. Schmidt, “One-dimensional kinetic ising model with competing dynamics: Steady-state correlations and relaxation times,” *Physical Review A*, vol. 39, no. 4, p. 2141, 1989.
- [113] A.-L. Barabási and H. E. Stanley, *Fractal concepts in surface growth*. Cambridge university press, 1995.
- [114] G. B. Marin, G. S. Yablonsky, and D. Constales, *Kinetics of chemical reactions: Decoding complexity*. Wiley-VCH, 2019.
- [115] H.-K. Janssen, “On the nonequilibrium phase transition in reaction-diffusion systems with an absorbing stationary state,” *Zeitschrift für Physik B Condensed Matter*, vol. 42, no. 2, pp. 151–154, 1981.
- [116] P. Grassberger, “On phase transitions in schlögl’s second model,” in *Nonlinear Phenomena in Chemical Dynamics*, pp. 262–262, Springer, 1981.
- [117] P. Bak, C. Tang, and K. Wiesenfeld, “Self-organized criticality,” *Physical review A*, vol. 38, no. 1, p. 364, 1988.
- [118] M. Rossi, R. Pastor-Satorras, and A. Vespignani, “Universality class of absorbing phase transitions with a conserved field,” *Physical review letters*, vol. 85, no. 9, p. 1803, 2000.
- [119] S. Lübeck and P. Heger, “Universal scaling behavior at the upper critical dimension of nonequilibrium continuous phase transitions,” *Physical review letters*, vol. 90, no. 23, p. 230601, 2003.
- [120] S. Manna, “Two-state model of self-organized criticality,” *Journal of Physics A: Mathematical and General*, vol. 24, no. 7, p. L363, 1991.
- [121] M. Starnini and R. Pastor-Satorras, “Temporal percolation in activity-driven networks,” *Physical Review E*, vol. 89, no. 3, p. 032807, 2014.
- [122] M. Suzuki, “New universality of critical exponents,” *Progress of Theoretical Physics*, vol. 51, no. 6, pp. 1992–1993, 1974.
- [123] L. Wang, B. Liu, D. Goeckel, D. Towsley, and C. Westphal, “Connectivity in cooperative wireless ad hoc networks,” in *Proceedings of the 9th ACM international symposium on Mobile ad hoc networking and computing*, pp. 121–130, 2008.

- [124] L. Rashidi, D. Towsley, A. Mohseni-Kabir, and A. Movaghar, “On the performance analysis of epidemic routing in non-sparse delay tolerant networks,” *arXiv preprint arXiv:2002.04834*, 2020.
- [125] W. Ettoumi, J. Kasparian, and J.-P. Wolf, “Spin-glass model governs laser multiple filamentation,” *Physical review letters*, vol. 115, no. 3, p. 033902, 2015.
- [126] A. M. Turing, “The chemical basis of morphogenesis,” *Bulletin of mathematical biology*, vol. 52, no. 1-2, pp. 153–197, 1990.
- [127] J. W. Cahn and J. E. Hilliard, “Free energy of a nonuniform system. i. interfacial free energy,” *The Journal of chemical physics*, vol. 28, no. 2, pp. 258–267, 1958.
- [128] X. Fu, L.-H. Tang, C. Liu, J.-D. Huang, T. Hwa, and P. Lenz, “Stripe formation in bacterial systems with density-suppressed motility,” *Physical review letters*, vol. 108, no. 19, p. 198102, 2012.
- [129] Q.-X. Liu, A. Doelman, V. Rottschäfer, M. de Jager, P. M. Herman, M. Rietkerk, and J. van de Koppel, “Phase separation explains a new class of self-organized spatial patterns in ecological systems,” *Proceedings of the National Academy of Sciences*, vol. 110, no. 29, pp. 11905–11910, 2013.
- [130] D. E. Wolf, M. Schreckenberg, and A. Bachem, *Traffic and granular flow*. World Scientific, 1996.
- [131] D. Mollison, “Spatial contact models for ecological and epidemic spread,” *Journal of the Royal Statistical Society: Series B (Methodological)*, vol. 39, no. 3, pp. 283–313, 1977.
- [132] S. Clar, B. Drossel, and F. Schwabl, “Forest fires and other examples of self-organized criticality,” *Journal of Physics: Condensed Matter*, vol. 8, no. 37, p. 6803, 1996.
- [133] W. Kinzel, “Phase transitions of cellular automata,” *Zeitschrift für Physik B Condensed Matter*, vol. 58, no. 3, pp. 229–244, 1985.
- [134] M. Henkel, H. Hinrichsen, S. Lübeck, and M. Pleimling, *Non-equilibrium phase transitions*, vol. 1. Springer, 2008.
- [135] Y. Kantor and M. Kardar, “Percolation of sites not removed by a random walker in d dimensions,” *Physical Review E*, vol. 100, no. 2, p. 022125, 2019.
- [136] L. D. Valdez, P. A. Macri, and L. A. Braunstein, “Temporal percolation of a susceptible adaptive network,” *Physica A: Statistical Mechanics and its Applications*, vol. 392, no. 18, pp. 4172–4180, 2013.
- [137] N. Khan, P. Sarkar, A. Midya, P. Mandal, and P. Mohanty, “Continuously varying critical exponents beyond weak universality,” *Scientific reports*, vol. 7, no. 1, pp. 1–7, 2017.

- [138] B. Sutherland, “Two-dimensional hydrogen bonded crystals without the ice rule,” *Journal of Mathematical Physics*, vol. 11, no. 11, pp. 3183–3186, 1970.
- [139] L. P. Kadanoff and F. J. Wegner, “Some critical properties of the eight-vertex model,” *Physical Review B*, vol. 4, no. 11, p. 3989, 1971.
- [140] C. Fan and F. Y. Wu, “General lattice model of phase transitions,” *Physical Review B*, vol. 2, no. 3, p. 723, 1970.
- [141] S. de Queiroz, “Scaling behavior of a square-lattice ising model with competing interactions in a uniform field,” *Physical Review E*, vol. 84, no. 3, p. 031132, 2011.
- [142] T. Suzuki, K. Harada, H. Matsuo, S. Todo, and N. Kawashima, “Thermal phase transition of generalized heisenberg models for $su(n)$ spins on square and honeycomb lattices,” *Physical Review B*, vol. 91, no. 9, p. 094414, 2015.
- [143] F. Alet, J. L. Jacobsen, G. Misguich, V. Pasquier, F. Mila, and M. Troyer, “Interacting classical dimers on the square lattice,” *Physical review letters*, vol. 94, no. 23, p. 235702, 2005.
- [144] Y. Deng, T. M. Garoni, J. Machta, G. Ossola, M. Polin, and A. D. Sokal, “Critical behavior of the chayes–machta–swendsen–wang dynamics,” *Physical review letters*, vol. 99, no. 5, p. 055701, 2007.
- [145] T. Newman, “Continuously varying exponents in reaction-diffusion systems,” *Journal of Physics A: Mathematical and General*, vol. 28, no. 6, p. L183, 1995.
- [146] H. Janssen, K. Oerding, F. Van Wijland, and H. Hilhorst, “Lévy-flight spreading of epidemic processes leading to percolating clusters,” *The European Physical Journal B-Condensed Matter and Complex Systems*, vol. 7, no. 1, pp. 137–145, 1999.
- [147] J. D. Noh and H. Park, “Universality class of absorbing transitions with continuously varying critical exponents,” *Physical Review E*, vol. 69, no. 1, p. 016122, 2004.
- [148] Y. Cho, J. Lee, H. Herrmann, and B. Kahng, “Hybrid percolation transition in cluster merging processes: Continuously varying exponents,” *Physical review letters*, vol. 116, no. 2, p. 025701, 2016.
- [149] S. Kondo and T. Miura, “Reaction-diffusion model as a framework for understanding biological pattern formation,” *science*, vol. 329, no. 5999, pp. 1616–1620, 2010.
- [150] H. Meinhardt, “Models of biological pattern formation: from elementary steps to the organization of embryonic axes,” *Current topics in developmental biology*, vol. 81, pp. 1–63, 2008.

- [151] A. J. Bray, “Theory of phase-ordering kinetics,” *Advances in Physics*, vol. 51, no. 2, pp. 481–587, 2002.
- [152] F. Falk, “Cahn-hilliard theory and irreversible thermodynamics,” *Journal of Non-Equilibrium Thermodynamics*, vol. 17, no. 1, pp. 53–66, 1992.
- [153] E. Kuhl and D. W. Schmid, “Computational modeling of mineral unmixing and growth,” *Computational Mechanics*, vol. 39, no. 4, pp. 439–451, 2007.
- [154] F. Spineanu and M. Vlad, “The filamentation of the laser beam as a labyrinth instability,” in *Journal of Physics: Conference Series*, vol. 633, p. 012032, IOP Publishing, 2015.
- [155] K. G. Soga, J. R. Melrose, and R. C. Ball, “Continuum percolation and depletion flocculation,” *The Journal of chemical physics*, vol. 108, no. 14, pp. 6026–6032, 1998.
- [156] C. Moore and M. E. Newman, “Exact solution of site and bond percolation on small-world networks,” *Physical Review E*, vol. 62, no. 5, p. 7059, 2000.
- [157] R. M. Ziff, “Scaling behavior of explosive percolation on the square lattice,” *Physical Review E*, vol. 82, no. 5, p. 051105, 2010.
- [158] F. Ginelli, V. Ahlers, R. Livi, D. Mukamel, A. Pikovsky, A. Politi, and A. Torcini, “From multiplicative noise to directed percolation in wetting transitions,” *Physical Review E*, vol. 68, no. 6, p. 065102, 2003.
- [159] S. Fortunato and H. Satz, “Percolation and magnetization for generalized continuous spin models,” *Nuclear Physics B*, vol. 598, no. 3, pp. 601–611, 2001.
- [160] R. J. Baxter, “Eight-vertex model in lattice statistics,” *Physical Review Letters*, vol. 26, no. 14, p. 832, 1971.
- [161] A. Zisook, “Second-order expansion of indices in the generalised villain model,” *Journal of Physics A: Mathematical and General*, vol. 13, no. 7, p. 2451, 1980.
- [162] S. Mertens and C. Moore, “Continuum percolation thresholds in two dimensions,” *Physical Review E*, vol. 86, no. 6, p. 061109, 2012.
- [163] R. A. Neville, *Topological techniques for characterization of patterns in differential equations*. PhD thesis, Colorado State University. Libraries, 2017.
- [164] J. Carrasquilla and R. G. Melko, “Machine learning phases of matter,” *Nature Physics*, vol. 13, no. 5, p. 431, 2017.
- [165] L. Wang, “Discovering phase transitions with unsupervised learning,” *Physical Review B*, vol. 94, no. 19, p. 195105, 2016.

- [166] K. T. Butler, D. W. Davies, H. Cartwright, O. Isayev, and A. Walsh, “Machine learning for molecular and materials science,” *Nature*, vol. 559, no. 7715, pp. 547–555, 2018.
- [167] G. Torlai, G. Mazzola, J. Carrasquilla, M. Troyer, R. Melko, and G. Carleo, “Neural-network quantum state tomography,” *Nature Physics*, vol. 14, no. 5, p. 447, 2018.
- [168] I. Glasser, N. Pancotti, M. August, I. D. Rodriguez, and J. I. Cirac, “Neural-network quantum states, string-bond states, and chiral topological states,” *Physical Review X*, vol. 8, no. 1, p. 011006, 2018.
- [169] P. Zhang, H. Shen, and H. Zhai, “Machine learning topological invariants with neural networks,” *Physical review letters*, vol. 120, no. 6, p. 066401, 2018.
- [170] P. Huembeli, A. Dauphin, P. Wittek, and C. Gogolin, “Automated discovery of characteristic features of phase transitions in many-body localization,” *Physical Review B*, vol. 99, no. 10, p. 104106, 2019.
- [171] J. Venderley, V. Khemani, and E.-A. Kim, “Machine learning out-of-equilibrium phases of matter,” *Physical review letters*, vol. 120, no. 25, p. 257204, 2018.
- [172] K. Ch’ng, N. Vazquez, and E. Khatami, “Unsupervised machine learning account of magnetic transitions in the hubbard model,” *Physical Review E*, vol. 97, no. 1, p. 013306, 2018.
- [173] J. F. Rodriguez-Nieva and M. S. Scheurer, “Identifying topological order through unsupervised machine learning,” *Nature Physics*, p. 1, 2019.
- [174] S. Dernbach, A. Mohseni-Kabir, S. Pal, M. Gepner, and D. Towsley, “Quantum walk neural networks with feature dependent coins,” *Applied Network Science*, vol. 4, no. 1, pp. 1–16, 2019.
- [175] S. Dernbach, A. Mohseni-Kabir, S. Pal, and D. Towsley, “Quantum walk neural networks for graph-structured data,” in *International Conference on Complex Networks and their Applications*, pp. 182–193, Springer, 2018.
- [176] S. H. Strogatz, *Nonlinear dynamics and chaos: with applications to physics, biology, chemistry, and engineering*. CRC Press, 2018.
- [177] I. Goodfellow, Y. Bengio, and A. Courville, *Deep learning*. MIT press, 2016.
- [178] H. Hotelling, “Analysis of a complex of statistical variables into principal components.,” *Journal of educational psychology*, vol. 24, no. 6, p. 417, 1933.
- [179] G. E. Hinton and R. S. Zemel, “Autoencoders, minimum description length and helmholtz free energy,” in *Advances in neural information processing systems*, pp. 3–10, 1994.

- [180] D. P. Kingma and M. Welling, “Auto-encoding variational bayes,” *arXiv preprint arXiv:1312.6114*, 2013.
- [181] J. A. Hartigan and M. A. Wong, “Algorithm as 136: A k-means clustering algorithm,” *Journal of the Royal Statistical Society. Series C (Applied Statistics)*, vol. 28, no. 1, pp. 100–108, 1979.
- [182] S. Dasgupta, “Learning mixtures of gaussians,” in *40th Annual Symposium on Foundations of Computer Science (Cat. No. 99CB37039)*, pp. 634–644, IEEE, 1999.
- [183] W. M. Rand, “Objective criteria for the evaluation of clustering methods,” *Journal of the American Statistical association*, vol. 66, no. 336, pp. 846–850, 1971.
- [184] L. Hubert and P. Arabie, “Comparing partitions,” *Journal of classification*, vol. 2, no. 1, pp. 193–218, 1985.
- [185] M. J. Warrens, “On the equivalence of cohen’s kappa and the hubert-arabie adjusted rand index,” *Journal of classification*, vol. 25, no. 2, pp. 177–183, 2008.
- [186] J. von Hardenberg, E. Meron, M. Shachak, and Y. Zarmi, “Diversity of vegetation patterns and desertification,” *Physical Review Letters*, vol. 87, no. 19, p. 198101, 2001.
- [187] J. W. Cahn and J. E. Hilliard, “Spinodal decomposition: A reprise,” *Acta Metallurgica*, vol. 19, no. 2, pp. 151–161, 1971.